

Electronic Thesis and Dissertation Repository

12-11-2015 12:00 AM

Photonic Crystal Directional Coupler Based Optomechanical Sensor

Michael A. Zylstra
The University of Western Ontario

Supervisor
Professor Jayshri Sabarinathan
The University of Western Ontario

Graduate Program in Electrical and Computer Engineering
A thesis submitted in partial fulfillment of the requirements for the degree in Master of Engineering Science
© Michael A. Zylstra 2015

Follow this and additional works at: <https://ir.lib.uwo.ca/etd>

Recommended Citation

Zylstra, Michael A., "Photonic Crystal Directional Coupler Based Optomechanical Sensor" (2015).
Electronic Thesis and Dissertation Repository. 3447.
<https://ir.lib.uwo.ca/etd/3447>

This Dissertation/Thesis is brought to you for free and open access by Scholarship@Western. It has been accepted for inclusion in Electronic Thesis and Dissertation Repository by an authorized administrator of Scholarship@Western. For more information, please contact wlsadmin@uwo.ca.

PHOTONIC CRYSTAL DIRECTIONAL COUPLER BASED
OPTOMECHANICAL SENSOR

by

Michael Zylstra

Graduate Program in Electrical and Computer Engineering

A thesis submitted in partial fulfillment
of the requirements for the degree of
Masters of Engineering Science

The School of Graduate and Postdoctoral Studies
The University of Western Ontario
London, Ontario, Canada

© Michael Abraham Zylstra 2016

Abstract

An extremely small ($6.5 \times 6.5 \mu\text{m}$) optomechanical sensor is proposed that utilizes a photonic crystal (PC) etched onto silicon-on-insulator (SOI) using adapted complimentary metal-oxide-semiconductor fabrication technology. The destructive interference of light with the periodic structure can forbid its propagation inside the crystal across a range of frequencies and can be used to confine light near edge of a PC slab. By placing two PC edges near each other, a directional coupler is formed where light is periodically exchanged between the two waveguides. Wet-etching away the buried oxide residing beneath the photonic crystal directional coupler (PCDC), a membrane is formed. Exerting force on the PCDC alters the separation between the two PC edges and modulates the observed transmission at the coupler outputs. Buckle-mitigating structures are also demonstrated here which relieve the unpredictable compressive stress built into the top silicon layer of SOI during wafer fabrication.

The PCDC sensors attempt to overcome some of the shortcomings of existing micromechanical sensors such as area constraints, material restrictions, stiction, and EM interference. PCDC sensors are also highly parallelizable due to their small size and wide optical bandwidth. PCDC sensors are envisaged to be used in microfluidic integration and are capable of 149kPa full scale pressure measurement ranges.

Keywords: Photonics, Photonic Crystal, Optomechanical, Sensor, Directional Coupler

Acknowledgements

Firstly, I would like to thank the University of Western Ontario for their beautiful campus, stimulating learning environment, and vibrant student life. I am thankful for the competitive grants I have received over the years that had made my education affordable particularly OGS, QEII-GSST, as well as NSERC USRA. Knowledge is power. I am thankful for the wisdom of elected leaders for their continued investment in education at both the federal and provincial levels; this not only prepares the next generation of Canadian scientists and engineers, but brings a sense of relevance to our research.

A very special thanks to CMC Microsystems. Bob Mallard and Susan Xu for their support with setting up the silicon photonic testbench; our experiment results could not be possible without their help. A nod to John Bock and Jessical Zhang for their administration work with the SiEPIC Passive Photonics 2014 Workshop at Universite Laval, Quebec City. The multiproject wafers are affordable means for students to gain valuable experience working with world class foundries like the IMEC ePIX-fab.

I would like to thank the UWO nanofab for the use of their SEM and nanopatterning tools as well Todd Simpson and Tim Goldhawk with their general expertise and patience. Also, Dr. Edward Xu and the Toronto nanofabrication center for their enthusiasm and the silicon etching of our buckle-mitigated structures. A special thanks to Dr. Evgueni Bordatchev for his help in performing the optical profilometry measurements on the buckle-mitigated structures which validates an important design strategy for these sensors.

Photonics is not an easy subject learn, let alone teach to someone. I would like to reserve a most special thanks professor Jayshri Sabarinathan and Dr. Aref Bakhtazad and their ultimate patience and guidance throughout this project. Learning, designing, fabricating, setting up our test-bench, and finally testing our first photonic devices, basically from scratch, was extremely rewarding. Considering where we were two years ago I was not entirely sure this was possible. Our research group is small, but tight; this was truly a team effort and we all should be very proud of ourselves.

Finally, I would like to thank my family who always try to get the best out of me. I could not have done this without the life-skills and work ethic instilled by my parents. And my brothers, Chris, Trevor, and Steve, who are always asking what I'm working on, always curious. Science and engineering is more than numbers and equations, there is a human element that ultimately motivates us; a desire to investigate and communicate ideas with our friends. We must cherish and appreciate the relationships we are in, for they give meaning to all life's work.

Contents

Certificate of Examination	ii
Abstract	ii
Acknowledgements	iii
List of Figures	vii
List of Tables	xii
List of Appendices	xiii
List of Abbreviations, Symbols, and Nomenclature	xiv
1 Introduction	1
1.1 Micromechanical Markets and Trends	1
1.2 Performance Characteristics	3
1.2.1 Material Properties	3
1.2.2 Overall Transduction Performance	4
1.2.3 Piezoresistive Sensors	5
1.2.4 Capacitive Sensors	6
1.2.5 Micro-optoelectromechanical Systems (MOEMS)	7
1.3 A Case for Photonic Crystal Directional Coupler Sensors	8
1.4 Objectives and Thesis Layout	11
1.5 Overview of Thesis	12
1.6 Contributions	12
2 Background	14
2.1 Introduction	14
2.2 Dielectric Slabs	14
2.3 Photonic Crystals	17
2.4 Photonic Crystal Slab Line Defects	21
2.5 Optical Directional Coupler	23

2.6	Operating Principle of Coupler Based Optomechanical Sensor	24
2.7	Conclusion	27
3	Design and Simulation	28
3.1	Design Overview	29
3.2	Optical Design	29
3.2.1	Fabrication Constraints	29
3.2.2	SOI Substrate and Etch Depths	29
3.2.3	Surface Grating Coupler Ports	30
3.2.4	Bulk PC Design Using Plane Wave Expansion	30
3.2.5	PCDC Defect Design Using PWE	32
3.2.6	FDTD Simulation	35
3.3	Mechanical Design	39
3.3.1	Buckling in SOI	40
3.3.2	Non-buckled Designs $\sigma_{crt} > \sigma_0$	41
3.3.3	Buckled Designs $\sigma_{crt} < \sigma_0$	42
3.3.4	Buckle Mitigated Designs	45
3.4	Conclusion	46
4	Process Flow	47
4.1	Fabrication Overview	47
4.2	CMC-IMEC Silicon Photonics Foundry MPW	47
4.2.1	Layout	47
4.3	UWO Nanofab Fabrication Process	50
4.3.1	E-beam Lithography	50
4.3.2	Deep Reactive Ion Etching	51
4.3.3	HF Under-Etching	51
4.3.4	Critical Point Drying	52
4.3.5	SEM Characterization	52
4.4	Conclusion	52
5	Sensor Measurements and Evaluation	54
5.1	Introduction	54
5.2	Sensor Measurement Procedure	54
5.3	Optical Measurements	57
5.4	Evaluation of Buckle-Compensation Structures	58
5.5	Conclusion	59
6	Closing Remarks and Conclusion	64
6.1	Summary	64

6.2	Configurations and Applications	65
6.2.1	Packaging	65
6.2.2	Pressure Sensors	65
6.2.3	Detector Integration	65
6.2.4	Dynamic Range and Noise	66
6.3	Future Work	67
6.3.1	<i>In situ</i> Measurement of the PCDC Sensor	67
6.4	Conclusion	68
	Bibliography	69
	A Finite-Difference Time-Domain	78
	B Plane Wave Expansion	81
	C FDTD Script (Lumerical)	83
	D Buckling Analysis	89
	E Project Specifications	92
	Curriculum Vitae	94

List of Figures

1.1	Cross section of piezoresistive-based sensor. Doping enhances the piezoresistive effect and is generally done near regions of high-stress.	5
1.2	Capacitive-based MEMS sensors detect the changes in capacitance based on microplate spacing.	6
1.3	Cavity-based optomechanical sensor is shown bonded to fiber optic cable which can be based on either changes in reflected intensity or colour. Intensity changes may be observed as based on the position of the reflective membrane and fiber optic properties. Changes in colour may be observed as membrane deflections change the optical resonant properties of the cavity.	7
1.4	PC-based vertical cavity pressure sensor previously investigated by our research group. (a) Unloaded sensor cross section showing supported membrane and under-etched SOI. (b) Exerting pressure on the membrane brings the PC line defect closer to the bottom substrate. Light propagating along the PC defect leaks into the bottom substrate and decreases the transmitted intensity (c) scanning electron microscope image of the PC membrane and line defect.	9
1.5	Design concept: (a) PCDCs are known to significantly reduce coupling lengths. (b) By isolating the waveguides, (c) a membrane may be formed and modulate the observed transmission.	10
2.1	Light impinging on the edge of a dielectric slab is shown. Light which does not satisfy total internal reflection condition (a) is gradually diminished. Light which does satisfy TIR (b) is confined to lie inside the slab exhibiting distinct spatial and temporal symmetries	15
2.2	Dispersion diagram of a silicon slab $n_{Si} = 3.46$ normalized with respect to thickness t . For the first mode $n = 1$, the expected homogeneous propagation conditions is asymptotically reached quickly with increasing k . A singular mode can be made to exist in thin slabs where the free-space wavelength is of the same order as the thickness. In this case, the simple ray model breaks down and Maxwell's equations must be solved numerically.	16
2.3	Crystals are, by definition, repetitive structures. (a) 1D, (b) 2D, and (c) 3D photonic crystal is shown composed of two dielectric materials	17

2.4	Also known as Bragg's law, the reciprocal lattice yields the selection rules for possible scattering events inside a PC. The Fourier transform (FT) of the periodic dielectric arrangement yields the reciprocal lattice. Applying the Bloch theorem (BT) restricts analysis to a Voronoi-like region in \mathbf{k} -space. Here ΓMK represent points of high symmetry [77].	19
2.5	The dispersion diagram of a photonic crystal slab of silicon. Note the \mathbf{k} -space correspondence to a path of sequential points high symmetry. The distortion of the light line is a direct result of the particular path taken to high symmetry points. A photonic band gap is formed for even parity of the \mathbf{E} in the y -direction which corresponds to transverse electric (TE) modes.	20
2.6	At the "K" symmetry point, two possible field intensity profiles exist where the field is concentrated in either the air holes or the slab. A higher frequency is required to generate the same wavelength inside air than inside the slab. . . .	20
2.7	The band structure for a line defect (a) is shown in (b). Both TIR and the PBG create defect modes as indicated in the figure. The repetitive structure of the crystal lattice is only maintained in the x -direction and the defect needs to be padded with an infinite number of lattice periods. This changes the Brillouin zone from a hexagon to a narrow rectangle as shown in (c). Any modes with a non-zero k_z component are bulk PC modes that are smeared out when projected along the x -direction of the \mathbf{k} -path.	22
2.8	By mirror symmetry, an even and odd mode must exist for a symmetric waveguide with the field distribution described in the figure. Light initially launched at \mathbf{A} can be expressed as a superposition of even and odd modes. Since these modes generally travel at different speeds, the relative phases between the even and odd superposition will gradually change until the power is effectively exchanged to the opposite waveguide at \mathbf{B}	23
2.9	(a) Two waveguides initially separated by W form a directional coupler of length NL_c . (b) A simple model may be constructed describing the transmission change due to out-of-plane deflections d assuming negligible cross section in each waveguide and exponential decay of the EM fields.	24
2.10	The expected optical response as seen at both output ports for $N = 1/4, 1/2,$ and 1 as a function of out-of-plane deflection.	26
3.1	The PCDC design concept showing the released photonic crystal membrane. Light enters the photonic crystal split-line defect and couples to the adjacent side. Deflections in the PC membrane alter the observed transmission.	29

3.2	Cross section of SOI wafer. Three different etch depths are offered using the IMEC process which can be used to create rib (a&b) and channel waveguides(c). (d) Overall, the SOI wafer has a top layer silicon layer of 220nm followed 2000nm of silicon dioxide followed by 2mm of silicon. (e) Scanning electron microscope image of a triple-etch depth surface grating coupler.	30
3.3	For a $T = 220\text{nm}$, the key design constraints that dictate the bulk PC parameters Λ and D are shown which include the presence of the desired wavelength in the PBG and the 120nm resolution of the design rule checker. The cross-hair represents the selected design parameters $\Lambda = 450\text{nm}$ and $D = 270\text{nm}$	31
3.4	Band structure for \mathbf{E} in-plane at mid-slab inside the bulk silicon photonic crystal structure surrounded by air. The desired 1550nm wavelength is observed to lie within the photonic band gap which extends from 1313nm to 1681nm. PC dimensions: thickness 220nm, pitch 450nm, and hole diameter 270nm.	32
3.5	Symmetric line defect representing the directional coupler	33
3.6	The isolated defect is shown in (a). The bandwidth of the defect modes is plotted as a function of E in (b). A slice of this parameterization is projected in (c) which shows the defect band structure for $E = 1.2\Lambda$. Here, the desired wavelength crosses a dielectric mode (black dots), indicated by negative slope. A surface mode (open circles) may be seen near the top of the PBG indicated by positive slope.	33
3.7	The bandwidth of two possible sensor configurations which use dielectric and surface modes which pass through the desired wavelength at $E = 0.25\Lambda$ and $E = 1.2\Lambda$ respectively.	34
3.8	The defect band structure for PCDC designs of ($E = 0.25\Lambda, W = 1.22\Lambda$) and ($E = 1.2\Lambda, W = 0.44\Lambda$).	34
3.9	The PCDC FDTD domain is shown. A close up of the PC waveguide junction is depicted in units of nanometres. The hatched region is the 150nm partial etch depth of the rib waveguide. The FDTD domain was constructed using a parameterized script which may found in Appendix C.	36
3.10	The out-of plane component of the magnetic field at mid-slab for $\lambda = 1550\text{nm}$ and $L_{MEM} = 12.47\mu\text{m}$ (28 PC holes) is simulated using FDTD. Light enters the upper port and propagates from left to right. Energy is clearly transferred from the excited port to the coupled output forming a half-bridge coupler. The outline of the PCDC structure is also shown.	36
3.11	The relationship between L_c and wavelength as the air gap varies is shown. . . .	37
3.12	The transmission output spectra is shown for the $N = \frac{1}{2}$ bridge sensor.	37
3.13	The normalized transmission characteristics for three different sensor lengths (a) $L_{MEM} = L_c$, (b) $L_{MEM} = L_c/2$, and (c) $L_{MEM} = L_c/4$ are plotted as a function of out-of-plane membrane deflection at 1550nm and air gap separation 200nm. . .	38

3.14	The basic design of the PCDC sensor. The top silicon layer, 150nm etch depth, and the etched BOX are indicated by the grey, hashed grey, and white regions, respectively. The sensor length is some multiple of the coupling length $L_{MEM} = NL_c$. The mechanical properties of the sensor is largely controlled by the strut length L_{str}	39
3.15	The relationship between the critical buckling load and strut length is shown for a membrane length of $L_{MEM} = 12.7\mu\text{m}$ and $L_w = 15.8\mu\text{m}$. Also shown in the relationship between out-of-plane stiffness and strut length.	40
3.16	A rib waveguide (top) and photonic crystal (bottom) based $\frac{1}{4}$ -bridge directional couplers are shown. For an air gap separation of 200nm and waveguide width 540nm the coupling length is reduced thirteenfold.	42
3.17	Post-buckling simulation procedure	43
3.18	Expected buckling amplitude as a function of intrinsic SOI strain σ_0 . The strut length is approximately $21\mu\text{m}$	44
3.19	The COMSOL generated force-deflection curve is shown for parametrically prescribed displacements for the 28-hole buckled structure with specifications found in Table. 3.2. The initial buckling amplitude was set to 500nm corresponding to a reasonable initial stress of about 50MPa. The snap-through event can be seen to occur at about $0.3\mu\text{N}$ of force.	44
3.20	(a) The in-plane stiffness may be dramatically decreased using a (b) microbeam array with multiple beams. Figure based on [76]. (c) These structures may be integrated into the current PCDC design.	45
4.1	The process flow of the PCDC fabrication including IMEC and Nanofab processes.	48
4.2	Overview of the MPW dicing process and layout. An eight inch wafer includes about 120 repeated reticles etched using stepped UV lithography. The PCDC project workspace is $3\text{mm} \times 2\text{mm}$	49
4.3	The sum $2E + W$ is assumed to be stable despite fabrication biasing.	49
4.4	SEM image of a IMEC run half-bridge structure before HF under-etching. Structures with design No. X01 contain the correct hole radius and air gap separation.	53
4.5	SEM image of buckled mitigated design using a micro-beam array structure. . .	53
5.1	The control system for the SiP MIP with customized with an AFM driver (yet to be integrated). The MATLAB GUI allows the die stage ($\Delta x = \Delta y = 100\text{nm}$) to moved and select a device for testing.	55

5.2	(a) Overall optical test bench is shown. (b) Close up of the fiber array and chip stage. (c) Fiber array cross section with 1-4 ports TM polarization and 5-8 ports TE polarization. (d) The CCD camera is set at an angle with respect to the chip and can only focus on the SGCs. (e) The interstitial fiber array, shown with the polarization labeled, distance is $127\mu\text{m}$, providing a unit of reference.	56
5.3	Blank device transmission characteristics for associated fiber array angles (a) 5 degrees, (b) 10 degrees, and (c) 15 degrees away from the vertical. A 10dBm source with 1460–1610nm wavelength sweep and 1s settling time was used to generate the spectrum.	60
5.4	Normalized transmission of PCDC devices of length (a) $12.77\mu\text{m}$ and (b) $14.57\mu\text{m}$ are shown. Using the transmission minima and crossing points, the coupling length may be inferred at the corresponding wavelength. Near 1578nm, the coupling length changes rapidly due to zone folding of the even mode.	61
5.5	Plots of the observed coupling lengths for Tables 5.1 and 5.2. The coupling lengths as predicted by FDTD simulation are included for the same air gap width of 200nm.	62
5.6	The FDTD simulation of the normalized transmission of PCDC devices of length (a) $12.77\mu\text{m}$ and (b) $14.57\mu\text{m}$ are shown. Although a 20nm wavelength deviation is observed with respect to the measured spectrum, the shape and loss agree.	62
5.7	Summary of the optical profilometry results. A comparison of the compensated and uncompensated structures demonstrates significant reduction in buckling.	63
6.1	By flip bonding an etched wafer to the PCDC device and substrate, a sealed cavity may be formed.	66
6.2	(a) Overall picture of current AFM apparatus. The focused light from the laser is reflected on to the AFM tip using tunable mirrors. (b) Close up view of a sample chip loaded onto the AFM stage tip. The AFM tip is very small and can only be seen on under microscope as shown in (c) where it is ready to exert a force on a PC membrane measuring approximately $20 \times 20\mu\text{m}^2$	67
A.1	A Yee lattice, used almost universally in FDTD routines, provides a natural arena for computing curls and line integrals	78
D.1	Fixed-fixed buckling of a beam under axial loading	89

List of Tables

1.1	Estimated micromechanical properties [36] and thermal properties of common MEMS materials [35]. ρ =density, E=Young's modulus, ν =Poisson's ratio, σ_y =yield strength, σ_{max} =ultimate/fracture strength, α =coefficient of thermal expansion, T_m =melting point	4
1.2	Comparison of State-of-the-Art Sensors Characteristics [37, 38, 39, 40, 41, 42, 43, 44, 45, 46, 47, 48, 49, 50, 51, 52, 53].	4
2.1	Table of Parity Relationships [80]	21
3.1	The PCDC sensor performance at various specifications. $\lambda = 1550\text{nm}$	43
3.2	The PCDC sensor performance at various specifications. $\lambda = 1550\text{nm}$	43
3.3	A comparison of buckle-compensated and uncompensated designs. The critical buckling load may be dramatically increased without major consequence	46
5.1	#401 Coupling Lengths (with BOX) $L_{MEM} = 12.77\mu\text{m}$ (28 Holes)	58
5.2	#403 Coupling Lengths (with BOX) $L_{MEM} = 14.57\mu\text{m}$ (32 Holes)	58

List of Appendices

Appendix A Finite-Difference Time-Domain	78
Appendix B Plane Wave Expansion	81
Appendix C FDTD Script (Lumerical)	83
Appendix D Buckling Analysis	89
Appendix E Project Specifications	92

List of Abbreviations, Symbols, and Nomenclature

AFM	<i>Atomic Force Microscope/Microscopy</i>
BOX	<i>Buried OXide</i>
CMOS	<i>Complementary Metal-Oxide-Semiconductor</i>
DRC	<i>Design Rule Checker</i>
EM	<i>Electromagnetic</i>
FDTD	<i>Finite Difference Time Domain</i>
MEMS	<i>Microelectromechanical System</i>
MOEMS	<i>Micro-optoelectromechanical System</i>
PBG	<i>Photonic Band Gap</i>
PC	<i>Photonic Crystal</i>
PCDC	<i>Photonic Crystal Directional Coupler</i>
PDMS	<i>PolyDiMethylSiloxane (silicon based polymer)</i>
PEEK	<i>Polyether Ether Ketone (organic thermoplastic)</i>
PML	<i>Perfectly Matched Layer</i>
PWE	<i>Plane Wave Expansion</i>
QCM	<i>Quartz Crystal Microbalance</i>
SOI	<i>Silicon On Insulator</i>
TIR	<i>Total Internal Reflection</i>
WDM	<i>Wavelength Division Multiplexing</i>

Λ	<i>Photonic crystal slab lattice pitch</i>
λ	<i>Wavelength of light</i>
ω	<i>Frequency of light</i>
κ	<i>The difference between even and odd propagation constants</i>
ϵ	<i>Dielectric constant</i>
σ_0	<i>Compressive top layer SOI strain</i>
σ_{crt}	<i>Critical buckling load of PCDC</i>
A	<i>Sensing area of microsensor</i>
d	<i>Out-of-plane membrane or waveguide displacement</i>
D	<i>Photonic crystal hole diameter</i>
E	<i>Width of extended edges of PCDC</i>
f_0	<i>Mechanical resonance</i>
H	<i>Magnetic field phasor</i>
$k_{e,o}$	<i>Even (e)/Odd (o) propagation constant</i>
$k'_{e,o}$	<i>Even (e)/Odd (o) propagation constants normalized to PC pitch</i>
k_s	<i>Out-of-plane stiffness</i>
L_c	<i>Coupling length</i>
L_{MEM}	<i>Length of PCDC membrane</i>
L_{STR}	<i>Length of PCDC membrane support members</i>
L_{TOT}	<i>Total length of the PCDC membrane including support members</i>
L_w	<i>Width of PCDC membrane support members</i>
N	<i>Length of PCDC membrane in terms of L_c</i>
n	<i>Index of refraction</i>
S_{opt}	<i>PCDC optical sensitivity full scale per nanometer</i>
S	<i>PCDC optomechanical sensitivity full scale per kilopascal</i>
w	<i>In-plane directional coupler waveguide separation parameter</i>
W	<i>Fixed in-plane directional coupler waveguide separation</i>

Chapter 1

Introduction

1.1 Micromechanical Markets and Trends

Micromechanical sensors are used for measuring pressure, acceleration, viscosity, flow, force, torque, stress, sound, and fluid concentration. The operating principle of these sensors generally relies on the deformation of a micromachined membrane or cantilever. The deformation of these structures may be transduced either through changes in local material properties, as is the case for piezoresistive sensors, or by changes in element separation as seen in capacitive-based devices.

As of 2011, the pressure sensing domain alone was a multibillion dollar industry expected to reach a market size of \$7.34 billion by 2017 [1] with a 6.3% compound annual growth rate¹. The primary factors contributing to this growth include rising vehicle production, government legislation, and emerging foreign economies. Other important market pressures lie in the medical sector, environmental monitoring, petroleum engineering, aerospace research, process engineering, in addition to the rise of "big data" collection systems. Yet, perhaps the most important factor contributing to sensor growth, has been the successful leveraging of matured micromachining technology.

Complementary metal-oxide-semiconductor (CMOS) process technology, which involves UV-lithographic nanopatterning of silicon, has dominated the integrated circuit market [2] and represents an attractive cost-effective path to miniaturization and mass production currently exploited by many microelectromechanical systems (MEMS) and micro-optoelectromechanical systems (MOEMS) devices [3]. Silicon based sensors have followed Moore's law dropping from \$1000 in 1960s to less than 50 cents per die today [4]. Packaging, however, remains an important consideration accounting for up to 75 percent of the manufacturing costs of micro-sensors [5].

Many legislative factors involving car safety and environmental monitoring have placed

¹CAGR = $\left(\frac{\text{Future Value}}{\text{Beginning Value}} \right)^{\frac{1}{\# \text{ of yrs.}}} - 1$

greater demand on inexpensive sensor technologies [6]. Green initiatives such as Ontario's Drive Clean (1999) [7], US Clean Air Act (1990) [8], and European Emission Standards Stages EURO 1-6 (1993-2014) [9] have all mandated reduction in vehicle emissions. Presently, pressure sensors are being used to monitor tire pressure (TPMS), airbag deployment (SRS), exhaust pressure (EGR) and increasingly in engine control units (ECU) in order to optimize fuel economy [10]. Automotive sensors must be extremely robust; resistant to shocks, elevated temperature, harsh chemicals, clogging, and electromagnetic interference (EMI). There is currently a need for robust sensors placed inside the engine for ignition timing where conditions widely vary exceeding 30MPa and 1500°C.

The miniturization of silicon microsensors has found utility in the medical field due to the low power consumption and biocompatibility making it well suited for implantable systems and *in situ* measurements. As monitor devices, pressure sensors may be used as catheters, intracranial sensors, intraocular implant [11], heart monitors [12, 13], artificial ears [14], and bladder pressure monitors [15]. Desirable qualities of implantable systems, specifically wireless systems, is biocompatibility, low-power consumption, small form factors, and EMI immunity which make optical apparatus an attractive option.

Photoacoustic tomography (PAT) is an emerging medical imaging technique based on ultrasonic transducers that can detect the acoustic signals generated by photothermal excitation of deep tissue using a pulsed laser. Acoustic signal acquisition is done by either mechanically scanning a focused transducer or with fixed sensor arrays. As sensor arrays, small transducer apertures (<1mm [16]), high mechanical resonances (1–50MHz [17]), and channel bandwidth [18] are important for rapid submillimetre resolution of soft tissue [19]. Applications of PAT include intravascular imaging [20], melanoma detection [21], and minimally invasive breast cancer screening [22, 23] which maybe important to reducing unnecessary medical testing and radiation doses.

In order to study chemical/biochemical reactions with minimal consumption of reagents, micromechanical sensors have also been successfully integrated in microfluidic environments, providing real-time analysis as flow sensors on a variety substrates including silicon [24], pyrex [25], polydimethylsiloxane (PDMS) [26], glass and polyether ether ketone (PEEK) [27]. As flow meters, discrete pressure sensors are typically distributed along the length of microchannel. The difference between measured pressures may be used to determine the flow rate using the following equation [27].

$$\frac{P}{F} = \frac{128\mu L}{\pi D^4} \quad (1.1)$$

where P is the pressure difference across a cylindrical channel of length L and diameter D , F is the volumetric flow rate, and μ is the fluid viscosity. This assumes laminar flow which is characterized by Reynold's number $Re = Du\rho/\mu < 2000$ where u is the average linear velocity and ρ is the fluid density. Using silicon-based capacitive MEMS sensors with 100–150 μ m sensing diameters, differential pressures up to 200kPa across a microfluidic channel can be

related to the flow rate of water of 0.01–100mL/hr [24]. Developing lab-on-chip microsystems is not only relevant to bio-chemical R&D but may also serve as an inexpensive diagnostic tool leading to a more personalized healthcare; potentially saving millions of dollars and reducing MRI and CAT scan wait-times.

Purely optofluidic systems is a new and rapidly emerging field utilizing new technologies and low cost materials to produce sensitive microsensors [28]. Photonic crystal structures are known to be able to confine light to liquid-core regions despite the total internal reflection condition ($n_{clad} < n_{core}$) not strictly being satisfied in order to enhance light-matter interaction. Configurations currently being proposed are slotted PC structures [29], or hollow-core photonic crystal fibers [30].

The aerospace industry is enjoying the benefits of sensor miniaturization where weight and size reduction of sensor and associated instrumentation are primary design considerations [31]. Modern aircraft fly-by-wire avionics require high reliability, fast sensor response times, and EMI immunity while engine monitoring sensors need to operate at elevated temperatures [32]. Fluid research is also benefiting from the dense packing of sensors arrays where temperature and pressure sensors are able to monitor industrial flow processes. As sensor/actuator arrays, smart materials which can change shape according external stimulus have intriguing prospects for turbulent and laminar flow research [33] and is considered a future technology for advanced aircrafts [34].

1.2 Performance Characteristics

1.2.1 Material Properties

Silicon has favourable electrical, optical, and mechanical properties and is widely available as single-crystal wafers making it well suited for MEMS applications. Silicon may be either n or p doped in order to adjust its electrical properties and can be easily integrated with electronics. Silicon also has robust mechanical properties at MEMS scales when compared to alternative materials as shown in Table 1.1. The Young's modulus of single crystal silicon is nearly as high as steel (200GPa). High Young's moduli are desirable due to improved linearity between applied load and deformations [35].

Silicon-on-insulator (SOI) is becoming a popular substrate choice due to its CMOS technology compatibility. The SOI wafers include an oxide layer sandwiched between a silicon thin film and an extended silicon substrate. The oxide layers provides thermal isolation and allows cavities to be formed after subsequent under-etching of the top silicon layer.

Table 1.1: Estimated micromechanical properties [36] and thermal properties of common MEMS materials [35]. ρ =density, E=Young's modulus, ν =Poisson's ratio, σ_y =yield strength, σ_{max} =ultimate/fracture strength, α =coefficient of thermal expansion, T_m =melting point

Material	ρ [g/cm ³]	E [GPa]	ν	σ_y [GPa]	σ_{max} [GPa]	α [10 ⁻⁶ /°C]	T_m [°C]
Aluminum	2.7	70	–	–	0.15	25	660
Copper	8.9	120	–	0.15	0.35	16.56	1085
Gold	19.3	70	–	–	0.30	14	1064
Nickel	8.9	180	–	0.30	0.50	13	1455
Nickel-iron	8.1	120	–	0.70	1.60	1.2	1700
Diamond-like carbon	3.5	800	0.22	–	8.0	1	N/A
Polysilicon	2.3	160	0.22	–	1.2–3.0	2.8	1414
Silicon crystal	2.3	125–180	–	–	>1.0	2.33	1414
Silicon carbide	3.2	400	0.25	–	–	3.3	2300
Silicon nitride	3.1	250	0.23	–	6.0	0.8	1930
Silicon oxide	2.27	70	–	–	1.0	0.5	1700

1.2.2 Overall Transduction Performance

The performance of MEMS and MOEMS devices depends primarily on material selection, structural geometry, transduction method, and signal conditioning. Capacitive, piezoresistive, and piezoelectric transduction methods are popular for MEMS while intensity, spectral, interferometric, and polarization based transduction methods are commonly used for MOEMS [37]. While most sensors can be designed to operate under a variety of pressure ranges, the dynamic range and resolution is limited by noise, transduction linearity, and analog to digital converter performance. A comparison of popular transduction methods currently being researched is summarized in Table 1.2.

Table 1.2: Comparison of State-of-the-Art Sensors Characteristics [37, 38, 39, 40, 41, 42, 43, 44, 45, 46, 47, 48, 49, 50, 51, 52, 53].

	Capacitive	Piezoresistive	Fabry-Perot Fiber
Cost	Low to moderate	Low to moderate	High
Power Consumption	Low to very low	High	High
Sensitivity	1–20fF/kPa	30–150(mV/V)/MPa	0.004–70nm/kPa
Resolution	0.1–0.025% FS	0.01–0.002% FS	10–0.0005% FS
Min sense area	1000–100 μ m	1000–50 μ m	1000–125 μ m
Max Temperature	225°C	125°C	700°C

1.2.3 Piezoresistive Sensors

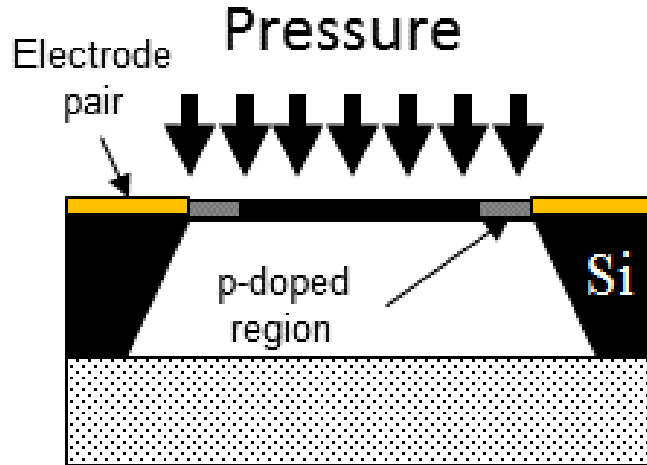


Figure 1.1: Cross section of piezoresistive-based sensor. Doping enhances the piezoresistive effect and is generally done near regions of high-stress.

With good linearity, dynamic range, and low cost, piezoresistive sensors represent the most popular choice for pressure sensing applications. As the name suggests, these sensors rely on the piezoresistive effect where changes in strain warp the electronic band structure and carrier mobilities [54] which may be interpreted as changes in conductivity. Piezoresistors are frequently arranged in Wheatstone bridge configurations and placed in high-stress regions, typically near the clamped regions of a diaphragm as shown in Fig. 1.1. Best quality has been achieved with doped (p-doped 10^{15} – $10^{22}/\text{cm}^{-3}$ is common [55]) single-crystal silicon which lends itself to CMOS friendly technologies. CMOS technology compatibility is important as signal processing electronics may be integrated monolithically thereby improving the form factor and reducing manufacturing costs.

The major drawback of piezoresistive sensors is the decrease in performance with temperature due to $1/f$ and Johnson-Nyquist noise which thermalize the piezoelectric band structure, limiting sensor resolution. The voltage noise density due to these effects is given by equations (1.2) and (1.3).

$$V_{1/f} = V_{bias} \sqrt{\frac{\alpha}{Nf}} \quad (1.2)$$

where V_{bias} , f , and N are bias voltage, frequency, and total number of carriers in resistor volume, respectively, with α being determined empirically.

$$V_J = \sqrt{4k_BTR} \quad (1.3)$$

where T , R , and k_B are temperature in Kelvin, piezoresistance, and Boltzmann's constant respectively. Piezoresistive sensors therefore require signal conditioning to offset thermal effects, although temperatures as high as 600°C have been achieved with isolation packaging [56]. Thermal effects may be mitigated by increasing doping levels, but this inevitably decreases sensitivity.

The performance of piezoresistive sensors might also be improved by either enhancing the strain near the piezoresistive element or by increasing the interrogating current. Practically, both approaches are limited as an increased current will heat the sensing element. Furthermore, enhancing the strain by structurally weakening the sensing regions exacerbates current-loading effects and is limited by the mechanical stability of the membrane itself. Ultimately, advances in piezoresistive sensors lie in material science. Presently, there is active research on using graphene [57], carbon nanotubes [58], and SiC [59] as piezoresistive elements.

1.2.4 Capacitive Sensors

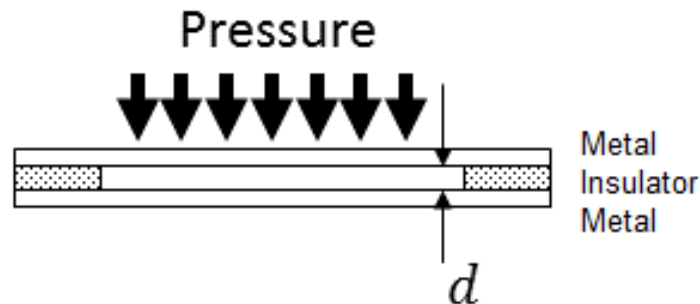


Figure 1.2: Capacitive-based MEMS sensors detect the changes in capacitance based on microplate spacing.

For highly accurate low-power applications, capacitive MEMS sensors are an attractive technology. Capacitive MEMS devices utilize the change in capacitance between closely spaced microplates as shown in Fig. 1.2. Capacitive sensors have better thermal characteristics than piezoresistive sensors. However, since the ability to detect capacitance is limited (0.5fF for industrial applications [37]), the resolution is fundamentally related to sensor area as shown by equation (1.4).

$$C = \frac{\epsilon A}{d} \quad (1.4)$$

where C , ϵ , A , and d are capacitance, dielectric constant, area, and plate separation. Moreover, highly sensitive capacitive sensors require small plate separations of only few microns making them prone to contamination and stiction effects that render the sensor unusable. The deflection dependency also makes the sensor highly nonlinear. These are overcome by use of contact modes that extend the dynamic range of the device.

1.2.5 Micro-optoelectromechanical Systems (MOEMS)

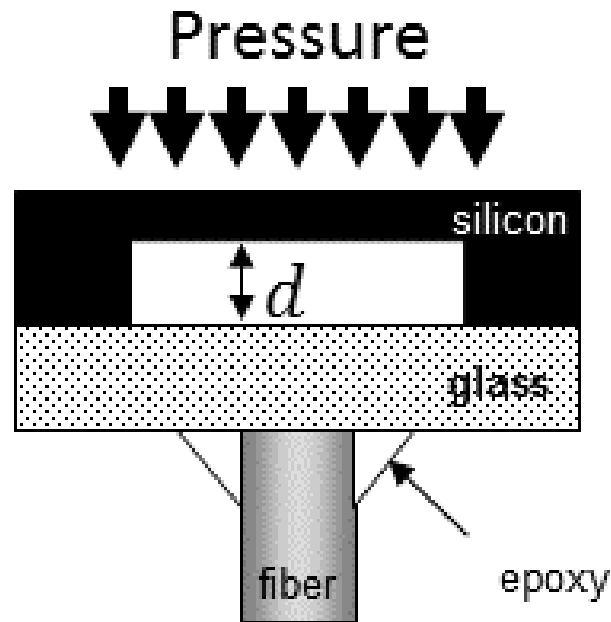


Figure 1.3: Cavity-based optomechanical sensor is shown bonded to fiber optic cable which can be based on either changes in reflected intensity or colour. Intensity changes may be observed as based on the position of the reflective membrane and fiber optic properties. Changes in colour may be observed as membrane deflections change the optical resonant properties of the cavity.

A variety of novel devices which optically interrogate pressure and deflection exist. There are many benefits to using optical configurations such as very high sensitivity, excellent thermal response, and EMI immunity, yet there are unique challenges with optical formats such as material absorption, and drifts in source intensity and detector response. In perhaps the simplest arrangement, the intensity of light reflecting off a sealed diaphragm is a function of deflection according to the inverse square law shown below in equation (1.5) [60].

$$\frac{P_r}{P_t} = \frac{D^2}{(2d \tan \theta)^2} \quad (1.5)$$

where P_r , P_t , D , d , and θ are the reflected power, transmitted power, fiber core diameter, cavity separation, and fiber-optic acceptance angle, respectively. These devices generally have low dynamic range due to the inherent non-linearity of the inverse square relationship. Intensity-based sensors also suffer from calibration issues due as the effects of sensor membrane deflection cannot be distinguished from intensity changes due to optical fiber bending [37].

Spectral interrogations have been more successful in achieving high resolution due to interferometric instrumentation that can detect wavelength changes as low as a few pm [50]. Typically by cleaving, fusing, and wet-etching, a sealed optical cavity can be formed at the tip of an fiber creating an Fabry-Perot (FP) optical resonator as shown in Fig. 1.3. Due to interference, the spectrum of light that is reflected from such a cavity is a series of wavelength minima separated by the free-spectral range (FSR). By exerting pressure, the cavity length is compressed causing an observable spectral shift of wavelength minima according to (1.6) [52].

$$\Delta d = \frac{\Delta \lambda_m}{\lambda_m} d \quad (1.6)$$

where d , and λ_m is the cavity separation and position of a wavelength minima, respectively. FP sensors are very robust with some apparatus being able to withstand temperatures as high as 710°C [53] and are presently sold commercially [61]. Similar spectral effects are also present with the stretching of fiber Bragg gratings (FBG) [62] and the deflection of ring resonators [63] with efforts being done to further integrate instrumentation on-chip using silicon photonic structures such as arrayed waveguide gratings (AWG) [64]. Excellent performance may be achieved with FP sensors; however, the cost of associated instrumentation remains quite high.

1.3 A Case for Photonic Crystal Directional Coupler Sensors

Despite countless devices being developed which use gratings and photonic crystals to enhance light-matter interactions [62, 29], surprisingly very little work is being done specifically on how photonic crystals (PC) might be used to enhance displacement sensors outside of our research group. Our previous PC-based sensor designs involve a vertical cavity created after under-etching the SOI oxide as shown in Fig.1.4 [65]. Light may be confined to propagate along the PC defect and a portion of transmitted power can couple into the bottom substrate. Applying pressure on the PC membrane draws the defect closer to the bottom substrate enhancing the coupling and increasing the optical power leakage into the substrate. The change in transmitted intensity (or reflected intensity [66]) can be related to the exerted pressure. The optical resonant properties of PC defects are known to significantly reduce the physical length needed for coupling to occur. Our group has previously been able to demonstrate displacement sensor enhancement using our patented [67] thin-film photonic crystal membranes [68, 69].

This thesis builds on these previous efforts that have successfully exploited the optical resonant properties of photonic crystals; however, this is the first such effort to investigate PC

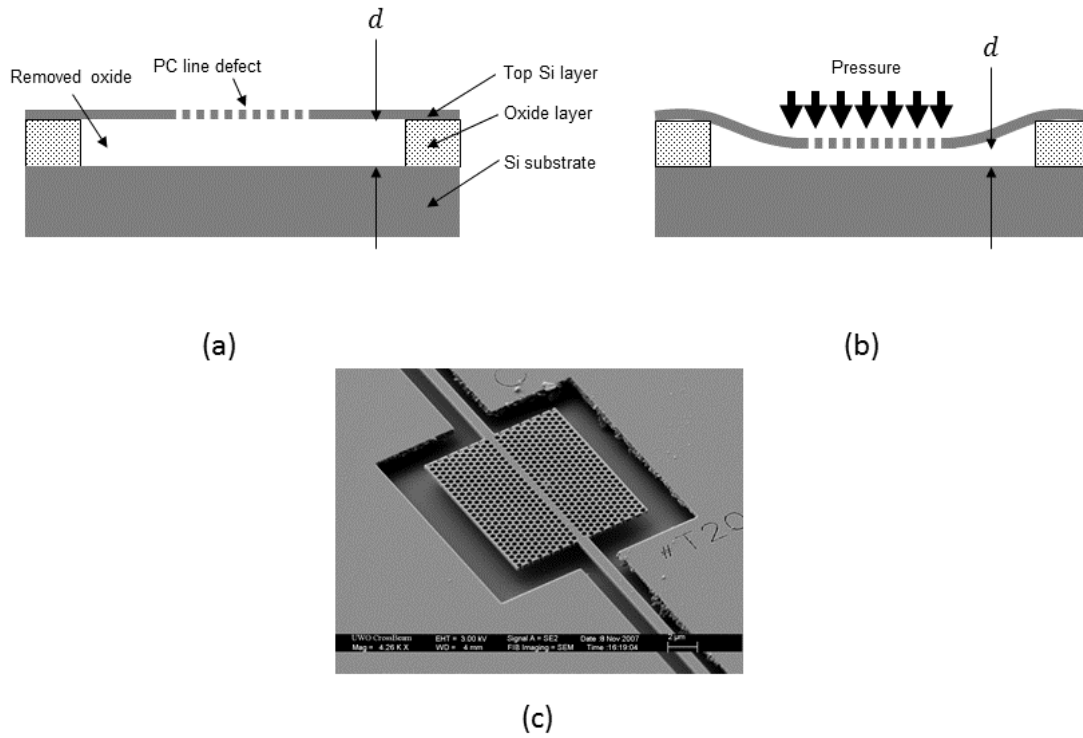


Figure 1.4: PC-based vertical cavity pressure sensor previously investigated by our research group. (a) Unloaded sensor cross section showing supported membrane and under-etched SOI. (b) Exerting pressure on the membrane brings the PC line defect closer to the bottom substrate. Light propagating along the PC defect leaks into the bottom substrate and decreases the transmitted intensity (c) scanning electron microscope image of the PC membrane and line defect.

displacement sensing in the context of a *directional coupler*. By using a directional coupler topology, it is hoped a strictly in-plane CMOS-compatible design may be implemented that may also allow for signal normalization and overcome stiction issues that were associated with previous PC designs and capacitive MEMS sensors. The PCDC is an edge-based phenomena requiring only 5–7 rows of PC holes for good confinement. Indeed, the in-plane nature of PCDC sensor designs allow them to be fabricated on SOI without predilection towards a particular buried oxide thickness, therefore relaxing SOI buried oxide constraints.

If we consider a directional coupler, where light periodically cycles between two waveguides when they become close, we can conceive a device that alters the transmission of light by deflecting one of the waveguides; that by changing the separation between the two waveguides, the characteristic cross-over length will be altered and the transmission will be modulated. In terms of photonic crystals, it is known that photonic crystal directional couplers (PCDC), as shown in Fig. 1.5, are able to reduce coupling lengths down to $10\mu\text{m}$ [70, 71], more than ten times shorter when compared with traditional index based waveguides. Extending this con-

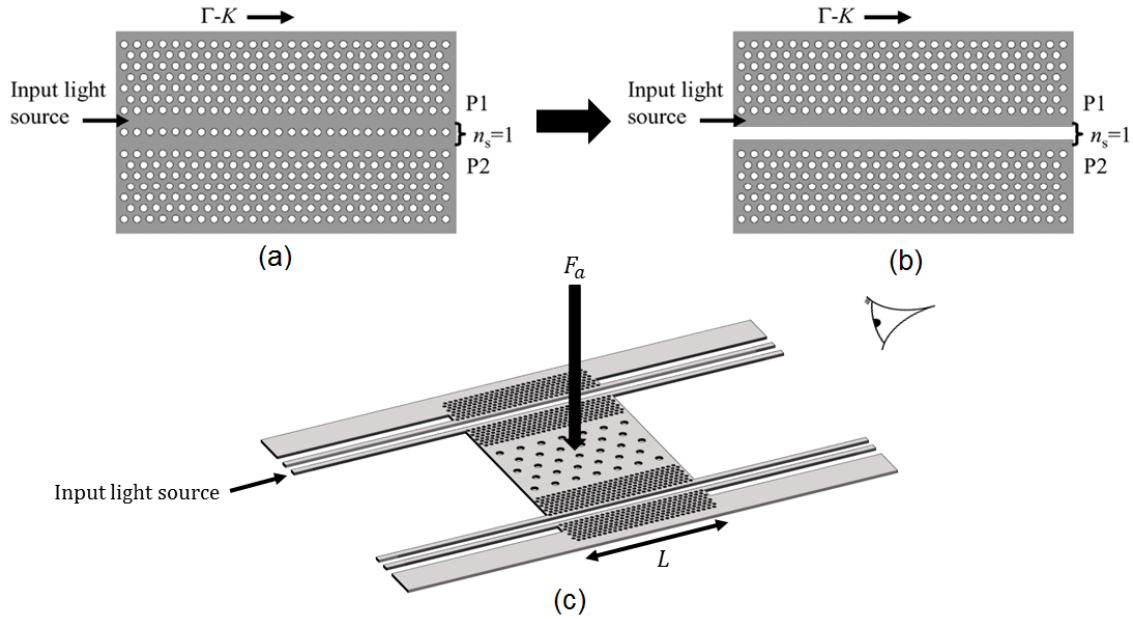


Figure 1.5: Design concept: (a) PCDCs are known to significantly reduce coupling lengths. (b) By isolating the waveguides, (c) a membrane may be formed and modulate the observed transmission.

cept by replacing the central line of holes with an air gap allows each side to be mechanically isolated and a membrane structure can be formed with one coupler on each side.

The small scale of the sensor should yield extremely high mechanical resonances resulting in faster response times. The compressed coupling lengths drastically reduce the unwanted pre- and post-coupling which occur between the interfacing waveguides as they approach the coupler, relaxing the integration engineering required. Additionally, if the supporting members are also made to serve as interfacing waveguides, all four ports of the coupler may be accessible allowing for signal normalization, providing immunity to source fluctuations.

Photonic crystals can be easily scaled, modeled, and created using any material given high enough index contrast between the PC and surrounding medium. It is thought the key to creating high temperature sensors is the use wide band gap materials (e.g., SiC, Diamond) which have stable optical, electronic, and mechanical properties at high temperature (i.e. dn/dT $6 \times 10^{-5}/^\circ\text{C}$ for SiC [72] when compared with silicon (i.e. dn/dT $2.5 \times 10^{-4}/^\circ\text{C}$ [73]).

There are unique spectral qualities of PC assisted couplers. PC coupling lengths have a quadratic-like dependence on wavelength leading to up a five-fold increase in coupler bandwidths up to 100nm [74, 75]. The increase in bandwidth may be useful for reducing design parameter sensitivity and, perhaps, help to mitigate thermal-related spectral shifts and enable inexpensive LED/detector integration. Moreover, the optical channel utilized by PCDC sensors may allow intensity-based wavelength division multiplexing (WDM) schemes to be implemented that may become important in highly parallelized applications.

1.4 Objectives and Thesis Layout

The main contribution to knowledge of this thesis is the investigation of the split line photonic crystal defect and its properties as an out-of-plane mechanical sensing element. As a figure of merit, the PCDC sensors were designed around a 200kPa sensing range as described in the microfluidic reference [24]. The main objectives of this thesis are listed below

- Develop a design strategy for creating a PCDC sensors on SOI using C-band (1530–1565nm)
- Integrate structures to mitigate buckling effects in SOI
- Fabricate and validate the operating principle of the PCDC
- Fabricate and validate buckle-compensated design

The PCDC sensors were designed on silicon on insulator (SOI) across C-band frequencies (1530–1565nm). A PCDC designed on SOI allowed the use of affordable high resolution foundry technologies. The C-band is selected as it represents the transmission window of minimal attenuation for popular silica based fiber-optical cables.

Since the PCDC sensor is based on the separation of adjacent slab edges, it is crucial that the resting position of the sensor lie in a predictable location. For larger PCDC designs, spring-like structures in the form of microbeam arrays are employed and are known to relax the unpredictable compressive strain that exists the top layer of flip-bonded SOI wafers. Without the microbeam array, the compressive strain can cause the PCDC membrane to buckle to an unpredictable out-of-plane resting position.

For this thesis, two batches of PCDC sensors were fabricated. The first batch was fabricated using the IMEC process at the ePIX foundry that featured high resolution triple-etch depth surface machining of SOI. This process also allowed access to established surface grating coupler (SGCs) designs that enabled optical interfacing to the PCDC chip using optical fibers. SGCs implemented as arrays on the surface of SOI chips allow rapid prototyping and efficient use of the overall allotted design space. Devices in this batch are intended to be fully optomechanical devices after post-process wet etching of the buried oxide layer.

Due to the limited quantity of IMEC generated chips, a second batch of PCDC devices was fabricated at UWO Nanofab in order to calibrate the post-process wet etching and subsequent drying. Since the second batch lacks established triple-etch depth capabilities, the PCDC devices included in this batch are only for testing mechanical properties and surface profiling. Also included in this batch are buckle-compensated designs that feature microbeam arrays. The integrity of these PCDC designs after post-processing is confirmed using scanning electron microscopy (SEM) after critical point drying (CPD).

The optical transmission characteristics of the first batch of IMEC generated sensors was tested before the buried oxide was under etched. Pre-etched measurements allowed for rapid

validation of the split line PC defect while at its known in-plane location. The surface profiles of buckle-compensated and uncompensated designs included in the second batch were compared using optical profilometry in order to validate the compensation strategy. Full optomechanical testing of the PCDC sensor could not be completed due to unexpected delays in the test bench procurement.

1.5 Overview of Thesis

The discussion of current microsensor technology and photonic crystal research was provided in this chapter in order to set the stage and motivate investigation into PCDC based optomechanical sensors. There is an established need for cheap, highly sensitive, small, robust sensors. In chapter 2, photonic crystals, line defects waveguides, the photonic band gap, and the optical directional coupler are introduced. Chapter 3 demonstrates how these concepts can be used to design and model a PCDC sensor. The critical optical design parameters of the PCDC (pitch Λ , edge width E , coupler separation W , sensor length L_{MEM}) are determined using plane wave expansion (PWE) and finite difference time domain (FDTD) simulation. Mechanical aspects of the design consider the effect of intrinsic strain built into SOI during wafer fabrication which is known to cause buckling after release of the membrane. Microbeam arrays are employed to mitigate buckling effects.

PCDC sensor fabrication is presented in chapter 4 featuring CMOS-compatible SOI surface machining done using 130nm IMEC-ePIXfab. Post-process wet-etching, done here at UWO Nanofab, releases the photonic crystal from the BOX layer forming the membrane structure. Characterization of sensor geometry is done using scanning electron microscopy (SEM), in order to confirm the correct PCDC dimensions. The testing procedure and evaluation of the first generation PCDC sensors is detailed in chapter 5, where the first measurements of a newly assembled silicon photonic test bench are performed. The measured transmission spectra validating the PCDC operating principle and a confirmation of successful buckling mitigation is presented. Finally, Chapter 6 summarizes the unique features of PCDC based sensors and offers possible avenues for improving sensor performance.

1.6 Contributions

All words, figures, simulation results, and computer code (unless stated otherwise) in this thesis were done by me. The strategy used to design the PCDC sensor presented in Chapter 3 was developed by myself. The application of buckle-mitigated structures, first investigated by Iwase *et. al.* in 2012 [76], and their relevance to PCDC sensor design stabilization was first noted by myself.

Fabrication of the first generation optical devices was outsourced using the IMEC process

at the ePIX-fab through the 2014 Passives Silicon Photonics Workshop sponsored by CMC Microsystems. The surface grating couplers (SGC) included in the IMEC chip layout enabled optical interfacing and were provided courtesy of UBC and implemented as part of a component cell library. Nanopatterning and post-processing of the buckle-mitigated structures was done jointly with post-doc Dr. Aref Bakhtazad.

The silicon photonic microsystems integration platform (SiPh-MIP) was procured and developed by CMC Microsystems and assembled here at Western University jointly by me and Aref. The MATLAB graphical user interface (GUI) controlling the laser, chip stage, and alignment routines was done by Maple Leaf Photonics. Optical profilometry measurements were provided courtesy of Dr. Evgueni Bordatchev. Due to the MATLAB SiPh-MIP GUI being still in its beta phase, the laser transmission spectra from the PCDC sensor was aquired instead using a Labview program created by me. Subsequent processing and normalization of transmission data was performed by myself.

Chapter 2

Background

2.1 Introduction

The two key phenomena behind the operating principle of the PCDC sensor are optical waveguiding and the directional coupler. Optical waveguiding may be provided by a dielectric distribution that satisfies the total internal reflection (TIR) condition. Optical waveguiding may also be provided by the photonic band gap (PBG) of a photonic crystal, where optical resonant properties of the PC forbid the propagation of light. Using the PBG, light can be guided through a defect in an otherwise perfect crystal.

A directional coupler is formed wherever two waveguides are brought near to each other. At a fixed waveguide separation, light which is initially launched in one waveguide, will periodically exchange its power with the adjacent waveguide along the propagation length. By altering the separation between the two waveguides, the characteristic coupling length is changed and the output transmission can be modulated, forming a sensing element.

There is no exact closed-form analytic solution describing the photonic crystal sensor; however, numerical methods exist which are able to compute the electromagnetic fields. Plane wave expansion (PWE) and finite-difference time-domain (FDTD) simulations are used to design the optical response of the PCDC sensor. An introduction to these simulation methods is outlined in Appendices A and B.

2.2 Dielectric Slabs

Consider a slab of silicon surrounded by air with a thickness much smaller than its areal dimensions. Suppose light is launched into the edge of the slab. If the angle formed by the edge-normal and the impinging light rays is less than some critical angle θ_{max} , light will become confined inside the slab by the total internal reflection (TIR) as shown in Fig. 2.1. This critical angle may easily be calculated using Snell's law of refraction.

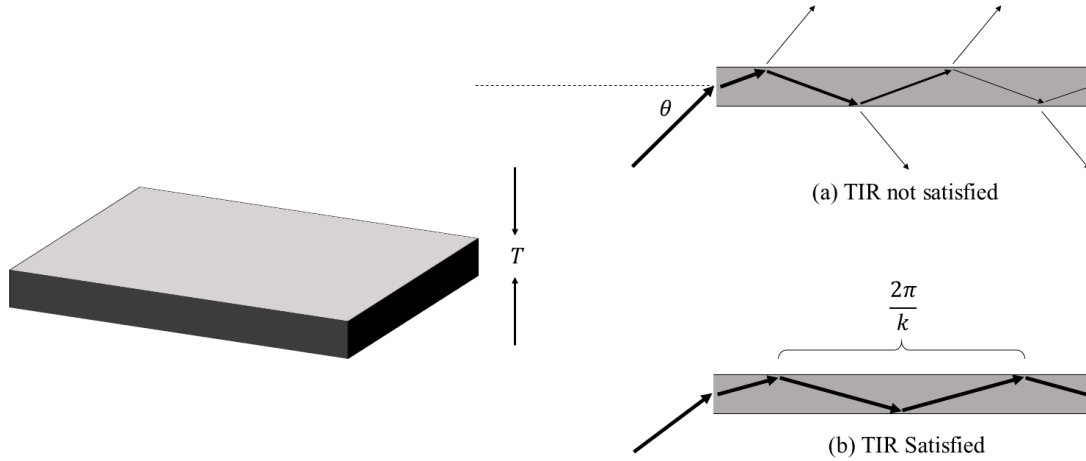


Figure 2.1: Light impinging on the edge of a dielectric slab is shown. Light which does not satisfy total internal reflection condition (a) is gradually diminished. Light which does satisfy TIR (b) is confined to lie inside the slab exhibiting distinct spatial and temporal symmetries

$$\theta_{max} = \sin^{-1} \sqrt{n_{glass}^2 - n_{air}^2} \quad (2.1)$$

where n_{glass} and n_{air} are the refractive indices of glass and air respectively.

Inside the slab, light will experience the numerous reflections and refractions at the top and bottom interfaces. If TIR is not satisfied, some of the light will radiate out of the slab during each interaction; exponentially diminishing in intensity as it advances further away from the edge. If TIR is satisfied, however, light is localized inside the slab and the perfect constructive interference condition leads to a discretization of light modes.

Light which is guided in this manner can be classified according to its symmetry, particularly its frequency ω and propagation constant \mathbf{k} of the mode in the waveguide. The frequency describes temporal symmetry, or how far in time we must travel until we see the same wave. Similarly, the propagation constant is associated with spatial symmetry, or how far in space we must travel until we see the same wave. Due to the in-plane symmetry of the dielectric slab, the direction of propagating light is arbitrary and the propagation constant may be represented as a scalar k quantity. The mode $\mathbf{H}(\mathbf{r})$ which represents the vector amplitude of the field, or its "shape", indicates where the field is mostly concentrated and the direction it points in. Regarding light in terms of its symmetry is crucial to understanding photonic crystals and interpreting how light propagates inside them. It is helpful to examine the dispersion diagram of the slab, as seen in Fig. 2.2, to see the relationship between these concepts. Due to continuous 2D symmetry, \mathbf{k} can be projected on to any arbitrary in-plane direction effectively making it scalar k .

The (ω, k) -plane is divided into two regions separated by the light line. Region I represents

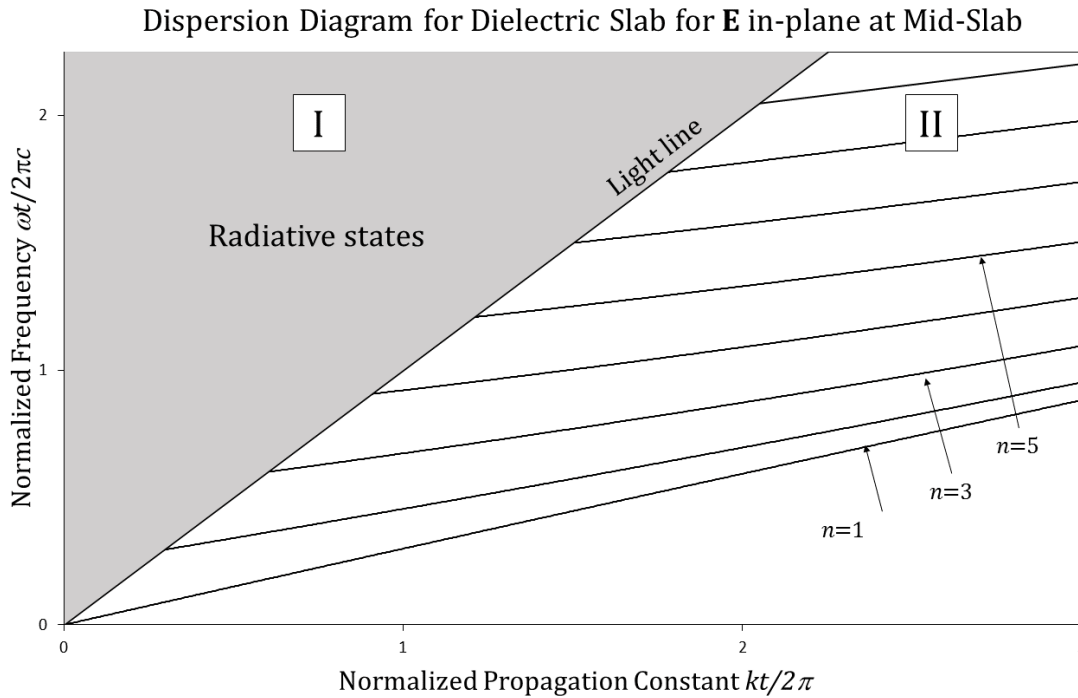


Figure 2.2: Dispersion diagram of a silicon slab $n_{Si} = 3.46$ normalized with respect to thickness t . For the first mode $n = 1$, the expected homogeneous propagation conditions is asymptotically reached quickly with increasing k . A singular mode can be made to exist in thin slabs where the free-space wavelength is of the same order as the thickness. In this case, the simple ray model breaks down and Maxwell's equations must be solved numerically.

the continuum of radiative modes which do not satisfy TIR. In this region, it is possible to couple light inside the slab with light on the surface of the slab. The mechanism for this is the k -matching at the air-silicon interface which satisfies the EM boundary conditions. The light line represents the extreme of this case where k is maximized by directing light exactly parallel with the slab (i.e. $\omega = ck$)¹. For larger k values, light is unable to couple outside the slab and must enter the slab from an edge facet.

Region II represents where the TIR condition is satisfied. Here, light is described by a discrete set of curves where perfect constructive interference occurs. The interference condition can be explained by in terms of ray optics. While completing a cycle, a light ray will pick up phase shifts associated with a pair reflections in addition to a phase shift associated with its propagation inside the slab. These phase shifts must add up to an integer multiple n of 2π for constructive interference to occur and provides a means of classifying modes by using n . Phase-matching represents the state of perfect constructive interference required for light to propagate indefinitely.

¹an exception to this is where the slab is bonded to a substrate. In this case, the slope of the light-line would be replaced by the reciprocal of the index of refraction of the substrate

2.3 Photonic Crystals

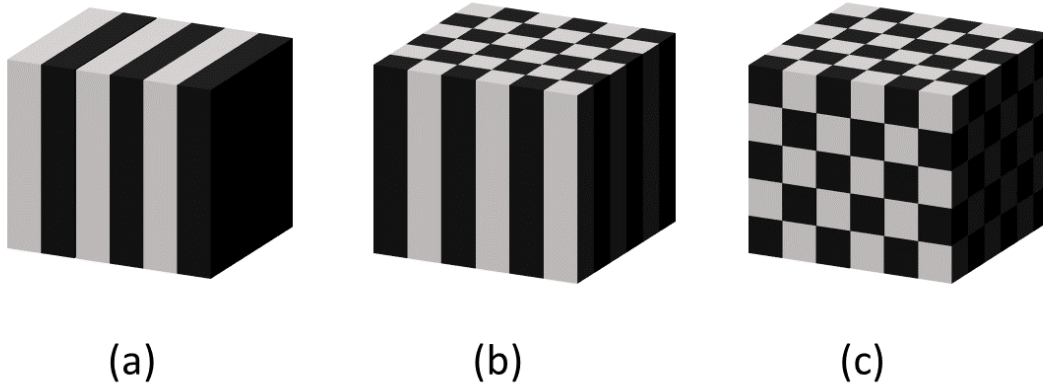


Figure 2.3: Crystals are, by definition, repetitive structures. (a) 1D, (b) 2D, and (c) 3D photonic crystal is shown composed of two dielectric materials

A photonic crystal is any periodic arrangement of dielectric media as shown in Fig. 2.3. Light impinging on the crystal will experience the many scattering events at all the dielectric interfaces. The collective interference of the light forms a periodic distribution of electromagnetic energy. However, under certain circumstances, no such distribution may exist and a photonic band gap (PBG) is formed [77].

The best way to understand PCs is by examining the interplay between Maxwell's equations and the symmetry present in dielectric media. The Bloch theorem emerges from the discrete translational symmetry present in the photonic crystal which implies a repetition of the dispersion diagram along \mathbf{k} -space. Thus, the only meaningful quantity to keep track of is the phase offset per lattice vector. This restricts the range of unique propagation constants to a 2π patch of the reciprocal lattice space. To see how this occurs, Maxwell's equations can be re-arranged into the vector Helmholtz equation for non-homogeneous dielectric media.

$$\nabla \times \left(\frac{1}{\epsilon(\mathbf{r})} \nabla \times \mathbf{H}(\mathbf{r}) \right) = \left(\frac{\omega}{c} \right)^2 \mathbf{H}(\mathbf{r}) \quad (2.2)$$

where $\mathbf{H}(\mathbf{r})$, $\epsilon(\mathbf{r})$, and ω are the magnetic field phasor, relative permittivity, and frequency of light respectively. Here, Maxwell's equations are expressed in Sturm-Liouville form which implies solutions must obey the superposition principle, yet more importantly, it implies the Helmholtz equation can be represented by a Hermitian operator² Θ and framed as an eigenvalue problem [78]

$$\Theta \mathbf{H}(\mathbf{r}) = \left(\frac{\omega}{c} \right)^2 \mathbf{H}(\mathbf{r}) \quad (2.3)$$

²A Hermitian operator is self-adjoint where the operator is equal to its conjugate transpose $A = A^\dagger$

where $\mathbf{H}(\mathbf{r})$ and $\left(\frac{\omega}{c}\right)^2$ are the eigenvector and eigenvalue respectively. Since information about the index periodicity is buried inside $1/\epsilon(\mathbf{r})$, this representation allows further classification of the state of light in terms of the eigenvalues of symmetry operators that commute with Θ . The eigenvalues of the symmetry operators are much easier to compute and give insight into the nature to the field inside the crystal.

The only observable feature of an EM field is the energy that is carried away by Poynting's vector [79]. This is due to the gauge invariance of the electron interaction with the EM field, which can arbitrarily adjust the global phase of the EM field. Thus, the EM field energy is directly related to the conjugate product of the magnetic phasor. And since the system is physically equivalent at each lattice point,

$$|\mathbf{H}(\mathbf{r} + \mathbf{R})|^2 = |\mathbf{H}(\mathbf{r})|^2 \quad (2.4)$$

where \mathbf{R} is any lattice vector. Consider now the effect of a crystal translation operator which takes the magnetic field phasor at \mathbf{r} and shifts it by a lattice vector \mathbf{R}

$$T_{\mathbf{R}}\mathbf{H}(\mathbf{r} + \mathbf{R}) = \lambda_{\mathbf{R}}\mathbf{H}(\mathbf{r}) \quad (2.5)$$

In order for states to remain physically equivalent, it is clear the eigenvalue $= \lambda_{\mathbf{R}}$ is restricted to lie on the complex unit circle. Thus,

$$T_{\mathbf{R}}\mathbf{H}(\mathbf{r} + \mathbf{R}) = e^{i\mathbf{k}\cdot\mathbf{R}}\mathbf{H}(\mathbf{r}) \quad (2.6)$$

where \mathbf{k} is an arbitrary parameter yielding the proper translation eigenvalue that so far has absolutely no relationship with the lattice periodicity.

In general, the translation operator cannot distinguish between states with the same eigenvalue. The best that can be done is express the magnetic field as a superposition of all possible states which would have the same eigenvalue

$$\mathbf{H}(\mathbf{r}) = \sum_{\mathbf{G}} \mathbf{h}_{\mathbf{G},\mathbf{k}} e^{i(\mathbf{k}+\mathbf{G})\cdot\mathbf{r}} \quad (2.7)$$

Here, $\mathbf{h}_{\mathbf{G},\mathbf{k}}$ are Fourier coefficients and the summation is over all possible reciprocal lattice vectors \mathbf{G} . Essentially, the reciprocal lattice vectors \mathbf{G} are able to exactly nullify lattice translations and leave the eigenvalue unchanged and may be defined as such. Bringing the exponential outside of the summation we get

$$\mathbf{H}(\mathbf{r}) = e^{i\mathbf{k}\cdot\mathbf{r}} \sum_{\mathbf{G}} \mathbf{h}_{\mathbf{G},\mathbf{k}} e^{i\mathbf{G}\cdot\mathbf{r}} \quad (2.8)$$

where the summation becomes a simple Fourier series which may be equivalently expressed as a periodic function $\mathbf{u}_{\mathbf{k}}$ with the same periodicity as the real dielectric lattice

$$\mathbf{H}(\mathbf{r}) = e^{i\mathbf{k}\cdot\mathbf{r}}\mathbf{u}_{\mathbf{k}}(\mathbf{r}) \quad (2.9)$$

This is the Bloch theorem. It represents the most general expression of the magnetic field inside a photonic crystal with a well defined translation eigenvalue. The Bloch-wave is simply a plane-wave modulated by an envelope function with the same periodicity as the crystal lattice.

Once again, \mathbf{k} has nothing directly to do with the crystal periodicity, it simply describes how the complex phase of the propagating Bloch-wave changes per lattice unit. Since \mathbf{k} describes spatial translations, it is the *de facto* propagation constant. However, the Bloch theorem implies that \mathbf{k} can only represent physically distinct states over a finite range values associated with the complex unit circle. Thus, the \mathbf{k} -space repeats itself after a reciprocal lattice vector, a phenomena frequently referred to as known as zone-folding. Consequently, analysis is usually restricted to a non-redundant Voronoi-like section of the reciprocal lattice space often referred to as the Brillouin zone [77]. The procedure is summarized in Fig. 2.4.

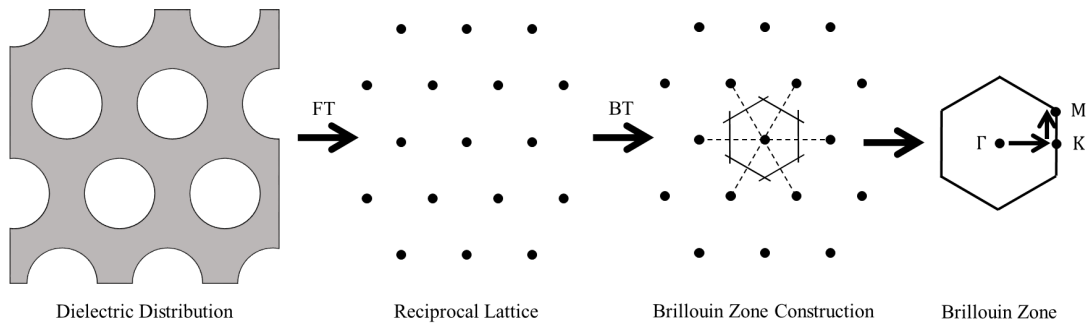


Figure 2.4: Also known as Bragg's law, the reciprocal lattice yields the selection rules for possible scattering events inside a PC. The Fourier transform (FT) of the periodic dielectric arrangement yields the reciprocal lattice. Applying the Bloch theorem (BT) restricts analysis to a Voronoi-like region in \mathbf{k} -space. Here Γ MK represent points of high symmetry [77].

In the case of photonic crystal slabs, the dispersion diagrams are represented with the 2D \mathbf{k} -space "rolled" out using a Γ MK notation in order to depict the directional dependence of propagation constant in a 1D representation, as shown in Fig. 2.5. However, strictly speaking, the system is not 2D, and a light line must be used to distinguish guided modes from radiative modes as was the case with the dielectric slab. As before, a discrete set of modes emerge inside the light line due to the TIR confinement. The mode shape, which is fully described by the periodic term $\mathbf{u}_{\mathbf{k}}(\mathbf{r})$ in equation 2.9, may be further classified using other possible symmetries including discrete rotational and mirror symmetry. For this reason, it is not necessary to show the dispersion for the full Brillouin zone, only the smallest, non-redundant path. Symmetry and linearity may be used to compute the dispersion at any \mathbf{k} inside the Brillouin zone not necessarily traversed along the selected \mathbf{k} -path.

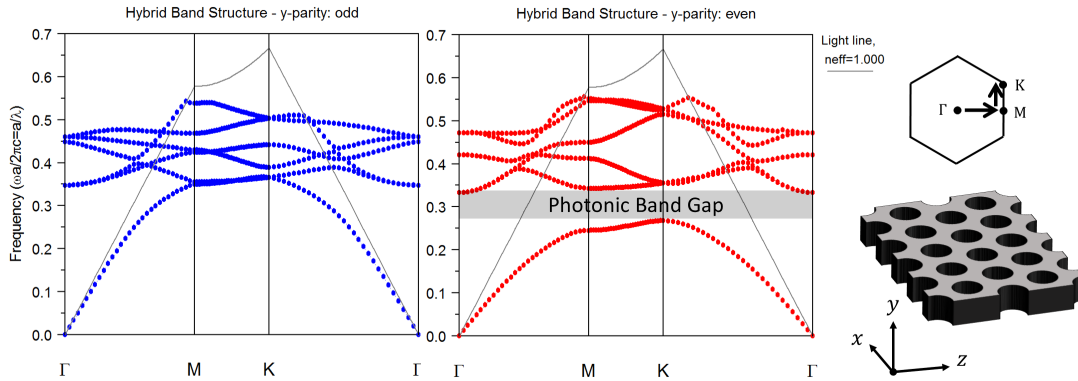


Figure 2.5: The dispersion diagram of a photonic crystal slab of silicon. Note the \mathbf{k} -space correspondence to a path of sequential points high symmetry. The distortion of the light line is a direct result of the particular path taken to high symmetry points. A photonic band gap is formed for even parity of the \mathbf{E} in the y -direction which corresponds to transverse electric (TE) modes.

At high symmetry points, represented by Γ , M , or K , the Bloch-wave becomes exactly 180 degrees out of phase after each lattice translation and forms a standing wave. At these turning points, the slope of the dispersion curves must go to zero due to zone-folding. Two types of mode profiles exist depending on where the field is concentrated as shown in Fig. 2.6. The energy contained in both distributions is related to the light frequency and is a function of the relative permittivity $\epsilon_r(\mathbf{r})$. If the dielectric contrast is high enough, an energy gap is formed³. Real eigenvalue solutions of Θ might not exist for light across this frequency band associated with the energy gap, regardless of the direction \mathbf{k} points. Therefore, the propagation of light is forbidden in *all* directions. This is the origin of the photonic band gap (PBG).

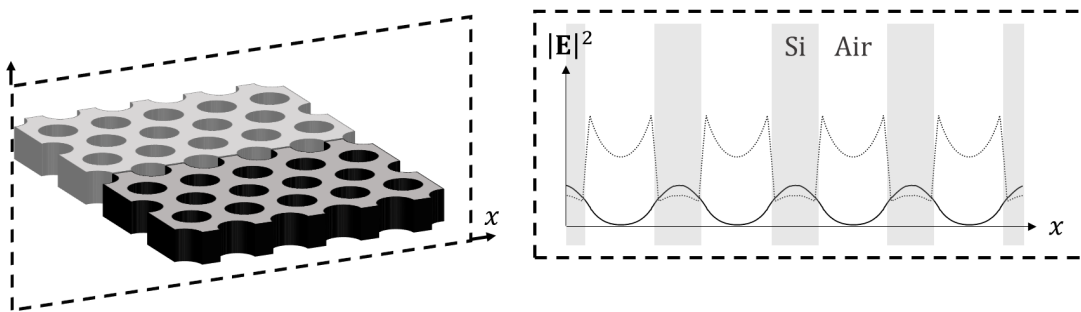


Figure 2.6: At the "K" symmetry point, two possible field intensity profiles exist where the field is concentrated in either the air holes or the slab. A higher frequency is required to generate the same wavelength inside air than inside the slab.

Before discussing line defects, yet another important way of classifying modes is according

³Energy in terms of the Rayleigh quotient formed by Θ which is a normalized form of the physical energy

to mirror symmetry. If mirror symmetry exists in the dielectric media across some plane, a parity operator \mathbf{M}_i may be constructed. If \mathbf{M}_i commutes with the translation operator, the eigenvalues may be well defined simultaneously. This is true only if the normal-vector of the mirror-plane has no \mathbf{k} components. As mentioned earlier, large PBGs occur for transverse electric-like (TE) polarization in PC slabs (\mathbf{E} in-plane at mid-slab). Since the slab possesses mirror symmetry about the mid-slab plane, a mirror operator \mathbf{M}_i may be constructed that acts on the field⁴ to yield its eigenvalue λ_i . Here, we select the i th-direction to be the mirror plane normal.

$$\mathbf{M}_i \mathbf{E}_i(x_i) = \lambda_i \cdot \mathbf{E}_i(-x_i) \quad (2.10)$$

We may find the eigenvalues of \mathbf{M}_i using the simple observation that two mirror translations give the identity

$$\mathbf{M}_i^2 \mathbf{E}_i(x_i) = \lambda_i^2 \cdot \mathbf{E}_i(x_i) \quad (2.11)$$

Evidently, modes in a system that possesses mirror symmetry may be classified as either even $\lambda_+ = +1$ or odd $\lambda_- = -1$ which act on the individual components of \mathbf{E} . Thus, we may define the transformation rules outlined in Table 2.1. The dispersion diagrams for both in-plane parities is shown in Fig. 2.5. A PBG clearly, exists for even symmetry which corresponds to the \mathbf{E} lying in-plane at mid-slab. Mirror symmetry will become important later for classifying the defect modes of the PC directional coupler and estimating the coupling-length.

Table 2.1: Table of Parity Relationships [80]

Operator	λ	\mathbf{E}_x	\mathbf{E}_y	\mathbf{E}_z
\mathbf{M}_x	+1	-1	+1	+1
\mathbf{M}_x	-1	+1	-1	-1
\mathbf{M}_y	+1	+1	-1	+1
\mathbf{M}_y	-1	-1	+1	-1
\mathbf{M}_z	+1	+1	+1	-1
\mathbf{M}_z	-1	-1	-1	+1

2.4 Photonic Crystal Slab Line Defects

A segue into describing the operation of the PCDC are line defects which have been well established over the past fifteen years [81]. Using both TIR and the PBG, a waveguide may be

⁴Here, the \mathbf{E} field is used rather than the \mathbf{H} field for illustrative purposes. In actuality, \mathbf{H} is a *pseudo-vector* and transforms a differently under reflection symmetry

constructed in the PC slab by filling a row of holes as shown in Fig. 2.7. The line defect alters the symmetric properties of the bulk lattice and the dielectric structure is no longer described simply by a pair of triangular primitive lattice vectors. While the dielectric periodicity is broken in the z -direction, it is still periodic in the x -direction, the direction of propagation, and the Bloch theorem will still apply here.

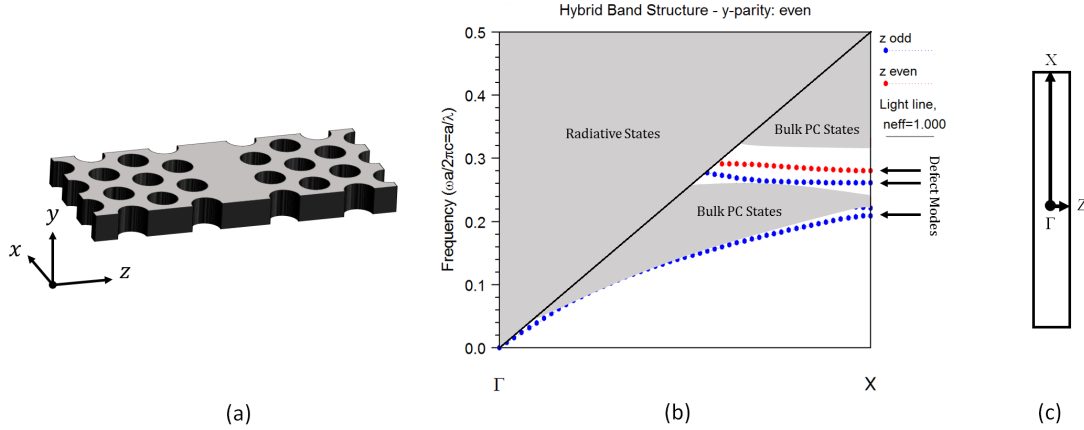


Figure 2.7: The band structure for a line defect (a) is shown in (b). Both TIR and the PBG create defect modes as indicated in the figure. The repetitive structure of the crystal lattice is only maintained in the x -direction and the defect needs to be padded with an infinite number of lattice periods. This changes the Brillouin zone from a hexagon to a narrow rectangle as shown in (c). Any modes with a non-zero k_z component are bulk PC modes that are smeared out when projected along the x -direction of the \mathbf{k} -path.

Since we are only interested in modes propagating along the line defect, the band structure is projected along this axis as shown in Fig. 2.7. Light which is localized to the defect must satisfy the Bragg condition which preserves the discrete nature of the defect after projection. However, modes which lie outside the PBG are able to propagate freely inside the crystal. These extended modes are therefore described by any \mathbf{k} -point lying inside the Brillouin zone of the bulk band structure. Projecting these modes creates a continuum of extended states across where the perpendicular \mathbf{k} is non-zero.

An important property of the PC defect mode is flattening of the dispersion near the zone edge X due to zone-folding. Here, the group velocity, given by

$$v_g = \frac{d\omega}{dk} \quad (2.12)$$

goes to zero. Generally, dispersion with high curvature is undesirable causing the strong distortion in light pulses and standing waves where $v_g = 0$. Fortunately, there exists an extended region of linear dispersion. At a glance, the group velocity appears to be negative and the PC dispersion would be anomalous. However, the phase velocity is ill-defined as the eigenmode is made of an infinite number of $\mathbf{k} + \mathbf{G}$ Fourier components, each with its own phase velocity.

It can be shown that the Bloch wave is made primarily of negative \mathbf{k} wave vectors which align with v_g [82]. Therefore, propagating defect modes in this case are in fact non-anomalous.

When the ends of two different waveguides are brought together, the amount of power transfer depends on the coupling efficiency much like the impedance of matching electrical networks. The coupling efficiency is expressed as the mode-matching condition represented by normalized inner product of the mode profiles at the same frequency.

$$\eta = \frac{|\int \mathbf{E}_1^* \cdot \mathbf{E}_2 dA|^2}{\int |\mathbf{E}_1|^2 dA \int |\mathbf{E}_2|^2 dA} \quad (2.13)$$

It is clear that coupling to odd defect modes is impossible using a Gaussian beam [83].

2.5 Optical Directional Coupler

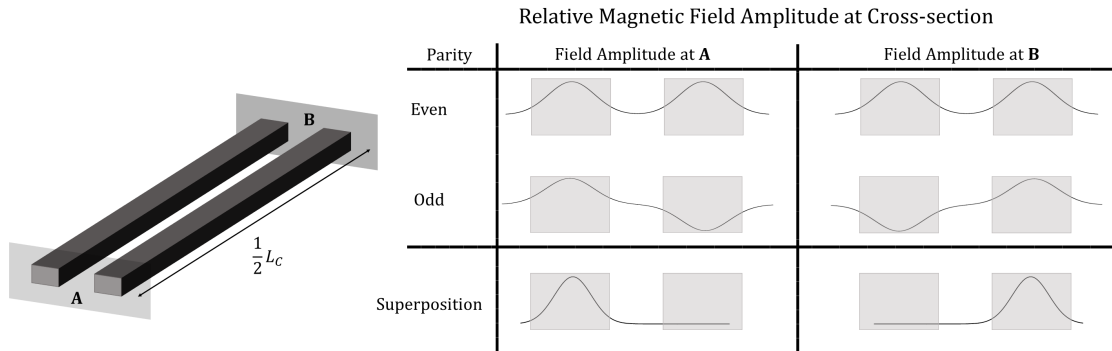


Figure 2.8: By mirror symmetry, an even and odd mode must exist for a symmetric waveguide with the field distribution described in the figure. Light initially launched at **A** can be expressed as a superposition of even and odd modes. Since these modes generally travel at different speeds, the relative phases between the even and odd superposition will gradually change until the power is effectively exchanged to the opposite waveguide at **B**

A directional coupler is created wherever two waveguides are brought near to each other. Depending on whether the two waveguides are the same or different, the coupler may be classified as either symmetric or asymmetric, respectively. Here, we consider only symmetric couplers as shown in Fig. 2.8 where power may be completely exchanged between the two closely spaced waveguides. As two waveguides are brought together, the dispersion bands split into two degenerate modes.

By mirror symmetry, the dual waveguide system should support both an even and odd mode with propagation constants k_e and k_o , respectively. Thus, an initial excitation of a single waveguide, may be thought as a linear combination of the even and odd modes. Since the even and odd propagation constants k_e , k_o are different, the even and odd modes travel at

different speeds and the superposition of these modes will appear as a periodic exchange of power between the two waveguides. The distance required to complete a full cycle is the coupling-length L_c and may be computed in terms of the difference between the propagation constants [84].

$$L_c = \frac{2\pi}{(k_e - k_o)} \quad (2.14)$$

2.6 Operating Principle of Coupler Based Optomechanical Sensor

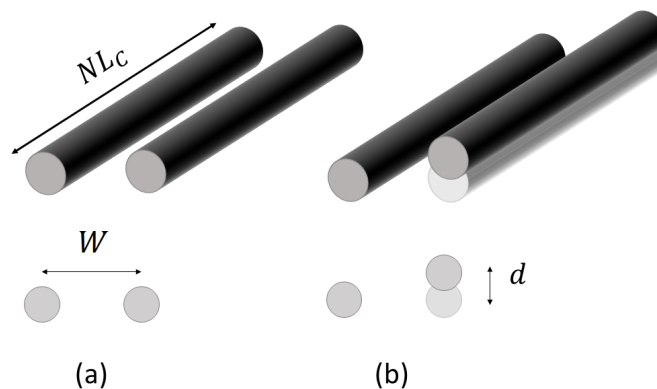


Figure 2.9: (a) Two waveguides initially separated by W form a directional coupler of length NL_c . (b) A simple model may be constructed describing the transmission change due to out-of-plane deflections d assuming negligible cross section in each waveguide and exponential decay of the EM fields.

If the coupling length is expressed in terms of the difference between even and odd propagation constants (i.e. $\kappa = k_e - k_o$), then the intensity of light at any given point along x the waveguides is given without approximation by

$$T_{thru} = \cos^2\left(\frac{\kappa x}{2}\right) \quad (2.15)$$

$$T_{coup} = \sin^2\left(\frac{\kappa x}{2}\right) \quad (2.16)$$

Thus, for a fixed sensor length $x = L_{MEM}$, the variations of intensity can only depend on $\kappa(w, d)$ which is implicitly a function of separation where w is the in-plane separation and d is the out-of-plane deflection, as shown in Fig. 2.9.

While a closed form of $\kappa(w, d)$ cannot be found analytically, some insight is gained by considering the separation of a coupler made of two narrow waveguides of negligible cross-section. The physical origin of coupling may be understood in terms of the mode-matching

between the guided mode of one waveguide with the evanescent field of the other, that extends across the separation [84]. The electromagnetic continuity equations applied to guided modes at the index boundary predict an exponentially decaying evanescent wave. If the field inside the waveguide is assumed to be uniform, κ must therefore be exponentially related to the waveguide separation s .

$$\kappa \propto \lim_{s \rightarrow \infty} e^{-\gamma' s} \quad (2.17)$$

where γ' is some positive constant which determines how strongly the EM fields are confined to the waveguides. The behaviour of κ can be determined heuristically by ignoring the cross-section of each waveguide. By fixing $w = W$, κ may be re-expressed as

$$\kappa \propto e^{-\gamma \sqrt{1 + \left(\frac{d}{W}\right)^2}} \quad (2.18)$$

where $\gamma'W = \gamma$. Now define the κ in the relaxed state to be $\kappa_0 = \kappa(d = 0)$

$$\kappa_0 = C e^{-\gamma} \quad (2.19)$$

where C is a multiplicative constant which may be solved.

$$C = \kappa_0 e^{\gamma} \quad (2.20)$$

Thus, κ at an arbitrary deflection d can be expressed in terms of the relaxed κ_0 .

$$\kappa = \kappa_0 e^{\gamma \left(1 - \sqrt{1 + \left(\frac{d}{W}\right)^2}\right)} \quad (2.21)$$

Suppose the length of the coupler is fixed at $x = L_{MEM}$ and expressed as N units of the relaxed coupling-length $L_{MEM} = L_c N$ where $L_c = 2\pi/\kappa_0$. The intensity as seen at the coupler outputs can be expressed as

$$T_{thru} = \cos^2 \left(\frac{\pi N \kappa}{\kappa_0} \right) \quad (2.22)$$

$$T_{coup} = \sin^2 \left(\frac{\pi N \kappa}{\kappa_0} \right) \quad (2.23)$$

which can be finally expressed in terms of the deflection d .

$$T_{thru} = \cos^2 \left(\frac{\pi N}{e^{\gamma \left(\sqrt{1 + \left(\frac{d}{W}\right)^2} - 1\right)}} \right) \quad (2.24)$$

$$T_{coup} = \sin^2 \left(\frac{\pi N}{e^{\gamma \left(\sqrt{1 + \left(\frac{d}{W}\right)^2} - 1\right)}} \right) \quad (2.25)$$

The output intensity of only the coupled output port is plotted with respect to normalized deflections with $N=1/4$, $1/2$, and 1 in Fig. 2.10 which are referred to quarter-, half-, and full-bridge designs in this thesis, respectively.

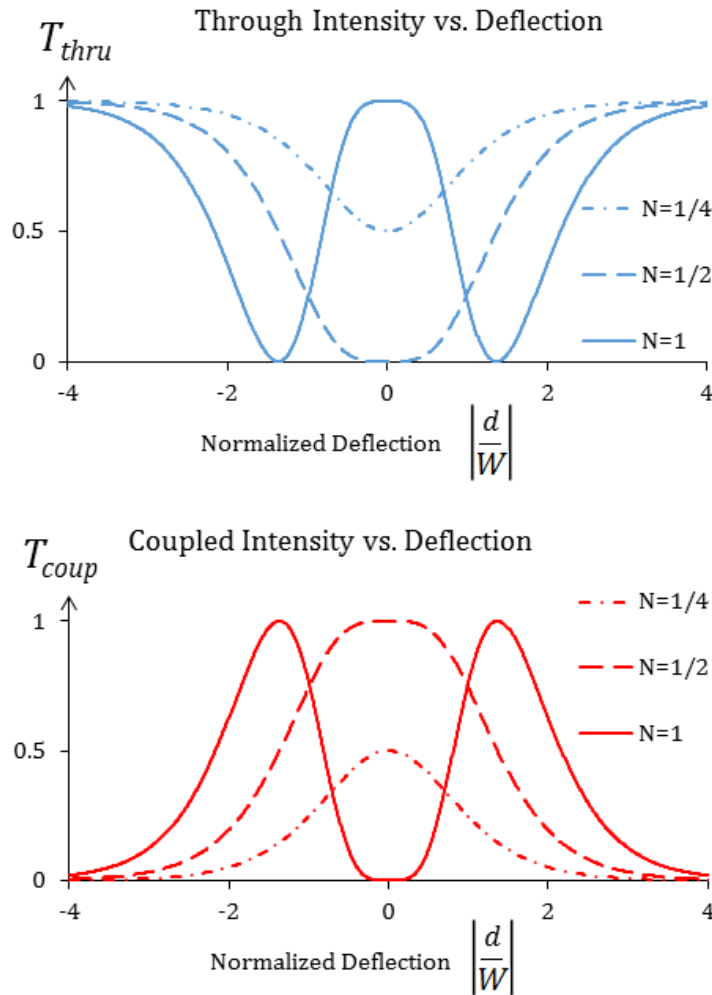


Figure 2.10: The expected optical response as seen at both output ports for $N = 1/4, 1/2$, and 1 as a function of out-of-plane deflection.

While being quite crude, this simple model illustrates a few key points. The sensitivity in terms of transmission change per nanometer may be increased by shrinking the separation between the waveguides. Since the deflection is scaled with respect to the separation in Fig. 2.10, adjustments in waveguide separation will have little effect on the dynamic range of the PCDC sensor. Therefore, the separation provides a means of tuning the resolution of the PCDC.

The effect of changing the length spanned by the sensor is observed to change the shape of the intensity response curve. For example, at $N = 1$ the coupler is a full coupling-length in its resting position. Subsequent deflections cause the system to transition from the full-coupler

to a half-coupler and finally to an isolated waveguide. The transmission in this case does not follow a one-to-one relationship with deflection which is true for all designs with $N > 1/2$. In general, the length of the sensor provides a means adjusting the linearity and dynamic range.

Realistically, the γ coefficient could be different in each w or d direction. Also, κ is likely to vary from the exponential relationship due to cross-sectional features that scale-in at close distances. However, there is very little more to be gained by predicting these effects analytically. In general, what can be said is the ideal PCDC sensor with good linearity, dynamic range, and sensitivity should utilize modes with enhanced evanescent fields have minimized separation.

2.7 Conclusion

This concludes the conceptual understanding of the optical directional coupler based displacement sensor. It has been shown that strongly dispersive waveguides may be formed using a filled-hole line defect which confines light using the photonic band gap. There is a strong theoretical basis that a directional coupler can exist for an appropriately designed symmetrical line defect. Waveguide deflections may be measured by observing the coupler output intensity. In the next chapter, we investigate the case of a split line defect in the PC lattice which acts as a directional coupler and how it might be used as an optomechanical sensor.

Chapter 3

Design and Simulation

The primary design target of the PCDC sensor is to achieve the 200kPa range as described in the microfluidic reference [24] with the intention of making it suitable for typical microfluidic applications. This is relatively easy to achieve with non-buckled structures by adjusting the strut length and membrane width after the optical design parameters have been fixed.

The optical design process begins by establishing the bulk PC slab parameters. In order for the PCDC to guide light, the desired C-band wavelengths (1530–1565nm) must necessarily lie within the PBG of the bulk PC slab. PWE method is used to compute the band structure and determine the lattice pitch Λ and hole diameter D of the bulk PC slab. Next, a symmetric defect is introduced comprised of extended edge regions of width E separated by an air gap W representing the coupled waveguide system. PWE is later validated by FDTD simulation which is better suited for finite structures and modeling intrinsic material loss. Using FDTD, the transmission characteristics of the full-, half-, and quarter-bridge structures under deflection are investigated.

Finite Element Analysis (FEA) is used to model the mechanical stiffness under uniform loading in order to estimate the sensitivity. The mechanical resonance is also computed to in order to approximate the sensor response time. Additionally, the membrane strut members are predicted to buckle due compressive SOI stress built up during wafer fabrication. Arrayed-microbeam designs are modeled and allow relaxation of SOI stress with little effect on out-of-plane stiffness.

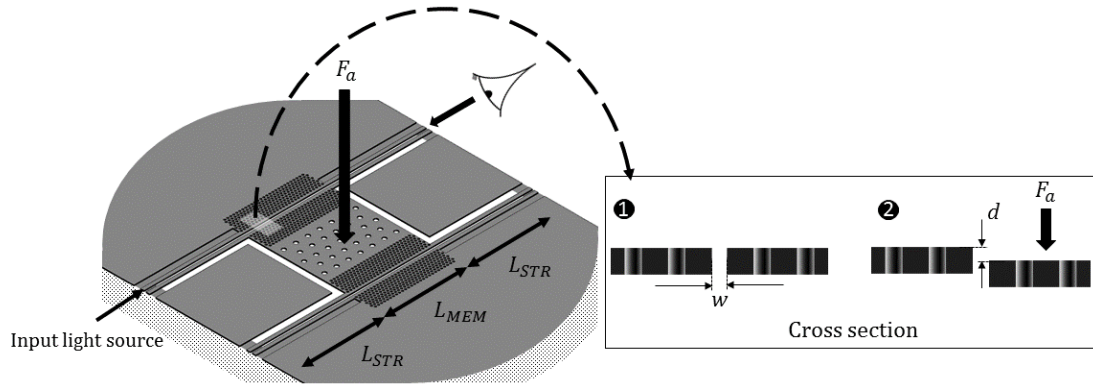


Figure 3.1: The PCDC design concept showing the released photonic crystal membrane. Light enters the photonic crystal split-line defect and couples to the adjacent side. Deflections in the PC membrane alter the observed transmission.

3.1 Design Overview

3.2 Optical Design

3.2.1 Fabrication Constraints

The PCDC sensor is most easily fabricated on buried oxide SOI wafers where subsequent under-etching of the oxide layer releases the top silicon film. The PCDC sensor is intended to operate across the C-band, specifically near 1550nm, where minimal attenuation in silica based fiber-optics exists. A portion of the fabrication of first generation sensors had the top-silicon machining out-sourced to IMEC ePIX-fab foundry using CMOS-based silicon photonics process technology. Although the fabrication process is discussed in more detail in chapter 4, it is introduced here as the product development kit (PDK) ultimately determined some of the design parameters.

3.2.2 SOI Substrate and Etch Depths

The SOI substrates used in the process flow have a top silicon layer thickness of $T = 220\text{nm}$ with a $2\mu\text{m}$ buried oxide layer (SiO_2) on an extended Si substrate as shown in Fig. 3.2. The fabrication process offers a full-depth etch in addition to two partial depths at 70nm and 150nm. By guiding light to the PCDC using rib waveguides, the buried oxide is not exposed and waveguide integrity may be maintained during wet etching. Moreover, the additional etch depths allow high efficiency surface grating couplers (SGCs) to be created that provide optical interfacing with the chip.

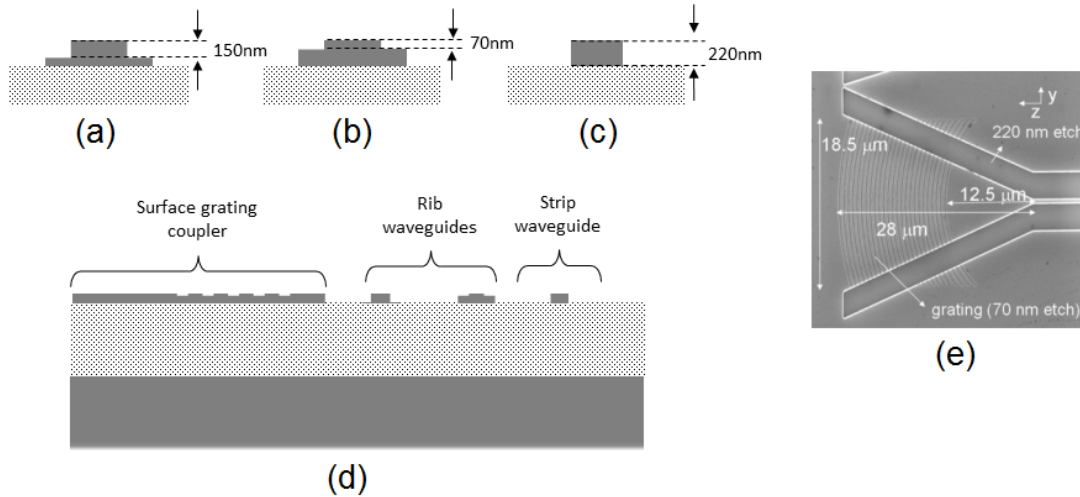


Figure 3.2: Cross section of SOI wafer. Three different etch depths are offered using the IMEC process which can be used to create rib (a&b) and channel waveguides(c). (d) Overall, the SOI wafer has a top layer silicon layer of 220nm followed 2000nm of silicon dioxide followed by 2mm of silicon. (e) Scanning electron microscope image of a triple-etch depth surface grating coupler.

3.2.3 Surface Grating Coupler Ports

The SGCs provide a way of interfacing and measuring a large array of PCDC sensors. Etched slots in the top silicon layer work as an array of scattering centres physically separated by a 180 degree phase of the projected k -vector. Light which does not satisfy the constructive interference condition either leaks into the BOX layer or is reflected back. The key advantage of SGCs over other interfaces is its planar construction can easily be machined on the surface of the SOI wafer. This allows for rapid prototyping and efficient use of design space.

Optimized transverse electric (TE) SGC designs are part of a cell library incorporated in the PDK designed to operate at 1550nm. The transmission specifications of the coupler port include a -1.6 dB coupling efficiency across 80nm 3dB bandwidth [85]. The central wavelength of the coupler can be adjusted somewhat by changing the Bragg condition. This can be done by tuning the angle the optical fiber angle makes with the SOI plane during measurement. The optical fiber is usually tilted about 10 degrees in order to minimize 2nd order Bragg diffraction that occurs at zero degree normal [85].

3.2.4 Bulk PC Design Using Plane Wave Expansion

In a plane wave expansion scheme (PWE), the crystal periodicity is exploited to provide accurate estimation of PBGs. For \mathbf{E} in-plane at mid-slab, PBGs are known to occur in thin slabs with holes arranged in a triangular crystal lattice provided a large enough refractive index contrast exists [77]. Silicon is well suited due to its high refractive index ($n_{Si}=3.46$), IR transparency,

availability as SOI, and established surface etching technology.

Using the software RSoft, the photonic band structure is surveyed for variety of pitches and hole diameters to see if the desired 1550nm wavelength lies inside the PBG. The white regions in Fig. 3.3 indicate the conditions where the 1550nm wavelength lies inside the PBG, for a slab thickness of $T = 220\text{nm}$. Additionally, the design rule checker (DRC) of the IMEC product development kit limits the resolution of structures to around 130nm. Designs which do not fulfill the DRC are indicated by the hatched region.

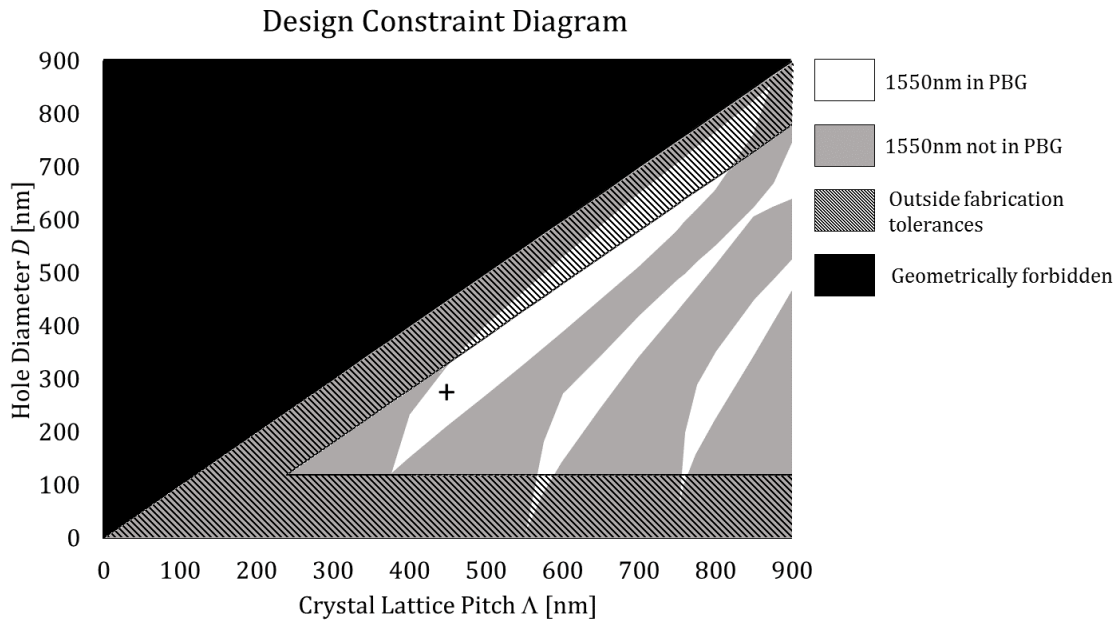


Figure 3.3: For a $T = 220\text{nm}$, the key design constraints that dictate the bulk PC parameters Λ and D are shown which include the presence of the desired wavelength in the PBG and the 120nm resolution of the design rule checker. The cross-hair represents the selected design parameters $\Lambda = 450\text{nm}$ and $D = 270\text{nm}$.

A pitch of 450nm and diameter of 270nm is selected to yield the largest possible range of diameters with the lowest pitch. Although higher order PBGs do occur at larger lattice pitches, the Brillouin zone becomes contracted and shrinks the band gap. The higher order PBGs also occur at higher normalized frequencies where the band structure becomes constricted by the light line and effectively limits the functional bandwidth.

While the e-beam process used to create the UV lithographic mask is known to create stable pitches, the PC hole diameters can depend on many factors. It is prudent to allow for the largest possible range of diameters as additional designs may be included in a fabrication-run in order to offset potential biasing of the feature sizes. The band structure featuring the selected parameter values is shown in Fig. 3.4.

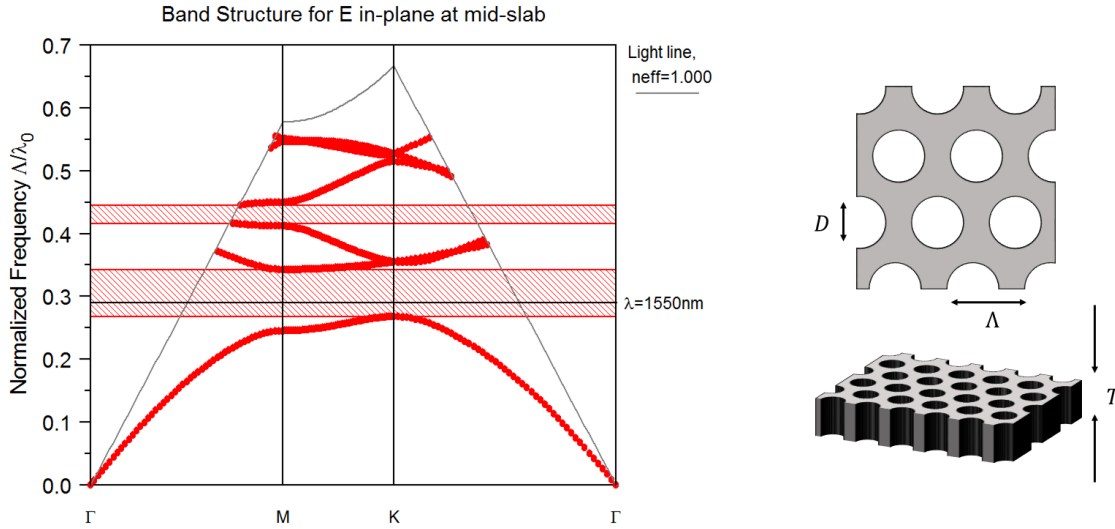


Figure 3.4: Band structure for **E** in-plane at mid-slab inside the bulk silicon photonic crystal structure surrounded by air. The desired 1550nm wavelength is observed to lie within the photonic band gap which extends from 1313nm to 1681nm. PC dimensions: thickness 220nm, pitch 450nm, and hole diameter 270nm.

3.2.5 PCDC Defect Design Using PWE

In order to form the directional coupler, a symmetrical line defect is introduced as shown in Fig. 3.5. The computational domain changes from hexagonal to rectangular and additional PC lattice periods must be padded to the PWE domain along the direction where the translational symmetry is broken in order to effectively model the PCDC. Since the computational domain is repeated in all directions, only the full PCDC can be simulated using PWE and not just an isolated half.

To overcome this, we consider the case where $W \rightarrow \infty$ and the waveguides are far apart in isolation. Here, the coupling-length becomes infinite and the dispersion curves of the even and odd defect modes should rapidly approach one another. Thus, the band structure for isolated waveguides should depend only on the edge width E , not the air gap separation when W is large. By using a sufficiently large separation, PWE can be used to tune the PC edge width while still modelling the full PCDC.

The bandwidth of the isolated waveguide, as shown in Fig. 3.6, is observed as E is parameterized. For $E < 0.3\Lambda$, the edge-waveguide is formed by terminating the bulk crystal by a plane which cuts through PC holes while the $E > 0.3\Lambda$ regime represents an extended edge without holes. Increasing the spatial dimension E shifts the defect dispersion curve down, therefore lowering the operating frequency and providing a means of tuning the split line defect. A suitable E may be found which aligns the linear region of the dispersion with the desired 1550nm wavelength.

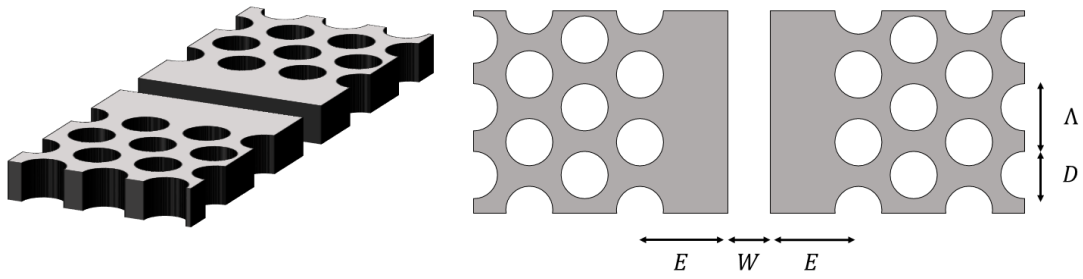


Figure 3.5: Symmetric line defect representing the directional coupler

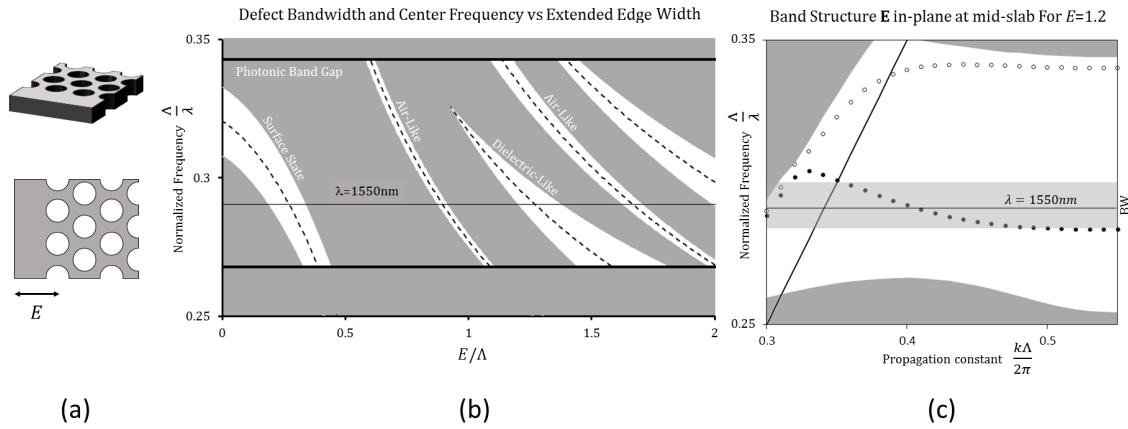


Figure 3.6: The isolated defect is shown in (a). The bandwidth of the defect modes is plotted as a function of E in (b). A slice of this parameterization is projected in (c) which shows the defect band structure for $E = 1.2\Lambda$. Here, the desired wavelength crosses a dielectric mode (black dots), indicated by negative slope. A surface mode (open circles) may be seen near the top of the PBG indicated by positive slope.

As the waveguides approach one another, the dispersion curves will split into even and odd modes. Since coupling can only exist across the frequency of intersecting bandwidths, the splitting effectively reduces overall bandwidth as shown in Fig. 3.7. The tapering of the bandwidth continues until some cut-off separation is reached and a common operating frequency between the even and odd modes no longer exists.

The splitting effect is more pronounced depending on where the EM field is concentrated. Each region in Fig. 3.6 describes modes with distinct electric field topology. For the surface modes, the field is concentrated to the outermost serrated edge of the PC. This enables the field to extend further into the air gap and enhances the coupling.

The splitting of the defect dispersion curves can be clearly observed in Fig. 3.8 for $E = 0.25\Lambda$ and $E = 1.2\Lambda$. A trade-off exists between bandwidth and κ as the same splitting effect tends to increase $\kappa = k_e - k_o$, or the difference between even and odd mode propagation constants. Therefore, the rate of tapering gives an indication of rate of change in κ which is

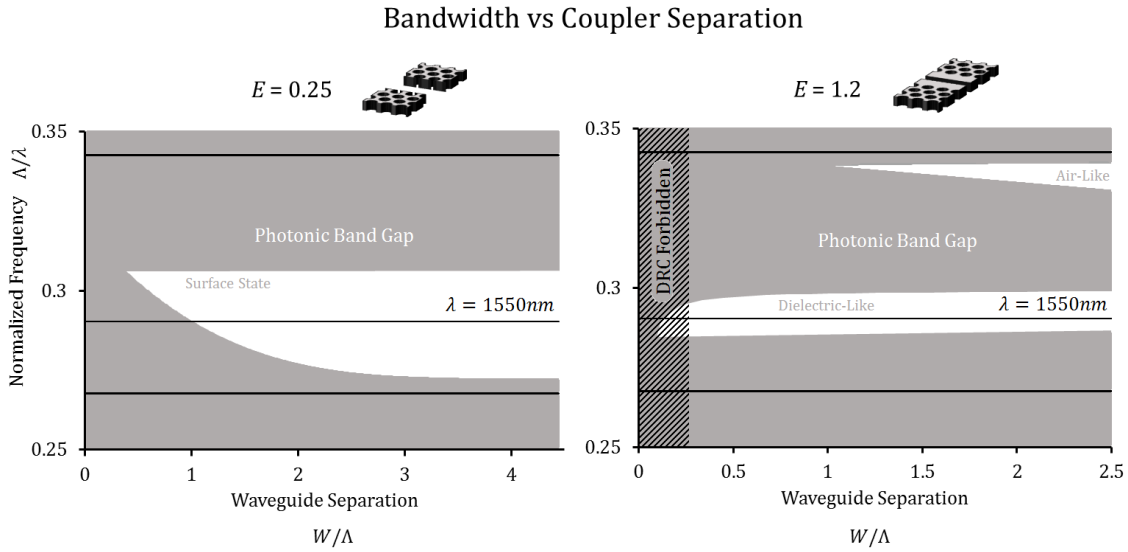


Figure 3.7: The bandwidth of two possible sensor configurations which use dielectric and surface modes which pass through the desired wavelength at $E = 0.25\Lambda$ and $E = 1.2\Lambda$ respectively.

exponentially proportional to the γ term discussed in chapter 2. The best dynamic range can likely be achieved with the surface mode where the slower bandwidth tapering suggests a lower γ .

Defect Band Structure for **E** in-plane at mid-slab

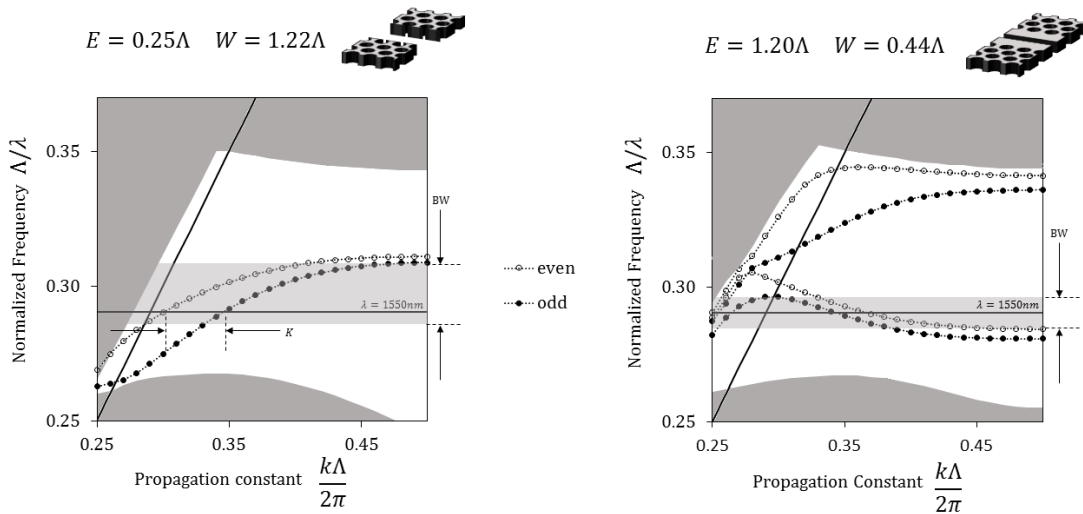


Figure 3.8: The defect band structure for PCDC designs of $(E = 0.25\Lambda, W = 1.22\Lambda)$ and $(E = 1.2\Lambda, W = 0.44\Lambda)$.

Although the surface mode possess larger bandwidth and dynamic range when compared to the dielectric mode, exciting such a mode is challenging as the field, strictly speaking, evanes-

cently decays both into the bulk PC and the surrounding air. Excitation of the surface mode is problematic and presents the same challenges facing the excitation of surface plasmon resonance. Thus, surface modes cannot be trivially excited using conventional rib or channel waveguides and require novel optimization of the surrounding geometry.

It is much more straight forward to excite the dielectric mode where the EM field is confined inside the volume of a dielectric extension. Although the enhanced confinement increases γ and lowers the dynamic range, there are benefits to using the dielectric mode. The non-linearity may be mitigated somewhat by designing stiffer sensors. The fabrication stability of E is improved from $\frac{\Delta\lambda}{\Delta E} = 1.86$ for the surface mode to $\frac{\Delta\lambda}{\Delta E} = 0.67$ for the dielectric mode. Additionally, greater sensitivities may be achieved as the bandwidth persists at close separations. For these reasons, the selected design is based on the defect parameters $E = 1.20\Lambda$ and $W = 0.44\Lambda$.

Before moving on to FDTD simulation, the coupling-length may be estimated using the PWE data. The L_c value may be computed using

$$L_c = \frac{\Lambda}{k'_e - k'_o} \quad (3.1)$$

where $k' = k\Lambda/2\pi$ is the normalized propagation constant as plotted for the $E = 1.2\Lambda$ and $W = 0.44\Lambda$ PCDC band structure. Here, the coupling length is observed to be 42Λ , or approximately $19\mu\text{m}$ at 1550nm .

3.2.6 FDTD Simulation

Using the software Lumerical, the FDTD model shown in Fig. 3.9 was constructed using a custom script which allowed easy adjustments of structure parameters and automated parameterization. The main code used in these scripts may be found in Appendix C. Half of the PCDC is fixed to the main substrate where the interfacing waveguides are protected by a partial etch of the silicon. The other half of the PCDC is connected to the substrate by the waveguides themselves, which form strut members and support the membrane after under-etching. Care must be taken to avoid simulating the slow-light regime, particularly near the even mode resonance where the group velocity approaches zero. EM energy from the FDTD pulse will dwell inside the domain near these frequencies and complicate the simulation.

An accurate estimation of the coupler-length L_c can be computed by examining the field distribution at the mid-slab of each of the coupled waveguides shown in Fig. 3.10. The rapid variations of the field magnitude are periodic with the PC pitch and is predicted by the Bloch theorem [77]. By filtering the field distribution, the complete exchange of power is estimated to occur after $21.8\mu\text{m}$ or 48Λ .

The coupling-length was computed for a variety of air gaps and is shown in Fig. 3.11. There is a direct correspondence with the PWE spectral characteristics with even mode resonance occurring at 1582nm . Here, the coupling-length shrinks rapidly to achieve its minimal value.

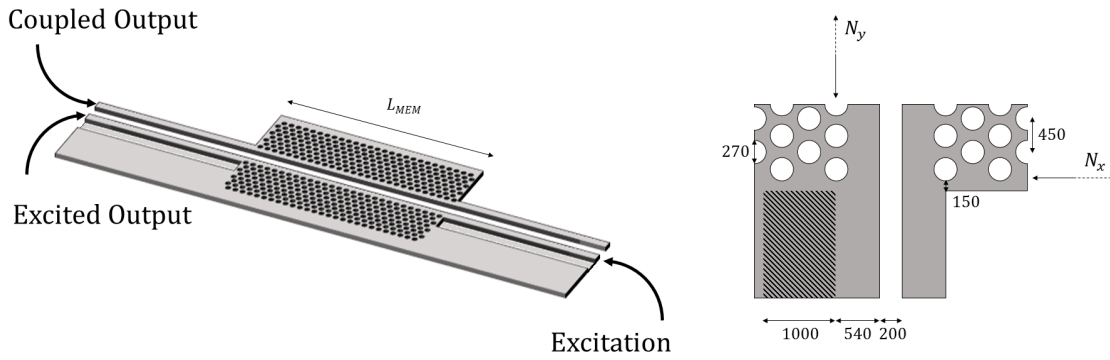


Figure 3.9: The PCDC FDTD domain is shown. A close up of the PC waveguide junction is depicted in units of nanometres. The hatched region is the 150nm partial etch depth of the rib waveguide. The FDTD domain was constructed using a parameterized script which may be found in Appendix C.

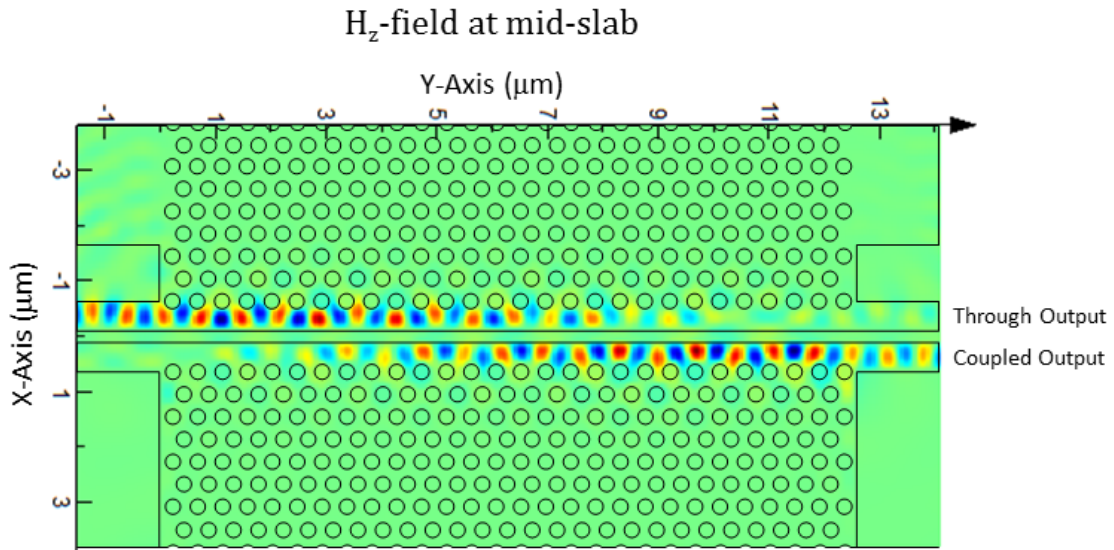


Figure 3.10: The out-of plane component of the magnetic field at mid-slab for $\lambda = 1550\text{nm}$ and $L_{MEM} = 12.47\mu\text{m}$ (28 PC holes) is simulated using FDTD. Light enters the upper port and propagates from left to right. Energy is clearly transferred from the excited port to the coupled output forming a half-bridge coupler. The outline of the PCDC structure is also shown.

Extremely sensitive sensors might be obtained operating in this regime; however, the rapid variation in coupling-length would effect the design stability.

The transmission characteristics of the half-bridge coupler ($L_{MEM} = \frac{1}{2}L_c$) consisting of 28 holes along its length is shown in Fig. 3.12 which corresponds to a L_{MEM} of $12.7\mu\text{m}$. The transmission is normalized with respect to the total power contained in the excitation source, which is a pre-computed fundamental TE modal solution for the ingoing rib waveguide. The rib-to-PC wavguide coupling loss can inferred to be approximately -1dB (33%) per junction

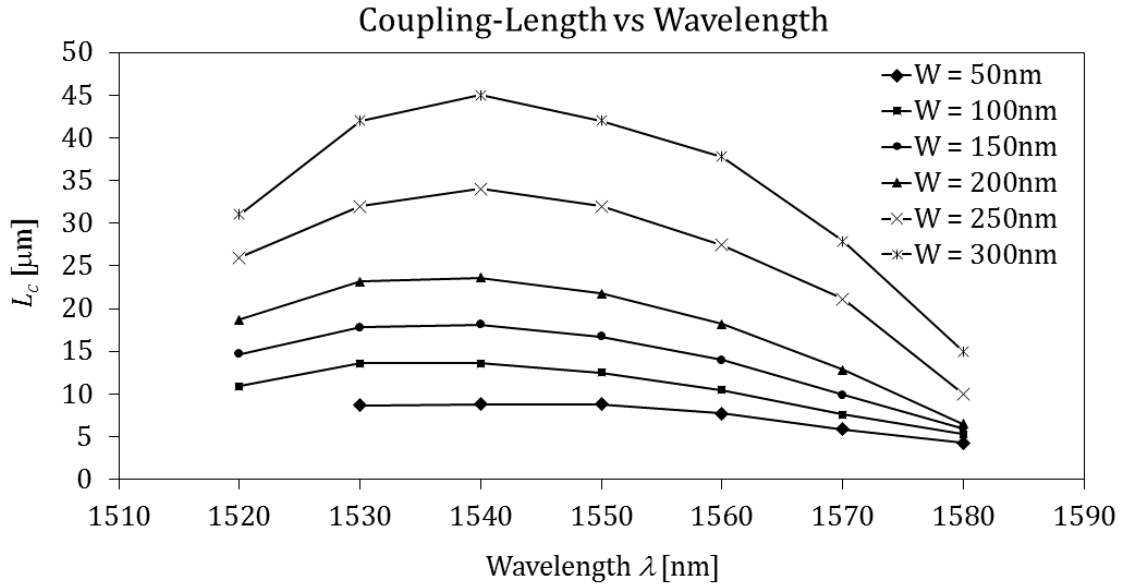


Figure 3.11: The relationship between L_c and wavelength as the air gap varies is shown.

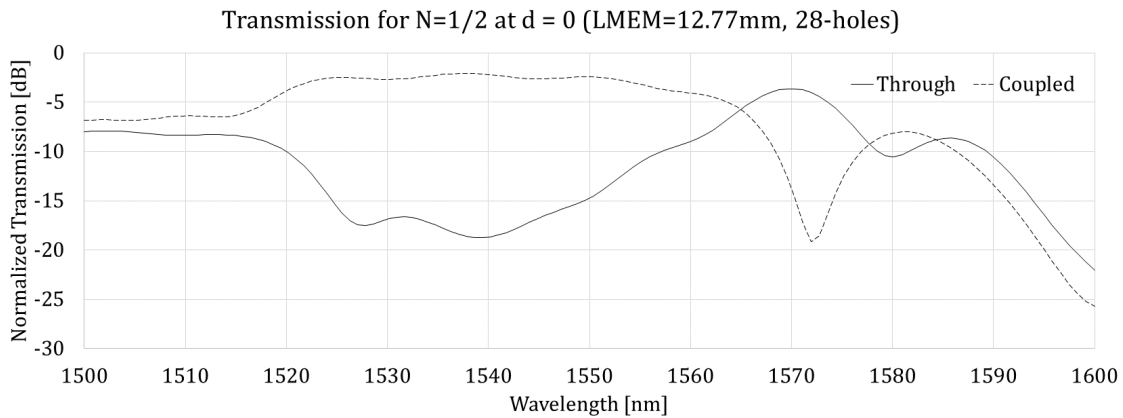


Figure 3.12: The transmission output spectra is shown for the $N = \frac{1}{2}$ bridge sensor.

across a 35nm bandwidth. This might be improved by 0.5dB using an optimized junction that cuts into a the first PC hole. However, this could compromise the mechanical integrity of the sensor and is avoided.

The change in transmission at both coupler outputs was simulated for out-of-plane deflections d and is depicted in Fig. 3.13. As expected, the total power transmitted to each output is conserved. For a coupler separation of 200nm, the average output transmission sensitivity S_{opt} lies in the range of 0.015–0.15% full scale (%FS) per nm depending on the sensor length (i.e. full-, half-, or quarter-bridge) and operating regime. The complete specifications of each sensor design can be found in Tables 3.1, 3.3, and 3.2.

The deflection of the membrane while in its resting state may not necessarily be zero.

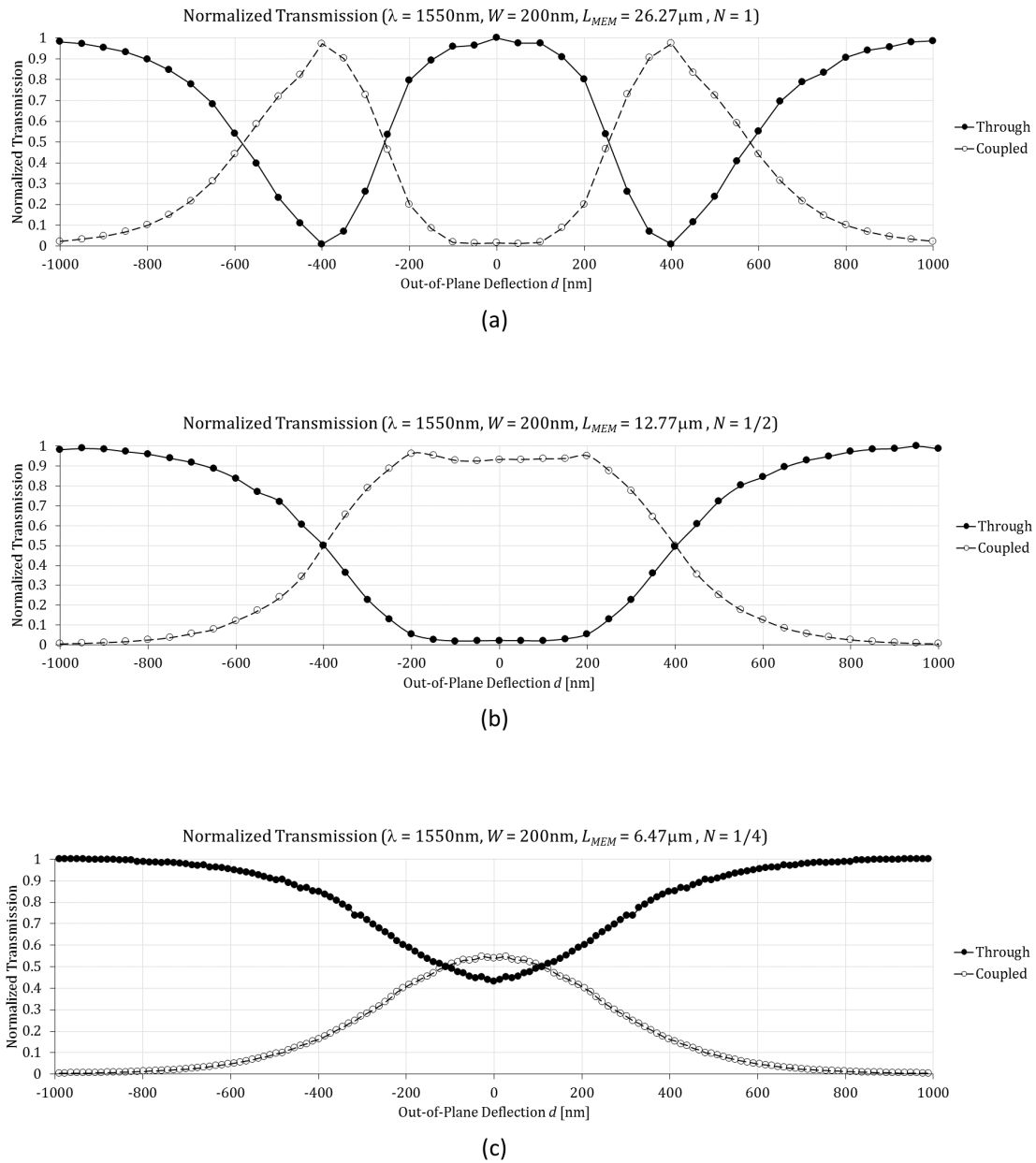


Figure 3.13: The normalized transmission characteristics for three different sensor lengths (a) $L_{MEM} = L_c$, (b) $L_{MEM} = L_c/2$, and (c) $L_{MEM} = L_c/4$ are plotted as a function of out-of-plane membrane deflection at 1550nm and air gap separation 200nm.

Buckling, due to the relaxation of residual SOI stress after under-etching, can break the out-of-plane symmetry and provide some initial displacement. It is important to consider these buckled designs. Due to the symmetry of the system, the sensitivity is guaranteed to go to zero if the membrane lies in-plane with the fixed PC waveguide. Buckling and other mechanical aspects related to the PC sensor are modeled in the next section.

3.3 Mechanical Design

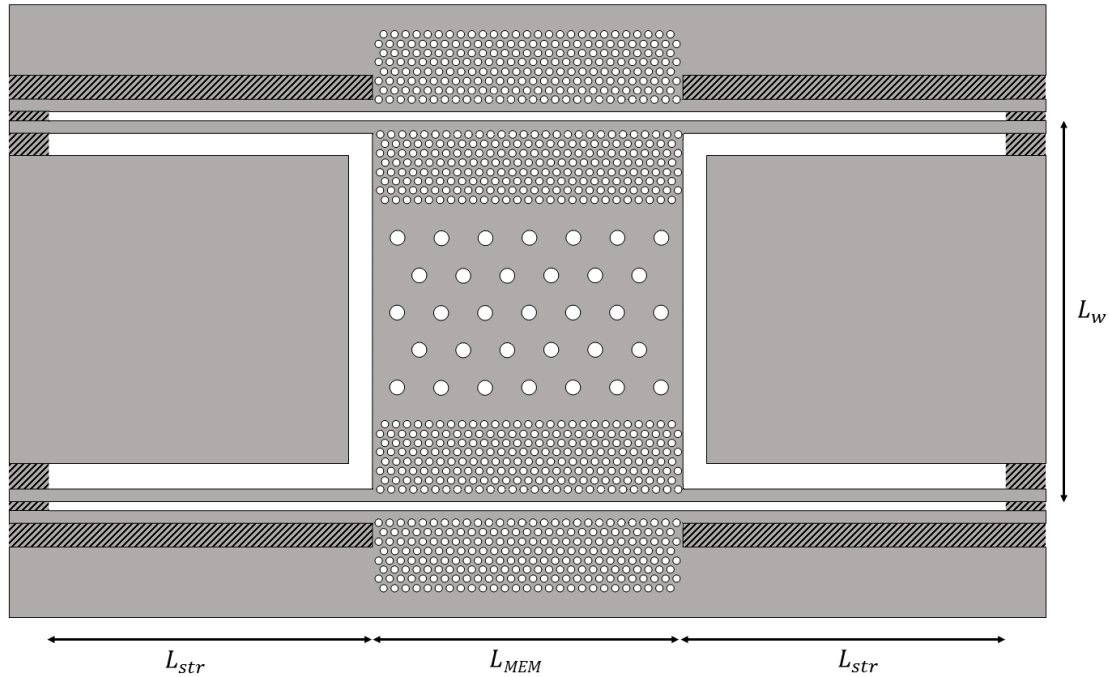


Figure 3.14: The basic design of the PCDC sensor. The top silicon layer, 150nm etch depth, and the etched BOX are indicated by the grey, hashed grey, and white regions, respectively. The sensor length is some multiple of the coupling length $L_{MEM} = NL_c$. The mechanical properties of the sensor is largely controlled by the strut length L_{str} .

The top view of the generic PCDC sensor is shown in Fig. 3.14. Mechanical properties of the PCDC sensor are primarily determined by the length of the strut members that support the membrane as shown in Fig. 3.15. In general, decreasing the length of the strut members will increase the resonant frequency and critical buckling load but with a trade-off in sensitivity in terms of applied force or pressure. Since the strut members also serve as interfacing waveguides, the width is fixed at E which optimizes the coupling.

While the mechanical properties of silicon is known to scale down to the MEMS regime, the relative uncertainty in physical dimensions and residual wafer stress become dominant factors when trying to evaluate the properties of nanopatterned thin films. The variability in Young's modulus of single-crystal silicon thin films has a 10% standard deviation about its theoretical value of 168.9GPa along (110) ranging from 135–219GPa [86]. The residual compressive stress in flip-bonded SOI wafers works against the tensile stress generated by membrane deflections and can effectively reduce both the in-plane and out-of-plane membrane stiffness.

The mechanical aspects such as the stiffness k_s , resonant frequency f_0 , and critical buckling stress σ_{crit} of the PCDC can be modeled using FEM in COMSOL. The stiffness gives an

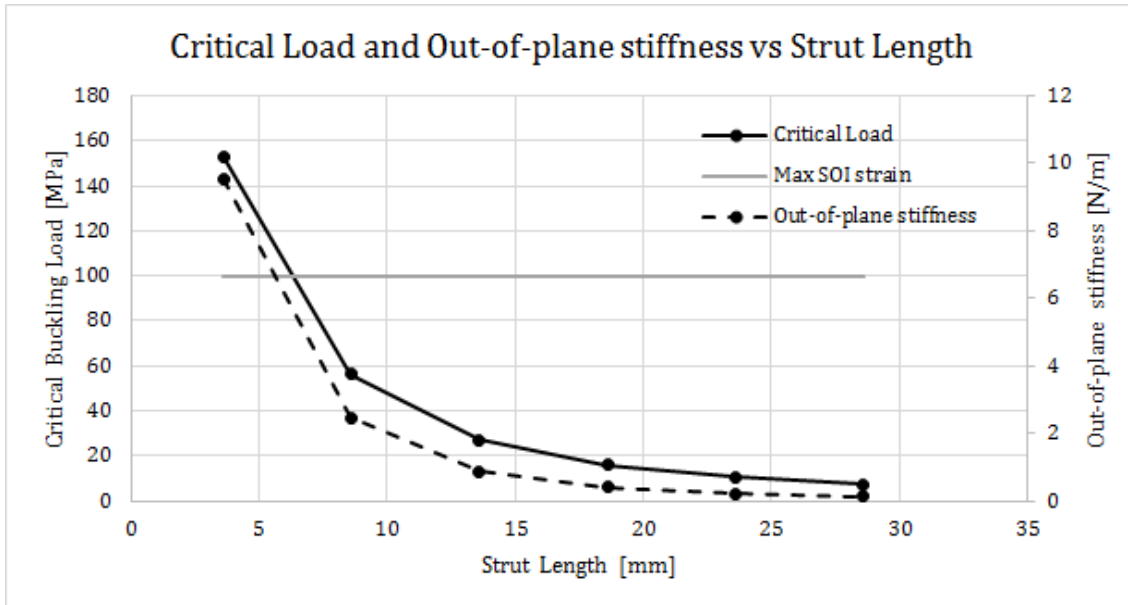


Figure 3.15: The relationship between the critical buckling load and strut length is shown for a membrane length of $L_{MEM} = 12.7\mu\text{m}$ and $L_w = 15.8\mu\text{m}$. Also shown in the relationship between out-of-plane stiffness and strut length.

indication of the sensitivity in terms of force while the resonant frequency should provide an indication of response times. Another important property of the PCDC sensor is the critical buckling load, or the minimum SOI stress required for buckling to occur.

A 2D free triangular FEM mesh was first generated automatically on the bottom surface of the PCDC device with min/max element sizes of $7\mu\text{m}/0.1\mu\text{m}$, growth rate 1.5, curvature factor 0.1, and a narrow region resolution of 0.5 with 4 iterations. A single layer mesh was swept across the 220nm thickness. Creating a mesh in this manner reduces the computation complexity for geometries that possess high aspect ratio [87].

3.3.1 Buckling in SOI

It is important to consider buckling as mismatches in thermal expansivity create residual compressive stress as high as 100MPa [76] in the top silicon layer that builds up during the SOI bonding process. Buckling is frequently a consideration in structural engineering where loading past some critical load causes a bifurcation and sudden deformation to a more energetically favourable state occurs. Like the photonic crystal, buckling may be expressed as an eigenvalue problem where the critical load and buckled shape represent the eigenvalue and eigenvector, respectively [88].

Although the buckled shape may be computed using this mathematical formulation, the amplitude of the buckled shape remains ambiguous as the unknown moments generated at the fixed ends create a family of possible solutions [88]. The height of the buckled membrane must

therefore be estimated by assuming that once the compressive stress is greater than the critical load σ_{crt} , the remaining SOI stress relaxes and increases the arclength along a path on the membrane connecting an opposing pair of fixed ends. Although custom MATLAB/COMSOL routines have been created to automatically compute the buckled shape and amplitude, for buckling problems, it is highly recommended to buttress numerical simulations with an analytic solution [88] (See Appendix D).

Three different designs are proposed based on whether or not the struts are predicted to buckle after under-etching.

- Non-buckled designs ($\sigma_{crt} > \sigma_0$)
- Buckled designs ($\sigma_{crt} < \sigma_0$)
- Buckle-compensated designs

For structures which do not buckle after oxide under-etch releasing, the resting point of the sensor is at zero deflection which is well suited for 1/4-bridge sensors. Despite the lower sensitivity, the benefit of such a design is predictability of the degree of buckling, or lack thereof, in addition to extremely fast response times.

Pre-deflection caused by buckling may be desirable as it can push the Q-point of the sensor into a linear regime. Full- and half-bridge sensors can benefit from buckling as the sensitivity vanishes at zero deflection. An additional concern of buckled designs is the snap-through effect, where a loaded structure suddenly buckles in the opposite direction. For this reason, buckled designs may be limited in their differential pressure measurements.

Yet a third family of designs may also be considered where buckling-mitigating structures are etched into the top silicon layer. The microbeam array designs, as proposed by Iwase *et al.* [76], can act as a spring which is able to relax the residual SOI stress while keeping the Si membrane in-plane.

3.3.2 Non-buckled Designs $\sigma_{crt} > \sigma_0$

The most important advantage to using a PC based directional coupler is the reduced coupling length when compared to rib waveguide. This is clearly seen in Fig. 3.16 where the coupling length is reduced by thirteen-fold for a PC coupler of equivalent air gap and waveguide width. The reduction in coupling length allows the fabrication of a class of PCDC designs which do not buckle after under-etching. This is not possible with rib waveguide directional couplers.

The enhanced coupling due to the PC virtually eliminates all unwanted coupling at the interfacing junctions. The pre-coupling is generally undesirable and often leads to additional design time spent offsetting the cross-talk effects of integrated photonic devices. Theoretically, short rib waveguide couplers can be constructed; however, the air gap separation must be less than 50nm, which places strict constraints on UV-based lithography processes.

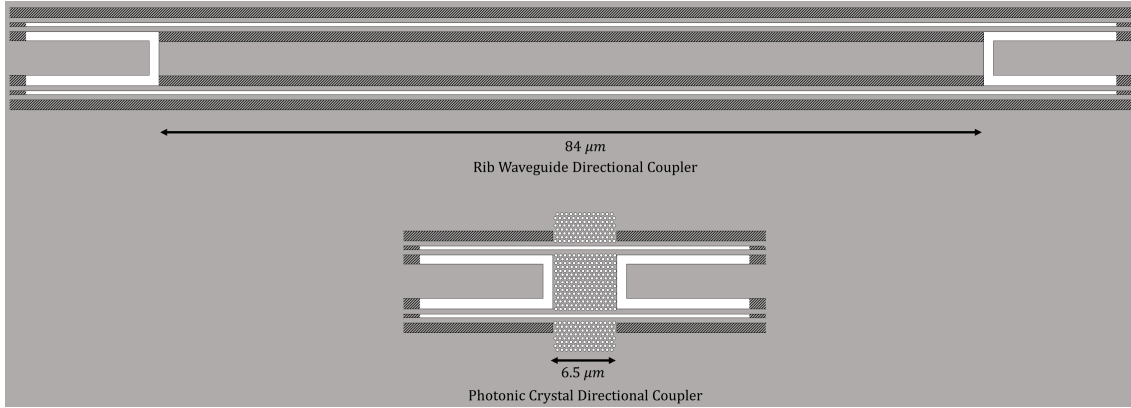


Figure 3.16: A rib waveguide (top) and photonic crystal (bottom) based $\frac{1}{4}$ -bridge directional couplers are shown. For an air gap separation of 200nm and waveguide width 540nm the coupling length is reduced thirteenfold.

Using single-crystal anisotropic silicon¹, the sensitivity of two non-buckled designs of varying width was computed using a linear elastic model in COMSOL. The average displacement across the membrane was computed for a total load of $1\mu\text{N}$ distributed uniformly across the surface and determined the out-of-plane spring constant k_s . The sensitivity S in terms of pressure may be computed using the PC membrane sensing area A .

$$S = \frac{S_{opt}A}{k_s} \quad (3.2)$$

Here, the strut length is set at $6.77\mu\text{m}$ which should set the critical load near the maximum SOI stress of 100MPa as determined by Fig. 3.15. The out-of-plane stiffness here should be approximately 6.5N/m. The sensor width L_w can be increased in order to increase the sensing area and enhance pressure sensitivity. For an air gap width 200nm, $N=1/4$ yields a sensor length $L_{MEM} = 6.47\mu\text{m}$. For a design of $L_w = 6.54\mu\text{m}$ the pressure sensitivity may be given by equation 3.2 as 0.67% full scale per kPa across a range of $100\%/S = 149\text{kPa}$. The specifications for PCDC sensors of varying membrane widths L_w is shown in Table 3.1

The total sensor resolution is largely dependent on the power of the light source and detector resolution. Assuming a 60dB dynamic range² for a laser/power-meter system, the PCDC sensor may be able to resolve 0.149Pa pressures.

3.3.3 Buckled Designs $\sigma_{crt} < \sigma_0$

Next we consider the case where the under-etched silicon membrane buckles. Obtaining post-buckled numerical simulation for the snap-through effect is a multi-step process as outlined in Fig. 3.17 and requiring two FEM models. First, linear buckling analysis is used to generate a

¹ $\langle 100 \rangle$ along sensor length, $\langle 010 \rangle$ along sensor width, $\langle 001 \rangle$ along out-of-plane direction

²based on Keysight N7744 power meter at 1kHz sampling rate

Table 3.1: The PCDC sensor performance at various specifications. $\lambda = 1550\text{nm}$

N	W [nm]	L_{MEM} [μm]	L_w [μm]	L_{str} [μm]	Rng. [nm]	S_{opt} [%/nm]	k_s [N/m]	S [%/kPa]	f_0 [kHz]	σ_{crt} [MPa]
1/4	200	6.47	15.89	6.77	0–600	0.105	6.36	1.71	1800	107
1/4	200	6.47	6.54	6.77	0–600	0.105	6.71	0.67	2840	101

normalized shape function. Using the arclength condition, a customized MATLAB function was able to estimate the amplitude of the buckled shape as a function of SOI strain σ_0 which is shown in Fig. 3.18. Typical σ_0 around 50MPa would generate approximately 500nm of deflection for a strut length around 21 μm . As σ_0 is known to vary even at different points the same die, very little can be done to further refine this estimation.

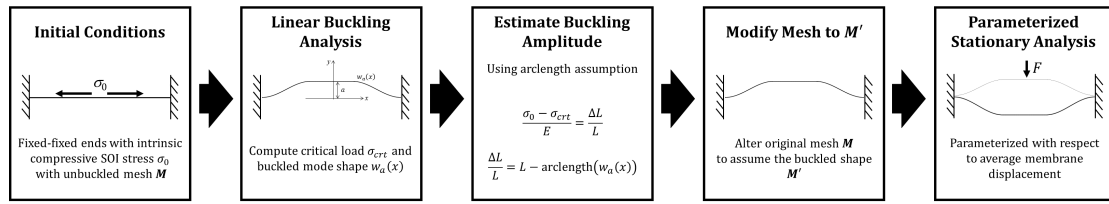


Figure 3.17: Post-buckling simulation procedure

A second FEM mesh is constructed based on the buckled mode shape at the prescribed 500nm amplitude using additional MATLAB code. Using the deformed mesh, the reactive force is computed using a nonlinear elastic model at parametrically prescribed displacements in order to generate the force-displacement curve shown Fig. 3.19 [89]. For a quarter-bridge sensor with $L_{str} = 21\mu\text{m}$ the snap-through force is .31uN which limits the prospects of buckled sensors as differential pressure sensing devices.

Table 3.2: The PCDC sensor performance at various specifications. $\lambda = 1550\text{nm}$

N	W [nm]	L_{MEM} [μm]	L_w [μm]	L_{str} [μm]	Rng. [nm]	S_{opt} [%/nm]	k_s [N/m]	S [%/kPa]	f_0 [kHz]	σ_{crt} [MPa]
1	300	41.57	15.89	21.72	400–1000	0.172	0.146	777	125	6.99
1	200	26.27	15.89	21.87	400–800	0.228	0.189	510	176	9.27
1/2	200	12.77	15.89	21.12	200–600	0.215	0.339	128	284	12.7

Due to the longer strut member and enhanced sensitivity, the buckled sensors are up to 700 times more sensitive than previously discussed sensors in terms of pressure. Assuming a fixed dynamic range of the interrogating equipment, there is a trade-off between the possible range of pressures that may be measured and the sensitivity. The sensing range may be improved somewhat by reducing the strut lengths. However, as shown in Fig. 3.18, the unpredictability

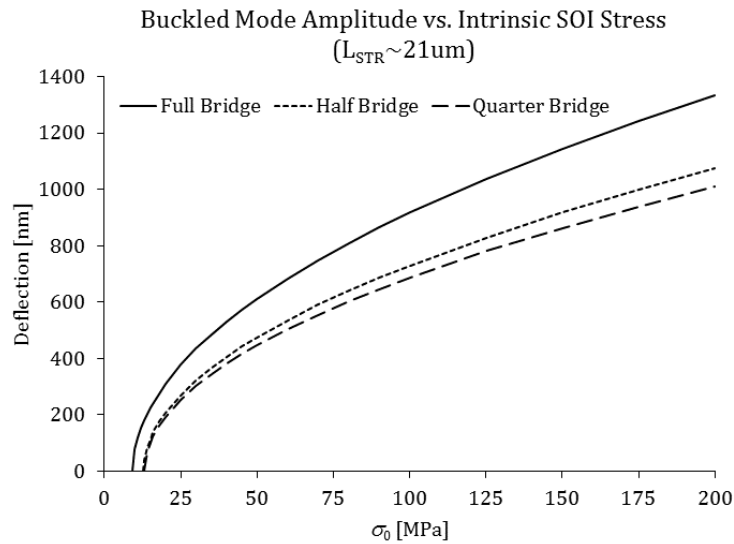


Figure 3.18: Expected buckling amplitude as a function of intrinsic SOI strain σ_0 . The strut length is approximately $21\mu\text{m}$

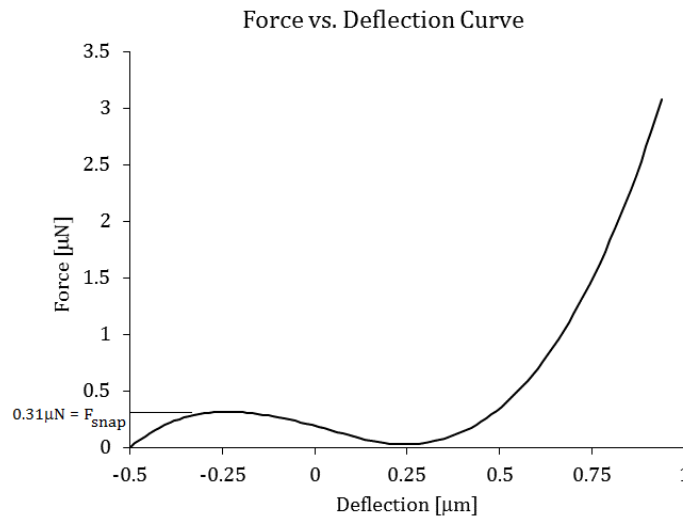


Figure 3.19: The COMSOL generated force-deflection curve is shown for parametrically prescribed displacements for the 28-hole buckled structure with specifications found in Table 3.2. The initial buckling amplitude was set to 500nm corresponding to a reasonable initial stress of about 50MPa . The snap-through event can be seen to occur at about $0.3\mu\text{N}$ of force.

of the buckling amplitude becomes exacerbated where $\sigma_{crit} = \sigma_0$. Thus, designs where the critical buckling load of the PCDC device is near the expected SOI strain is to be avoided.

3.3.4 Buckle Mitigated Designs

Buckling compensation is needed for longer bridge designs where the σ_{crit} falls below the intrinsic SOI stress. Buckle-compensated structures may be implemented using a microbeam array following the designs outlined by Iwase *et al.* [76] depicted in Fig. 3.20. For compensated designs, the membrane does not buckle and lies on the same plane as the SOI, therefore lifting the uncertainty associated intrinsic SOI stress without placing an upper limit on sensor length. Since the sensor membrane lies in-plane, and due to the longer sensor lengths, quarter-bridge designs with wide air gaps are well suited for these designs. This effectively improves the design stability as the internal stress varies quite widely in addition to relaxing lithography resolution constraints with regard to the air gap width.

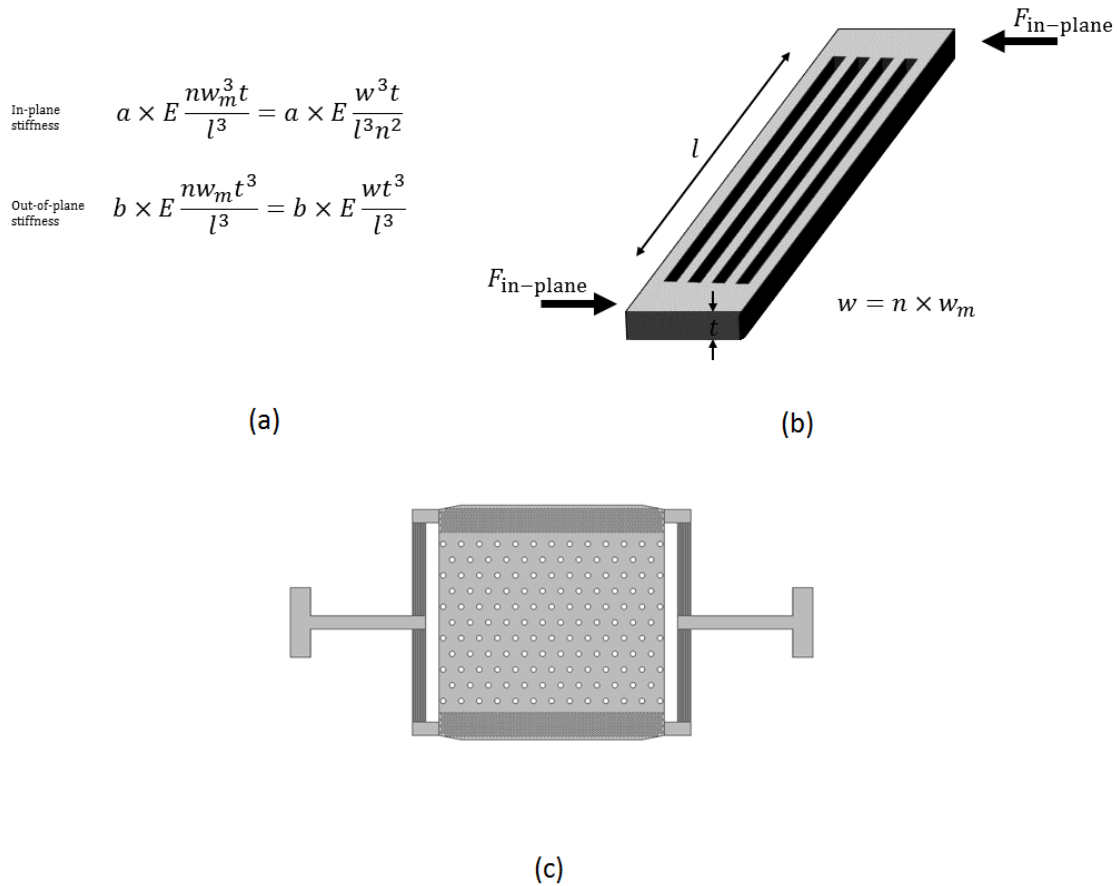


Figure 3.20: (a) The in-plane stiffness may be dramatically decreased using a (b) microbeam array with multiple beams. Figure based on [76]. (c) These structures may be integrated into the current PCDC design.

Two PCDC membrane structures, with and without buckle mitigation, were compared using FEM simulation. Each structure contains equivalent support strut cross sectional area ($900\text{nm} \times 220\text{nm}$), however, the buckle-mitigated design distributes the strut cross section into

six beams measuring 150nm each, directed laterally so as to absorb the intrinsic stress, like a spring. As shown in Table 3.3, the critical buckling load can be dramatically increased without significant compromise in sensor size or sensitivity. Such buckle-mitigated designs are essentially independent of intrinsic SOI strain and clearly an improvement in design stability particularly for longer designs where buckling is expected to occur.

Table 3.3: A comparison of buckle-compensated and uncompensated designs. The critical buckling load may be dramatically increased without major consequence

N	W	L_{MEM}	L_w	L_{str}	Rng.	S_{opt}	k_s	S	f_0	σ_{crit}
	[nm]	[μm]	[μm]	[μm]	[nm]	[%/nm]	[N/m]	[%/kPa]	[kHz]	[MPa]
1/4	750	28.06	29.06	15.97	0–1000	0.0138	0.253	74.0	190	18
1/4	750	28.06	29.06	15.97	0–1000	0.0138	0.185	101	165	11300

The sensing range of these devices in terms of force are 0–253nN and 0–185nN for the uncompensated and buckle-compensated structures, respectively. Although the sensing range is quite low, they can be made extremely sensitive; capable of making measurements as small as 0.185–0.253pN using a 60dB power meter. The mass of the PCDC membrane is 1.44×10^{-13} kg and exerts a force of 1.41pN in earth’s gravity. Thus, these large area PCDC sensors may be able to detect their own weight making them perhaps more suitable for accelerometer applications.

3.4 Conclusion

The target PCDC thickness of $T=220$ nm, PC lattice pitch $\Lambda=450$ nm, PC hole diameter $D=270$ nm, edge width $E=540$ nm, and air gap separation $W=200$ nm were selected based on the various design constraints and strategies presented in this chapter. Three PCDC sensor designs were considered based on presence of buckling due to compressive SOI stress. The smallest designs, which are not predicted to buckled, have a pressure sensing range of 149kPa which is well suited for measuring microfluidic flow rates based on differential pressure measurements.

Distributing the lateral PCDC supporting members into six microbeams can enable the PCDC sensor to remain in-plane after under-etch. Larger designs, that are either buckle-compensated or uncompensated, are shown to be much more sensitive with a trade-off in sensing range while assuming a fixed dynamic range of the interrogating instrumentation. Using a 60dB power detector, these designs should be capable of detecting their own weight and are perhaps more useful as accelerometers. Next, the device layout and fabrication outline is presented.

Chapter 4

Process Flow

4.1 Fabrication Overview

The PCDC sensors intended for optomechanical testing were constructed using the IMEC ePIX-fab process with the post-process under-etching done at University of Western Ontario (UWO) nanofab. Fabrication of the buckle-mitigated devices was also done at UWO Nanofab and do not feature the fiber optic surface grating coupler interface. These buckle-mitigated membranes are not intended to be optically functional. The overall fabrication process of the PCDC is shown in Fig. 4.1.

The rationale for outsourcing the fabrication of the optical devices is access to established surface grating coupler (SGC) designs which allow easy interfacing with the silicon photonic chip. Coupling directly to the surface of the chip not only improves testing repeatability, but increases the density of possible designs which is needed for offsetting fabrication biases.

4.2 CMC-IMEC Silicon Photonics Foundry MPW

The IMEC technology run is a CMOS-based process done at the ePIXfab using $0.13\mu\text{m}$ mask technology. In order to minimize costs, the die project space is shared among many researchers as a multiproject wafer (MPW). An e-beam generated mask is used during a patterned deep UV lithography (193nm) step followed by ICP-RIE at the prescribed etch depths. The dimensions after subsequent dicing and the final PCDC project space is shown in Fig. 4.2. Each participant in the MPW receives five chips.

4.2.1 Layout

Within the project space, a total of 54 different design instances were implemented plus an important blank design needed for characterizing the SGCs. Although the PCDC sensor itself

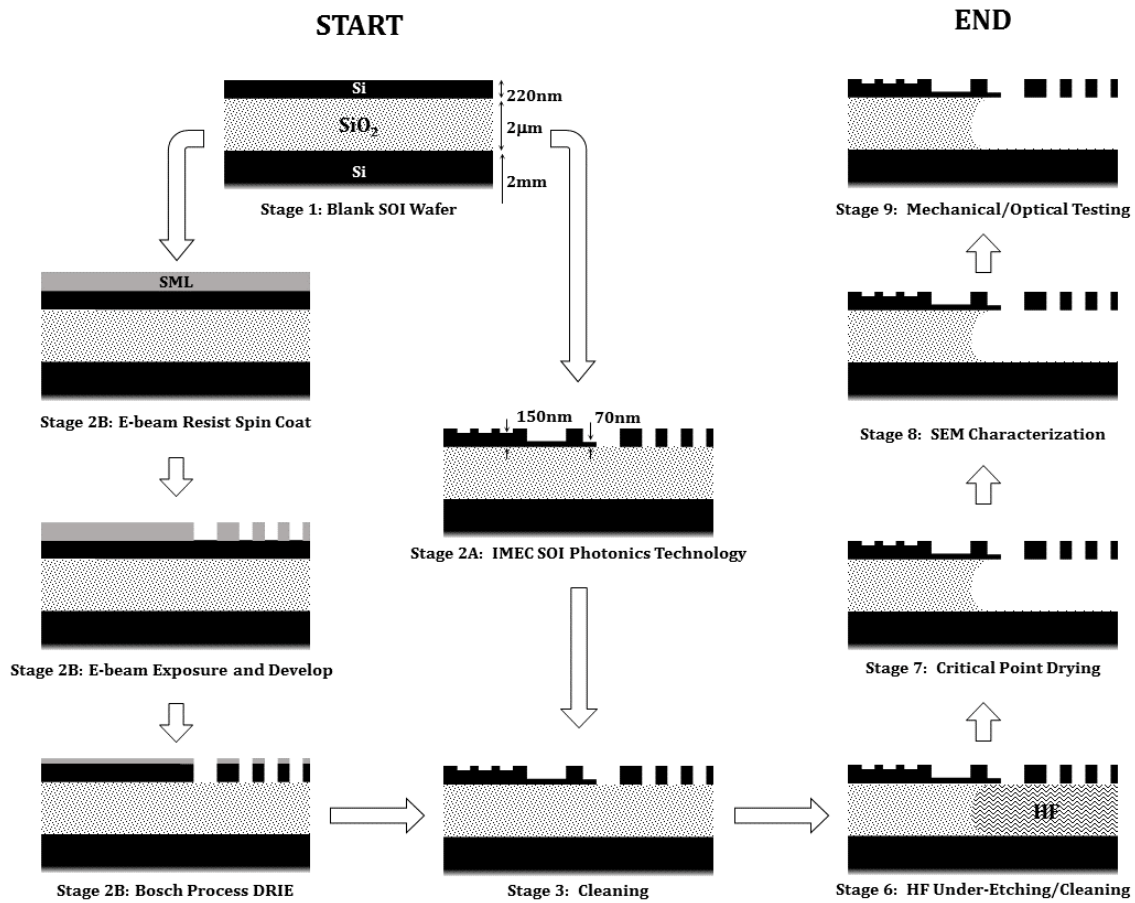


Figure 4.1: The process flow of the PCDC fabrication including IMEC and Nanofab processes.

requires very little area, there are other factors which limit the number of designs. Rapid prototyping will be done using a customized silicon photonics microsystems integration platform (SiPh-MIP) which features a fiber-optical array with a $127\mu\text{m}$ interstitial fiber distance. The period of the interfacing fiber array, therefore, determines the spacing of the grating couplers on the layout.

Sufficient clearance is also required between the sensor and SGCs of the optical i/o interface. Testing and characterization of the sensor will be done using an atomic force microscope (AFM) apparatus which may encroach the chuck of the fiber array during optomechanical testing. Thus, the fiber-grating couplers are placed $600\mu\text{m}$ away from sensor. These test bench constraints can be offset somewhat by interleaving pairs of sensor design.

Maximizing the number of designs on the project space is crucial as additional designs are required to offset biasing during fabrication. There are three critical design parameters: E , W , and D . The lattice pitch Λ is considered to be stable throughout the fabrication process while E and W are assumed to be strongly correlated as observed in Fig. 4.3.

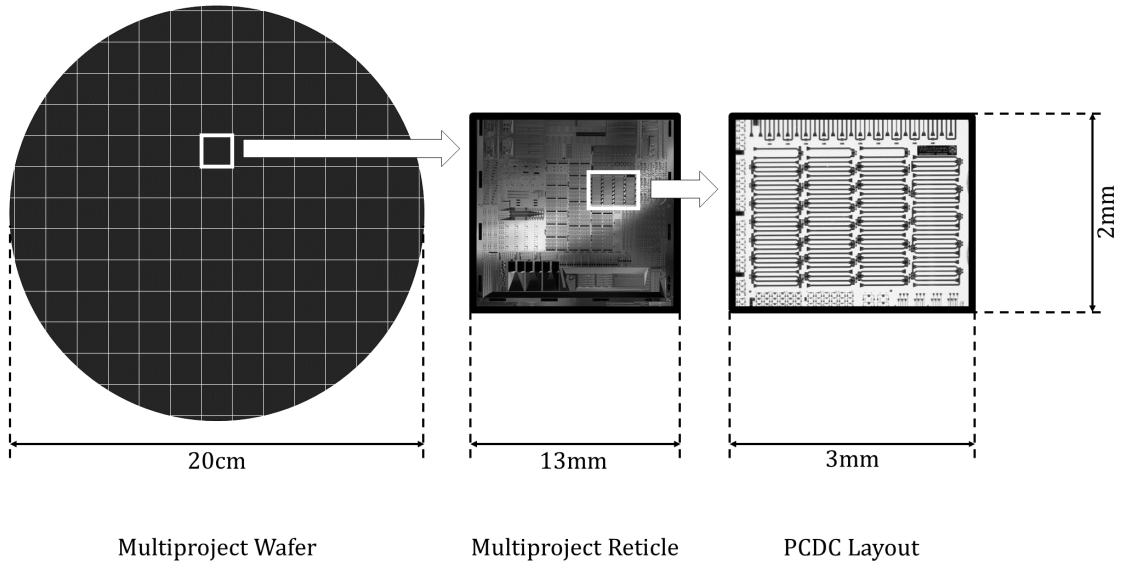


Figure 4.2: Overview of the MPW dicing process and layout. An eight inch wafer includes about 120 repeated reticles etched using stepped UV lithography. The PCDC project workspace is 3mm \times 2mm.

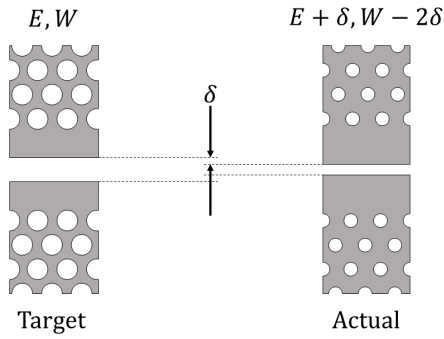


Figure 4.3: The sum $2E + W$ is assumed to be stable despite fabrication biasing.

The variation in the hole diameter is expected to lie between -50nm to $+10\text{nm}$ depending on the UV dosage used. Less variation is expected in the width of the air gap/edge which could be $\pm 10\text{nm}$ around the target dimension. By understanding the most important effects of these variations on the PCDC design, more designs can be used to increase the likelihood of a faithful representation of the intended design. PWE was used to estimate these effects and is summarized below.

$$\frac{\Delta L_c}{\Delta D} = -38\text{nm/nm} \quad \frac{\Delta \lambda_0}{\Delta D} = 0.94\text{nm/nm}$$

$$\frac{\Delta L_c}{\Delta W} \Big|_{\frac{\partial W}{\partial E} = -2} = 52\text{nm/nm} \quad \frac{\Delta \lambda_0}{\Delta W} \Big|_{\frac{\partial W}{\partial E} = -2} = -0.67\text{nm/nm}$$

The central wavelength position is strongly related to the PC holes size. Since large variations are expected in the PC hole size, many different diameters must be included on the layout

in order to ensure operation near 1550nm. Since the fabricated PC hole diameters are likely to be smaller, four different hole diameters at 320nm, 300nm, 280nm, 260nm are used to target 270nm.

Rather than varying the air gap W , various sensor lengths are used instead. Thus, coupling may still be studied without mechanical deflection of the membrane by examining the output intensity of varying sensor lengths. Four different sensor lengths selected are $\pm 3\frac{1}{3}\%$ and $\pm 10\%$ of the target sensor lengths.

4.3 UWO Nanofab Fabrication Process

Post-processing of the IMEC project chips was done here at the UWO Nanofab facility. The chips were coated with a protective silicon nitride layer that is easily removed using acetone. Nanopatterning, wet-etching, and critical point drying (CPD) of the buckle-mitigated designs was done at UWO. Deep reactive ion etching (DRIE) of these patterned designs was outsourced to Toronto Nanofabrication Center (TNFC).

The buckle-compensated structures were designed separately, outside of the IMEC run, and fabricated at UWO Nanofab. Since the I/O SGCs were available only the PDK cell library in conjunction with the highly calibrated triple-etch depth IMEC process, these compensated structures are not optically functional. These devices were fabricated in order to validate the buckle-compensated structures and calibrate the under-etch and drying process without sacrificing the valuable IMEC chips.

4.3.1 E-beam Lithography

E-beam lithography was used to nanopattern the buckle-mitigated devices. The e-beam lithography begins with the creating the Nanometer Patter Generation System (NPGS) CAD file. Designs were created using DesignCAD 3D MAX 24 and imported using a COMSOL .dxf file.

Next, the SML based e-beam resist (SML1000 and Anisol casting solvent 1:1) was spin coated on a 4×4cm SOI wafer:

- 5 seconds 500 rpm
- 20 seconds 4000 rpm
- 10 seconds run down
- 2 minutes pre-bake at 180C

After spin coating, the SOI sample is broken 16 1×1cm chips. Ellipsometry and scanning electron microscope (SEM) imaging estimate the resist thickness to be approximately 400nm. Electron beam exposure was done using the LEO 1530 field emission SEM at 30kV with

10 μ m aperture. In order to create the desired geometric dimensions, an array of test patterns with varying dosages is used to find the correct exposure. Stable features were observed for 360 μ C/cm² where exposure is confirmed across the full resist thickness.

SEM imaging of the test structures after 4nm osmium deposition revealed a geometric biasing and required further adjustments within the NPGS CAD file itself as the thin strut members appeared 40nm smaller and the PC hole diameter appeared 10nm larger. The buckle-compensated CAD designs were appropriately modified, exposed, and developed.

Development of the SML resist proceeds as follows:

- 30 seconds in Amyl Acetate (Developer)
- 30 seconds rinse in Isopropynol
- air dry N₂

Ten chips, each measuring about 1x1cm, were developed each containing an identical array of different designs.

4.3.2 Deep Reactive Ion Etching

After development, the top silicon layer of the chips were ready to be etched using a DRIE (deep-reactive ion etching) process done at the Toronto Nanofabrication Center. DRIE is an anisotropic etch process using a combination of physical bombardment and chemical reactivity to achieve near vertical structures. The DRIE process, commonly used for etching silicon, includes alternating passivation using C₄F₈ and etch using SF₆. The passivation, which is chemically inert to the etch, protects the vertical walls generated during etching which are less affected by the physical bombardment of ions.

As with all standard lithography procedures, the resist that remains after developing protects the top silicon layer during the etch process. It is important to consider the selectivity of such an etch process. The etch rate of the silicon using PlasmaPro Estrelas 100 DRIE is 25 μ m/min with the Bosch process [90]. The estimated etch rate of the SML resist is 22nm/min and therefore provides excellent selectivity.

4.3.3 HF Under-Etching

In order to release the bridge, buffered HF is used to isotropically under-etch the buried oxide (BOX) layer of the SOI and release the membrane. For the IMEC samples, acetone is used to remove the protective resist. The buckle-compensated samples are prepared by cleaning for 30 minutes in heated PG remover at 70 degrees Celsius under cover and monitoring. The buffered HF solution consists of 6:1 volume ratio of NH₄F(40%):HF(48%) with an etch rate of about 100nm per minute at room temperature. Since the BOX layer extends 2 μ m deep, the chips are left in the HF for approximately 25 minutes.

4.3.4 Critical Point Drying

Directly after HF etching, the chips are immersed in water in order to wash and dilute residual acid. The structures must remain wet and dried very carefully with minimal surface tension in order to prevent collapse of the membrane. This may be achieved using the critical point drying (CPD) of carbon dioxide. By carefully managing the temperature and pressure, CO₂ may be brought to its critical point (31.1°C at 7391kPa) where liquid, vapour, and gas exist in equilibrium. Here, the latent energy required for evaporation goes to zero and no additional energy is required for CO₂ molecules to escape the surface tension.

Since liquid CO₂ is immiscible with water, the chips are immersed in ethanol after being washed. The chips are then quickly transferred into a customized holder inside the CPD chamber which is prefilled with ethanol. Several purging cycles with liquid CO₂ at 5°C are used to replace ethanol. Sufficient purging can be confirmed by the dryness of the CPD vessel exhaust as the carbon dioxide quickly evaporates leaving the liquid ethanol.

After purging, the CPD chamber is filled with liquid CO₂ to the prescribed halfway point of the vessel and hermetically heated past its critical point to 35°C. The volume of the CPD vessel is such that the critical pressure is attained while crossing the critical temperature. After drying, the CO₂ is slowly released isothermally to prevent recondensation. The chips are now ready for SEM imaging and testing.

4.3.5 SEM Characterization

In order to validate the dimensions of the sensor features, the chips are inspected under a scanning electron microscope (SEM) under 2-3kV with 30um aperture. Fig. 4.4 shows the IMEC-fabricated 28-hole half-bridge design. A close up of the IMEC-fabricated structure shows designs biased with a PC hole diameter 320nm generated the correct target hole diameter 270nm. The air gap separation is also observed to be near the 200nm target. These designs were associated with the X01, X03, X05, and X07 labels as specified in Appendix E.

The buckle mitigated structure as shown in Fig. 4.5 has been released and has maintained its integrity throughout the CPD process. Closer inspection of the microbeam array revealed the beams are slightly smaller than the expected 50% fill ratio. However, this is not expected to affect the design significantly.

4.4 Conclusion

Target design parameters $\Lambda=450\text{nm}$, $D=270\text{nm}$, $E=540\text{nm}$, and $W=200\text{nm}$ have been successfully fabricated on SOI for first-generation PCDC sensors, utilizing CMOS-based technology. Buckle-mitigated structures were successfully nanopatterned using SEM and surface machined using DRIE. Structural integrity was maintained during HF wet-etching and subsequent CPD.

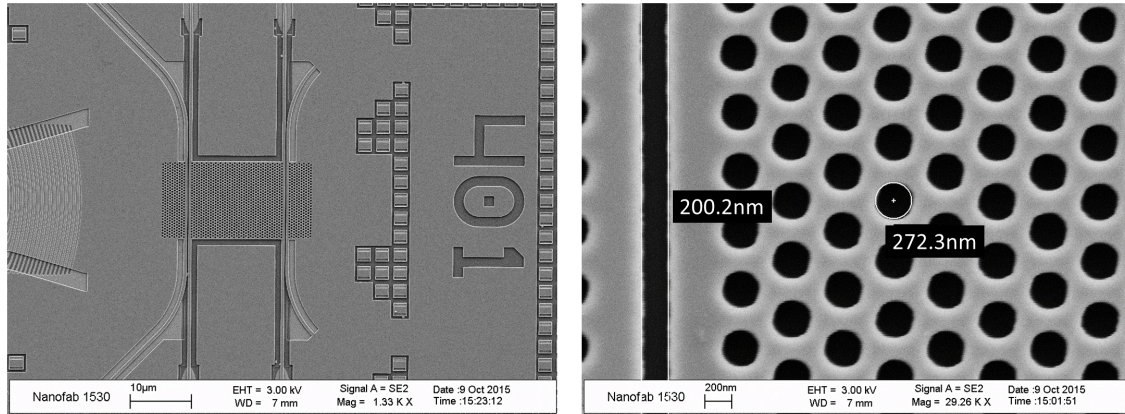


Figure 4.4: SEM image of a IMEC run half-bridge structure before HF under-etching. Structures with design No. X01 contain the correct hole radius and air gap separation.

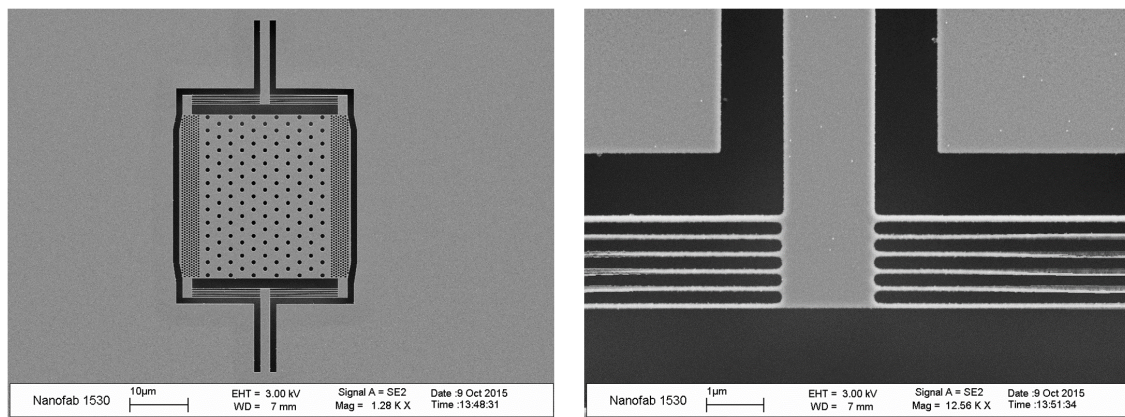


Figure 4.5: SEM image of buckled mitigated design using a micro-beam array structure.

Next, the operating principle of the PCDC will be evaluated in addition to the effectiveness of buckle-mitigating techniques.

Chapter 5

Sensor Measurements and Evaluation

5.1 Introduction

The PCDC sensors were tested using a newly assembled customized silicon photonic microsystems integration platform (SiP MIP)¹ and interfaced using surface grating couplers (SGCs). For the buckling compensated structures, optical profile measurements were used to confirm the reduced buckling amplitude.

5.2 Sensor Measurement Procedure

The control system and optical interface of the SiPh-MIP is shown in Fig. 5.1 and Fig. 5.2, respectively. The fiber array was brought very near to the chip ($<100\mu\text{m}$), which sits atop the X,Y actuating stage. The stage has been carefully leveled with respect to the polished end of the fiber array using stage tuning machines. The polarization is important, as not only the SGCs are polarization sensitive, but the PCDC devices themselves. For the desired TE polarization, fiber array ports 5-8 are used to interface the SGCs on the chip.

Optimum alignment of the fiber array to the SGCs was achieved using a MATLAB alignment routine created by Maple Leaf Photonics. First, coarse alignment of the fiber array was done visually using the CCD microscope. Next, the fiber array raster scans the area of interest and a heat map was generated which indicates regions where light is strongly coupled into one SGC and collected from another. The heat map indicates the strength of light emanating from the outgoing SGC and the corresponding stage coordinates. The fiber array can be commanded to the SGC hot-spot and a fine alignment routine using gradient and cross-hair methods ensures optimized coupling to the device.

Transmission from a blank device that was included on the chip allowed the SGC transfer function to be acquired allowing the PCDC device transmission to be normalized. The trans-

¹Developed and procured by CMC Microsystems

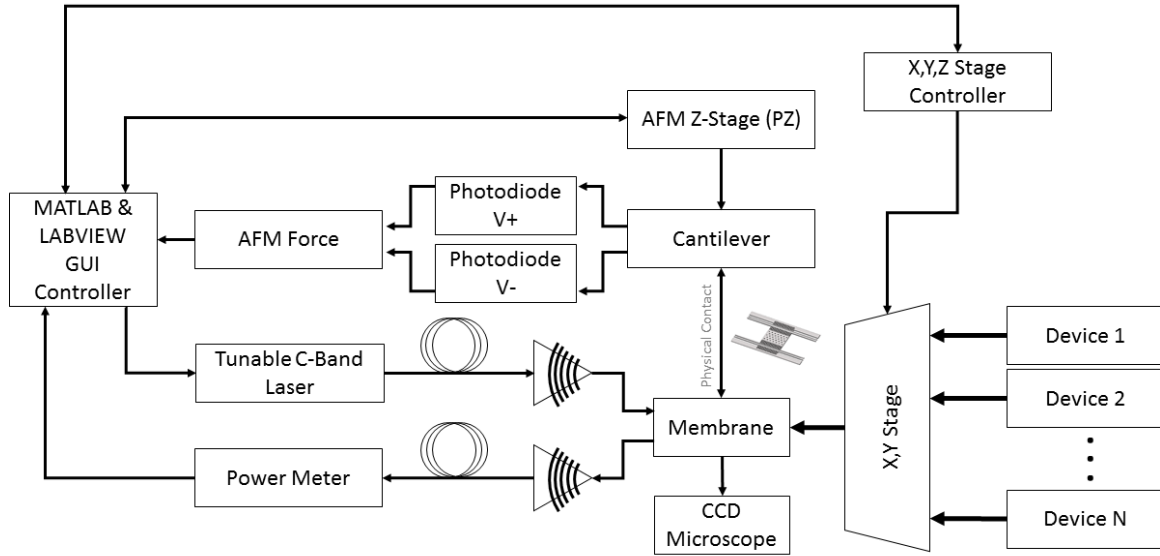


Figure 5.1: The control system for the SiP MIP with customized with an AFM driver (yet to be integrated). The MATLAB GUI allows the die stage ($\Delta x = \Delta y = 100\text{nm}$) to moved and select a device for testing.

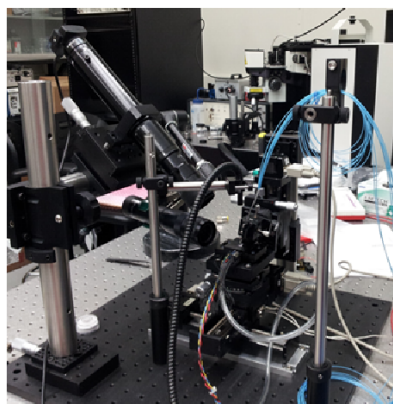
mission characteristics of the blank device are shown in Fig. 5.3 for various fiber array angles away from the vertical. The transmission spectra was measured using a LABVIEW routine in concert with a tunable laser and power meter. The angle of the fiber array determines the k-matching condition and provided a means for adjusting the transmission window.

The strongest coupling to the SGCs can be observed near 5 degrees where a minimum 20dB loss occurs near 1565nm. Using this transmission spectrum, a link budget may be created to select an appropriate power meter range. Here, the power received P_{RX} is related to the source power P_{TX} , fiber-to-SGC losses $L_{F \leftrightarrow SGC}$, rib waveguide-to-PCDC losses $L_{RB \leftrightarrow PCDC}$, and a 3dB/cm line loss [91] for about 1.3mm of rib waveguide L_{RB} .

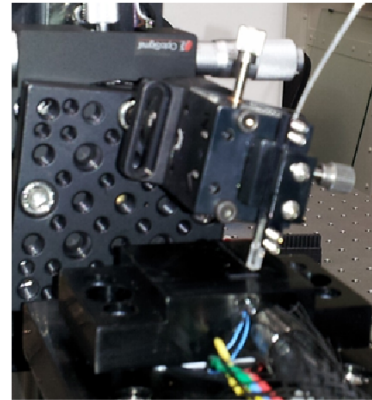
$$P_{RX} = P_{TX} - 2L_{F \leftrightarrow SGC} - 2L_{RB \leftrightarrow PCDC} - L_{RB} \quad (5.1)$$

$$-12.4\text{dBm} = +10\text{dBm} - 2(10\text{dB}) - 2(1\text{dB}) - 0.4\text{dB} \quad (5.2)$$

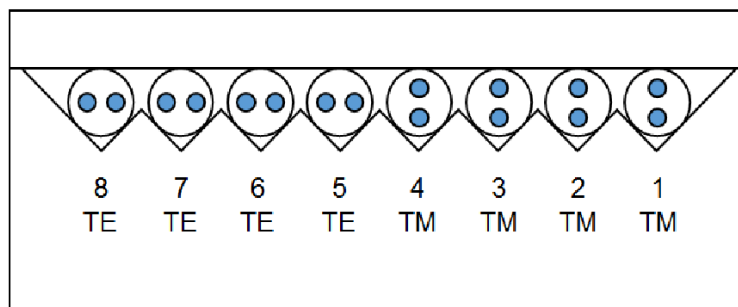
The current test bench is configured to use a 10dBm source. The peak power expected to be received is approximately -12.4dBm, or about $58\mu\text{W}$, using the 5 degree fiber array angle. An *in situ* atomic force microscopy (AFM) probe has yet to be integrated. Therefore, transmission measurements are restricted to devices that have not been under-etched.



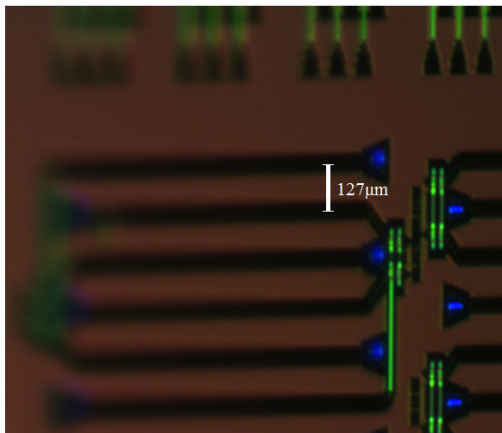
(a)



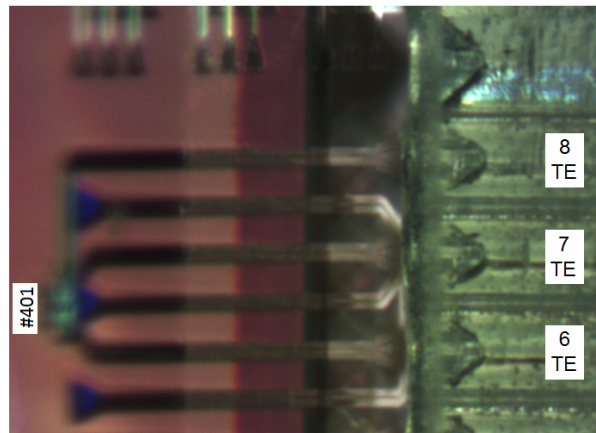
(b)



(c)



(d)



(e)

Figure 5.2: (a) Overall optical test bench is shown. (b) Close up of the fiber array and chip stage. (c) Fiber array cross section with 1-4 ports TM polarization and 5-8 ports TE polarization. (d) The CCD camera is set at an angle with respect to the chip and can only focus on the SGCs. (e) The interstitial fiber array, shown with the polarization labeled, distance is $127\mu\text{m}$, providing a unit of reference.

5.3 Optical Measurements

The PCDC sensors were evaluated before the buried oxide (BOX) layer was removed in order to expeditiously confirm proper operation. In this case, the PCDC membranes remain fixed to the BOX layer and lie at the known in-plane position that can be easily modeled and back-checked using FDTD simulation. In spite of the associated power leakage into the oxide, PCDC coupling can still be confirmed by observing the transmission spectrum of devices which have both output ports accessible. Additionally, the coupling lengths at specific frequencies may also be estimated by analyzing the transmission minima and crossing points. Thus, optical testing was concentrated on the half-bridge coupler designs (#401 and #403) where both ports are accessible.

Transmission measurements for devices #401 and #403 are shown in Fig. 5.4 which were normalized with respect to the 5 degree fiber array transmission. Coupling was confirmed as the power sum between the two ports remains relatively constant $-7.1\text{dB}\pm 0.5\text{dB}$ up to 1578nm where the even mode resonance occurs. In this slow-light regime, the coupling length is expected to rapidly shrink as the even mode dispersion approaches zero. For wavelengths greater than 1578nm, only the odd mode is supported and coupling no longer occurs.

By analyzing the critical points of the transmission spectra, the coupling lengths can be inferred by assuming the first minima of the coupled output represents the full-bridge ($N = 1$) configuration, where light completes a full cycle between the two waveguides. Subsequent minima from the coupled output will yield higher integer couplers. Similarly, the minima of the through-output indicate half-bridge configurations, while the transmission crossings represent quarter-bridge configurations, where power is equally shared between the two output ports. The results are summarized in Tables 5.1, 5.2, and Fig. 5.5.

In general, the bridge number N may be determined using the ratio of transmitted output power $\Delta\text{dB} = I_{\text{coup}(\text{dB})} - I_{\text{thru}(\text{dB})}$. Re-arranging eq.2.15 and eq.2.16 yields

$$N = \frac{\arctan\left(\pm 10^{\frac{\Delta\text{dB}}{20}}\right)}{\pi} + m\frac{1}{2} \quad (5.3)$$

where m is an integer. Care must be used with this formula as m must be advanced at each passing of a minima in addition to a flip the arctan argument sign. The coupling length is observed to remain constant across 1540–1510nm where a 38%:62% directional coupler is formed.

This agrees with RSOFTE air-slab-air simulation which predicts a rapidly changing coupling length based on even and odd Δk with a even resonance occurring at 1582.1nm. FDTD simulation with the BOX layer is shown in Fig. 5.6 and agrees quite well in terms of varying coupling length and losses, despite the 20nm wavelength shift.

Table 5.1: #401 Coupling Lengths (with BOX) $L_{MEM} = 12.77\mu\text{m}$ (28 Holes)

$N = \frac{KL_{MEM}}{2\pi}$	$L_c = \frac{L_{MEM}}{N}$	λ_0
No.	[μm]	[nm]
0.7109	17.69	1510–1540
3/4	17.03	1549.0
1	12.77	1564.6
5/4	10.21	1570.6
3/2	8.51	1573.5
7/4	7.30	1575.2
2	6.39	1576.8
9/4	5.68	1577.5
5/2	5.11	1577.7
11/4	4.64	1577.85
3	4.26	1577.9

Table 5.2: #403 Coupling Lengths (with BOX) $L_{MEM} = 14.57\mu\text{m}$ (32 Holes)

$N = \frac{KL_{MEM}}{2\pi}$	$L_c = \frac{L_{MEM}}{N}$	λ_0
No.	[μm]	[nm]
3/4	19.42	1510–1530
1	14.57	1558.6
5/4	11.66	1566.0
3/2	9.71	1570.4
7/4	8.33	1573.1
2	7.29	1574.5
9/4	6.46	1575.55
5/2	5.83	1576.4
11/4	5.30	1576.7
3	4.86	1577.1

5.4 Evaluation of Buckle-Compensation Structures

Using optical profilometry², the topography of compensated and uncompensated structures were compared in order to validate the buckling mitigating design. The two structures are located next to one another on the same die in order minimize the variation of expected SOI stress. The results are summarized in Fig. 5.7. Here, the uncompensated structure can be observed to buckle with an amplitude of approximately 330nm indicating an intrinsic SOI stress of approximately 35MPa. The profile of the compensated structure is seen to lie nearly

²Veeco WYKO NT1100 (Phase shift interferometry)

flat with amplitude of approximately 60nm. Clearly, the compensated structure is desensitized to the intrinsic SOI stress which is generally unknown *a priori*.

5.5 Conclusion

Coupling lengths of 5–20 μm have been demonstrated on PCDC structures that have yet to be under-etched. These results agree with FDTD simulation. Despite an unexplained 20nm shift in wavelength, the operating principle has been validated. Successful fabrication and buckle mitigation validates a key aspect of the PCDC optomechanical sensor design and is highly relevant to the edge-based mechanism. In the near future, an AFM will be incorporated with the SiPh-MIP and the IMEC-fabricated designs can be under-etched and evaluated.

IMEC SGC Transmission at Different Fiber Array Angles

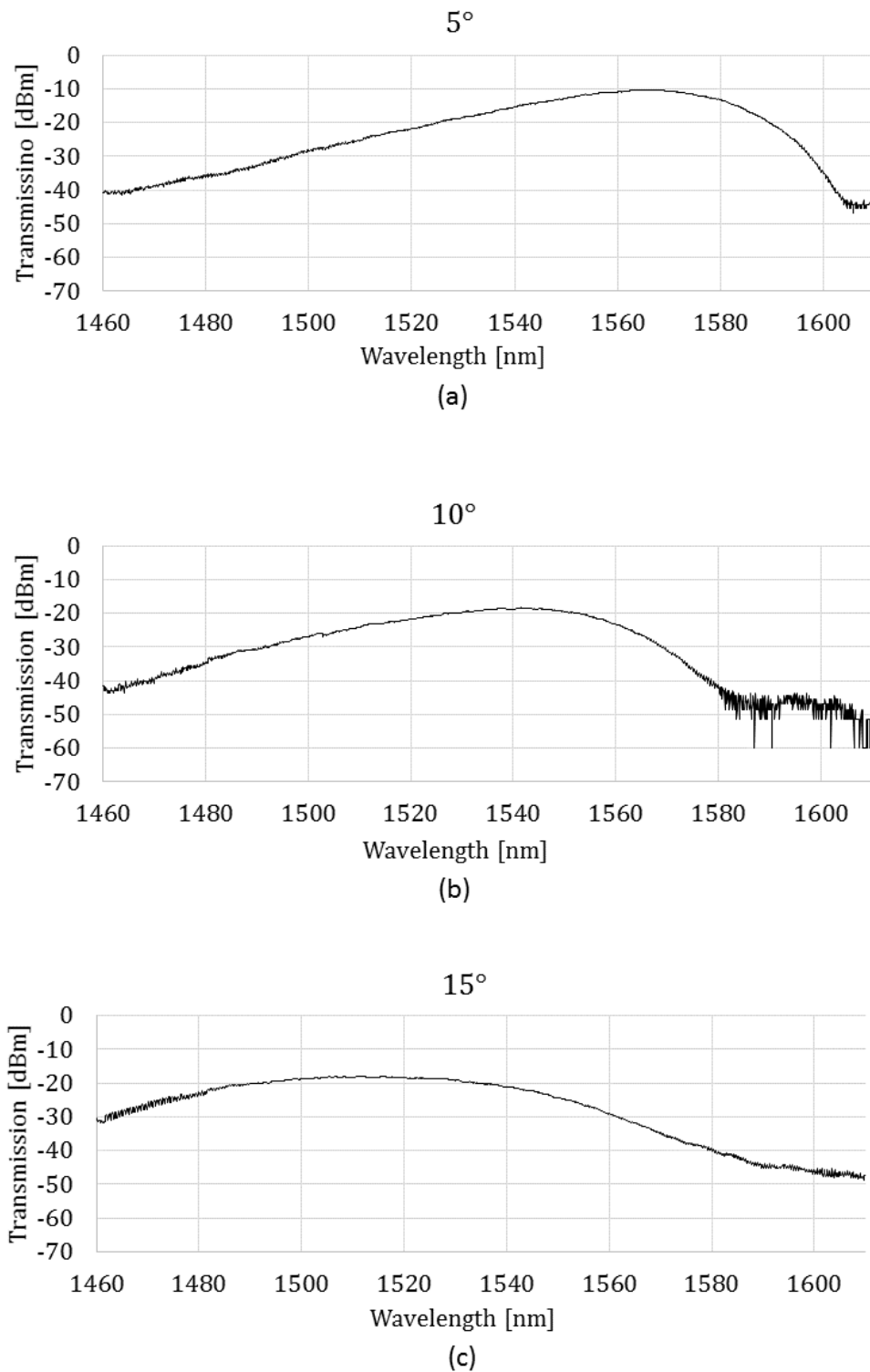


Figure 5.3: Blank device transmission characteristics for associated fiber array angles (a) 5 degrees, (b) 10 degrees, and (c) 15 degrees away from the vertical. A 10dBm source with 1460–1610nm wavelength sweep and 1s settling time was used to generate the spectrum.

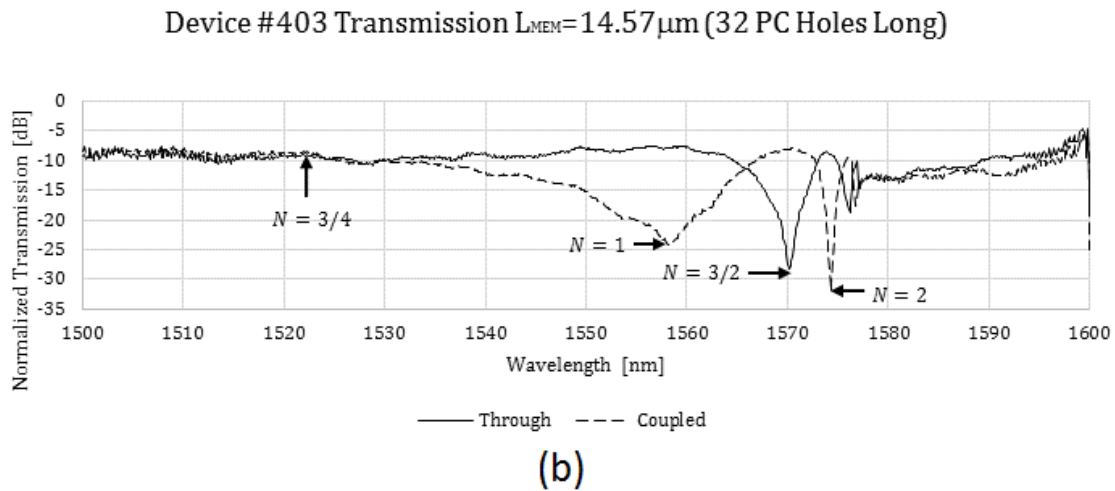
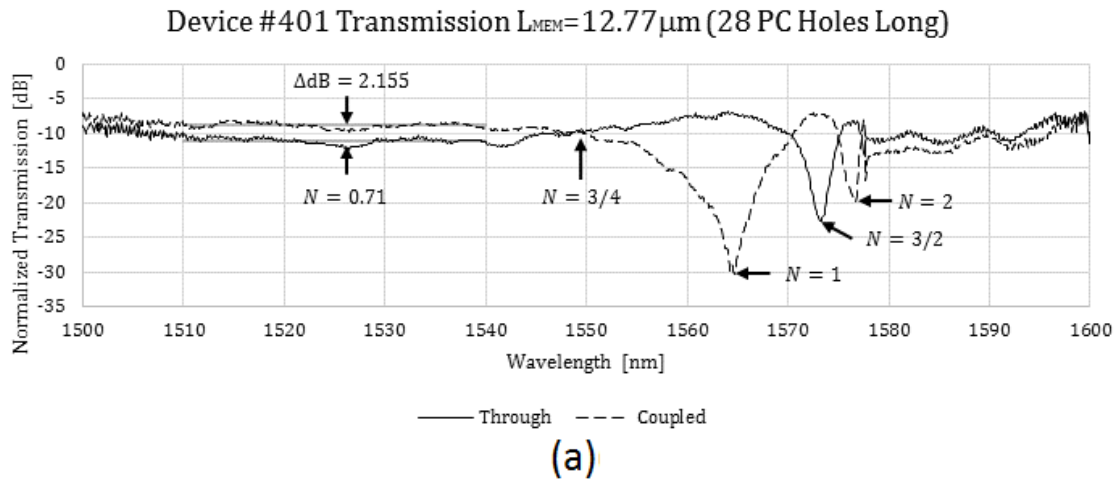


Figure 5.4: Normalized transmission of PCDC devices of length (a) $12.77\mu\text{m}$ and (b) $14.57\mu\text{m}$ are shown. Using the transmission minima and crossing points, the coupling length may be inferred at the corresponding wavelength. Near 1578nm , the coupling length changes rapidly due to zone folding of the even mode.

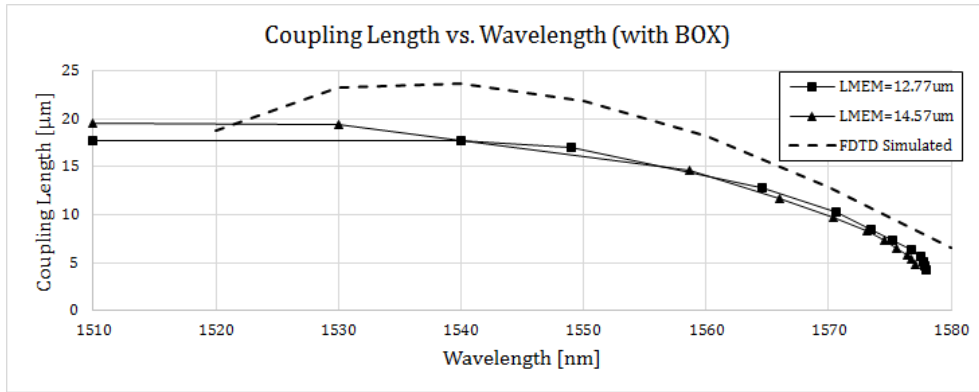


Figure 5.5: Plots of the observed coupling lengths for Tables 5.1 and 5.2. The coupling lengths as predicted by FDTD simulation are included for the same air gap width of 200nm.

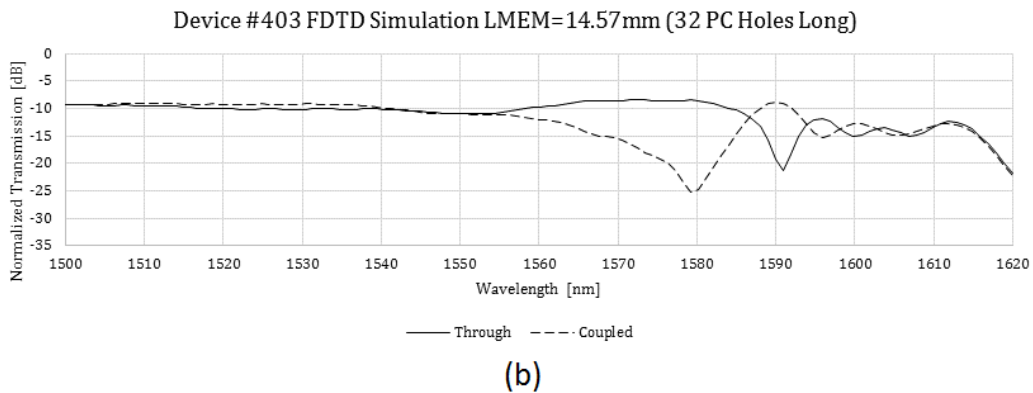
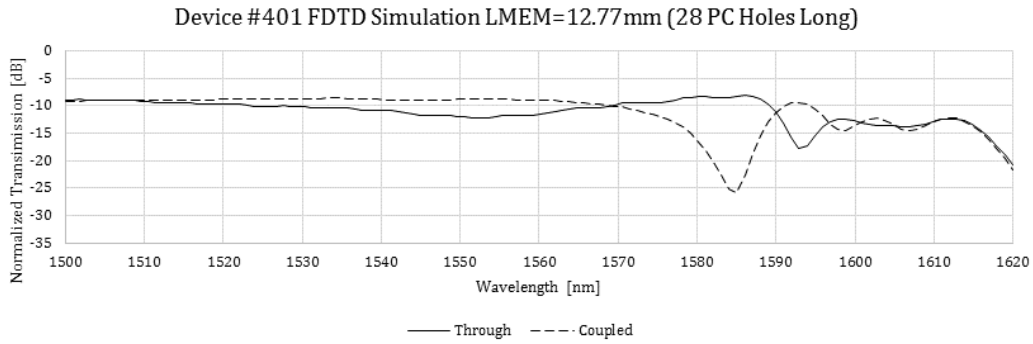


Figure 5.6: The FDTD simulation of the normalized transmission of PCDC devices of length (a) $12.77\mu\text{m}$ and (b) $14.57\mu\text{m}$ are shown. Although a 20nm wavelength deviation is observed with respect to the measured spectrum, the shape and loss agree.

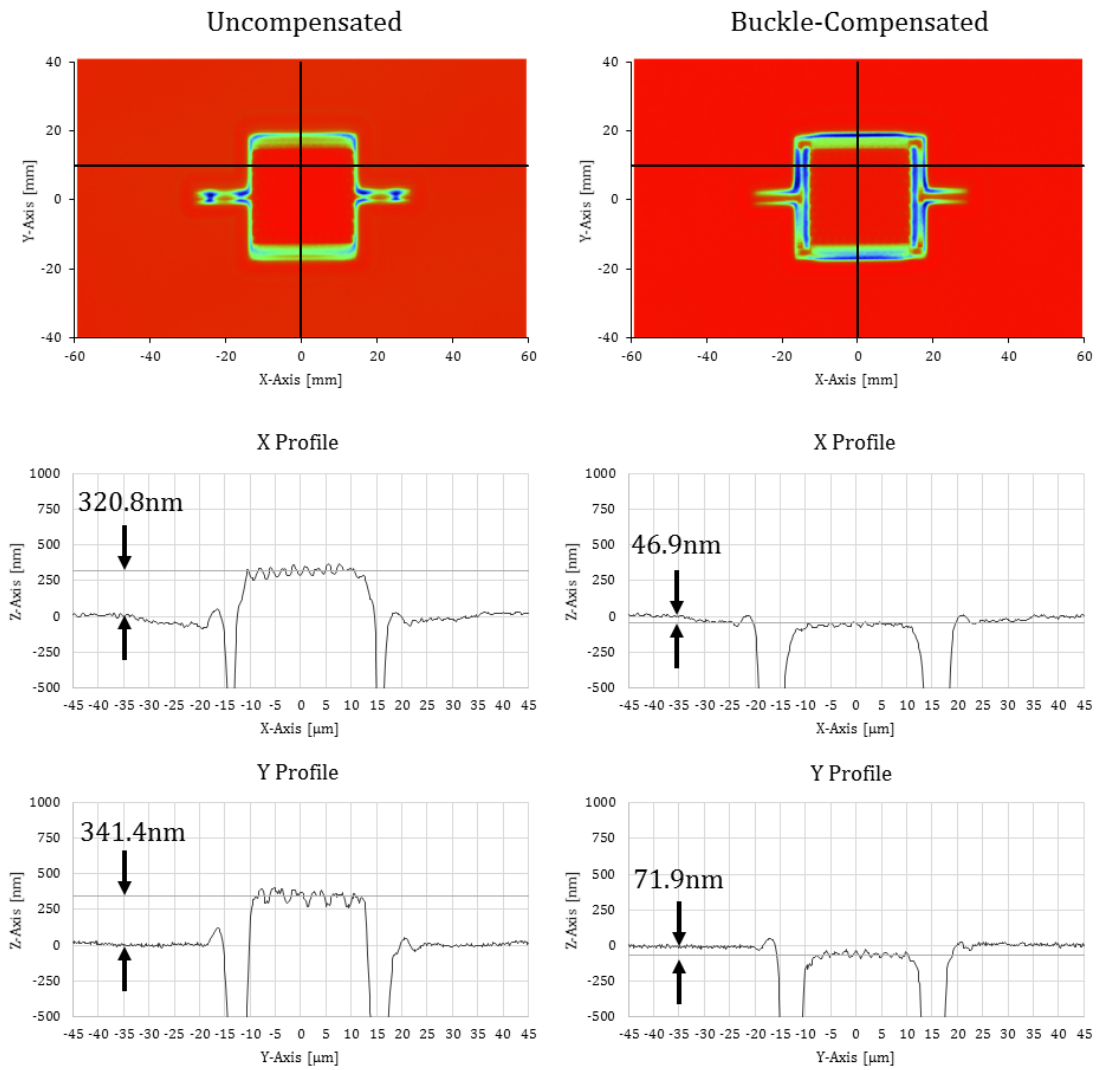


Figure 5.7: Summary of the optical profilometry results. A comparison of the compensated and uncompensated structures demonstrates significant reduction in buckling.

Chapter 6

Closing Remarks and Conclusion

6.1 Summary

The limitations of current mechanical transduction methods have been clearly outlined. Piezoresistive sensors, while inexpensive, suffer from sensor-loading, thermal, and material restrictions. Capacitive-based MEMS sensors suffer from poor linearity, area constraints, contamination and stiction issues. Fabry Perot-based optical sensors, while achieving excellent sensitivity and dynamic range, are plagued with high overhead costs associated with spectral interrogating instrumentation. The optomechanical sensor presented here, based on the photonic crystal directional coupler (PCDC), attempts to overcome these key shortcomings while maintaining high sensitivity, channel fidelity, and CMOS compatibility.

A mathematical framework explaining the operating principles of the PCDC using symmetry and Maxwell's equations was presented. The key concept is the photonic band gap, which allows light to be confined near adjacent PC slab edges and form the directional coupler. This is in contrast to traditional rib or channel waveguides which strictly use total internal reflection to guide light.

A general procedure for designing and modeling PCDC sensors was provided using a combination of plane wave expansion, finite difference time domain, and finite element numerical techniques. A thirteen-fold decrease in coupler-length was demonstrated for the PCDC against a similar directional coupler composed of basic rib waveguides. Numerical simulation indicates excellent sensitivities (0.05–0.15%FS/nm) might be achieved even for extremely small designs, as small as $6.5 \times 6.5 \mu\text{m}$. The minimum sensing areas of the PCDC sensor are about a 100 fold improvement on existing capacitive MEMS and piezoresistive based transduction methods (see Table 1.2). The mechanical design of the PCDC sensor considered the compressive stress that resides in the top silicon layer of SOI that tends to buckle the membrane after under-etching.

Successful fabrication of first generation PCDC sensors was outsourced to the ePIX-fab. Although the buckle-mitigated structures were created at UWO Nanofab using e-beam nanopat-

tering, the fabrication tolerances remain CMOS compatible. Hydrofluoric (HF) acid wet under-etching followed by critical point drying demonstrated PCDC membranes can be released while maintaining their integrity. SEM imaging of structural features confirmed the desired PCDC specifications.

The transmission spectra from the PCDC devices with both output ports accessible validated the principle of operation of the device (with the BOX layer). The validation of buckle-mitigated structures was demonstrated using optical profilometry. The importance of buckling mitigation cannot be overstated and is extremely important from the PCDC perspective. As a highly sensitive, edge-based system, it is crucial that the adjacent edges of the PC coupler lie in a predictable resting point.

6.2 Configurations and Applications

6.2.1 Packaging

Differential sensing using both coupler output ports might enable signal normalization and double the sensitivity. It should be stressed, however, that the high sensitivities quoted here are before packaging considerations. Aside from surface grating couplers, other methods exist which can couple light into the silicon chip which include focused edge-facet coupling [92], and more advanced laser-diode bonded ASIC formats [93]. In spite of this, silicon photonic packaging is an ongoing challenge and there is yet to be a standardized interfacing format. However, the benefits of maintaining an optical format include, large bandwidth, long sensor/receiver distance without amplification distances, EM interference immunity.

6.2.2 Pressure Sensors

As a pressure sensor, the sensor described in Table 3.1 with a membrane width of $L_w = 6.54\mu\text{m}$ PCDC sensors has a full scale of $100\%/S = 149\text{kPa}$ making it well suited for microfluidic applications described in Ref. [24] which was had a full range of 200kPa. A cost effective packaging is suggested for generic pressure sensor, shown in Fig. 6.1, which features a flip-bonding stage. The top surface might be polished in order to tune the device mechanical sensitivity before dicing, however a quantitative investigation is needed to explore the effect of flip-bonding and polishing on the sensitivity and resonance of the PCDC membrane.

6.2.3 Detector Integration

In spite of the all optical format offered by the PCDC, photodetectors can be placed on-chip in order to reduce packaging costs. Leveraging active research in high speed Si-photonic modulators and interchip optical connections can currently offer 1-100GHz bandwidths using CMOS

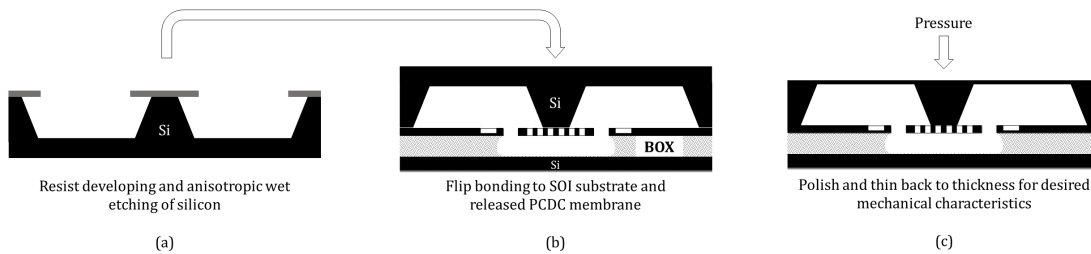


Figure 6.1: By flip bonding an etched wafer to the PCDC device and substrate, a sealed cavity may be formed.

compatible technology. Metal-semiconductor-metal photodiode [94] and evanescently coupled [95, 96] formats have been demonstrated. IBM researchers have successfully fabricated metal-semiconductor-metal Ge-based photodiodes within silicon photonic waveguides on SOI wafers¹ with a 0.41A/W responsivity at 1.31 μ m with 1V bias using an array of cylindrical electrodes implanted within the active layer [97, 98]. Due to stable coupling lengths across a broad band, LED illumination sources might also be integrated and detection onto a singular device.

6.2.4 Dynamic Range and Noise

The dynamic range is largely dependent on the detecting instrument configuration such as sampling rate and power range sampling rate of instrumentation. The dynamic range of the PCDC sensors can be quite high² when compared to existing systems. A detailed and recent analysis of noise generated inside silicon photonics devices is contained in Ref. [99]. Primary sources of noise for PCDC include shot noise in addition to two-photon absorption that leads to free carrier absorption (FCA). The shot noise is due to the discreteness of photon arrivals whose correlation function is given in terms of the expected intensity $\langle I \rangle$

$$\langle \Delta I_{shot}^2 \rangle = \langle I \rangle \frac{hf}{A_{eff}T} \quad (6.1)$$

where f is the optical frequency, h is Plank's constant, T is the data symbol period, and A_{eff} is the effective cross-sectional area of the waveguide.

If the characteristic absorption length is much longer than the length of the waveguide, the FCA noise correlation function can be approximated by the square of the expected intensity $\langle I(x) \rangle^2$

$$\langle \Delta I^2(x) \rangle \cong \frac{\sigma_{FCA}}{A_{eff}} \langle I(x) \rangle^2 \quad (6.2)$$

¹In fact, the same SOI wafers used in this thesis

²0.00008% FS (60dBm) can be achieved with based on N7744 10dBm power meter range 1ms sampling time

where $\sigma_{FCA} \cong 10^{-9} \mu\text{m}^2$ is the FCA cross-section for silicon. FCA noise overtakes the shot noise places an the upper limit on the power entering the silicon photonic chip.

$$P_{thresh} = \frac{hc}{T\lambda} \frac{A_{eff}}{\sigma_{FCA}} \quad (6.3)$$

where c is the speed of light. For a freespace wavelength 1550nm and $A_{eff} = 0.1188 \mu\text{m}^2$, the threshold power is about 150mW for a 10GHz sampling rate. The threshold power can be much lower, however, depending on the modulation scheme as carrier lifetimes can lead to intersymbol interference. These noise considerations are particularly important for WDM systems potentially used for large sensing arrays.

6.3 Future Work

6.3.1 *In situ* Measurement of the PCDC Sensor

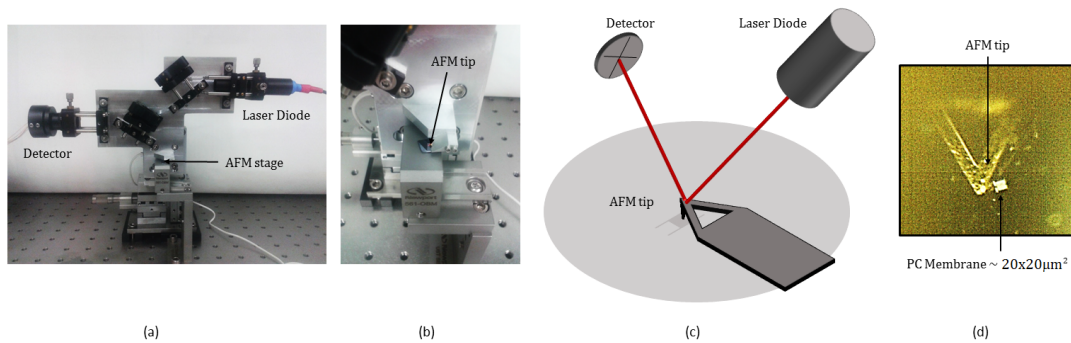


Figure 6.2: (a) Overall picture of current AFM apparatus. The focused light from the laser is reflected on to the AFM tip using tunable mirrors. (b) Close up view of a sample chip loaded onto the AFM stage tip. The AFM tip is very small and can only be seen on under microscope as shown in (c) where it is ready to exert a force on a PC membrane measuring approximately $20 \times 20 \mu\text{m}^2$.

The HF release of the IMEC fabricated PCDC membranes and full optomechanical testing is yet to be completed. This is due to unexpected delays in procuring the SiPh-MIP instrumentation and fabricating the critical point drying chip holder. It is imagined that the sensitivity of the PCDC sensor is enough to detect displacements prescribed by the tip of an atomic force microscopy (AFM) apparatus. By knowing the spring constant of the AFM tip, the mechanical sensitivity of the membrane can be evaluated. Fig. 6.2 shows our current stand-alone AFM apparatus which is yet to be integrated with the current silicon photonic microsystems integration platform (SiPh-MIP) in order to apply the minute force needed to characterize the PCDC membrane.

6.4 Conclusion

While packaging and instrumentation costs remain the key issues with photonic systems, market pressure for improved sensor performance is gradually allowing optical-based systems a market share. The CMOS compatible fabrication of the PCDC sensors is intended to help reduce these costs and should not be understated. Additionally, as industries look toward photonic integration solutions as a means to addressing Von Neumann bottlenecks, photonic sensors might be able to leverage these integration platforms.

A new edge-based mechanical sensing mechanism using a photonic crystal directional coupler fabricated on SOI has been presented. The preliminary measurements taken of the PCDC membranes (with the BOX layer) strongly suggest the primary claims of this thesis are valid: coupling due to split line PC defect, and relaxing SOI strain which led to unpredictable buckling. Despite the packaging related drawbacks, the potential benefits PCDC sensors cannot be overlooked: extremely small, highly sensitive, fast, parallelizable, versatile, CMOS friendly, and immune to EM radiation. For these reasons, PCDC sensors might prove to be an important technology in future.

Bibliography

- [1] Pressure sensor market (2012-2017) - global forecast, trend & analysis - segmentation by technology [piezoresistive, capacitive, electromagnetic (reluctance), resonant solid state, optical], applications [process and nonprocess] and geography. Markets and Markets, 2012.
- [2] R. J. Baker. *CMOS Circuit Design, Layout, and Simulation*. IEEE Press Series on Microelectronic Systems. Wiley, 3rd edition, 2010.
- [3] T.-R. Hsu. *MEMS and Microsystems: Design, Manufacture, and Nanoscale Engineering*, chapter Chapter 7: Materials for MEMS and Microsystems. Wiley, 2 edition, 2008.
- [4] M. J. Madau. *Fundamentals of Microfabrication: The Science of Miniaturization*. CRC Press, 2nd edition.
- [5] W. P. Eaton and J. H. Smith. Micromachined pressure sensors: review and recent developments. *Smart Materials and Structures*, 6:530–539, 1997.
- [6] Pressure sensors market - global industry analysis, size, share, growth, trends and forecast, 2014 - 2020. Transparency Market Research, 2014.
- [7] O. reg. 361/98: Motor vehicles. Environmental Protection Act, 1990. R.S.O., c. E.19.
- [8] The clean air act - highlight of the 1990 amendments. WEB: http://www.epa.gov/sites/production/files/2015-11/documents/the_clean_air_act_-_highlights_of_the_1990_amendments.pdf, 2015.
- [9] Emission standards - european union - cars and light trucks. WEB: <https://www.dieselnets.com/standards/eu/ld.php#intro>, 2015.
- [10] R. Isermann. *Engine Modeling and Control: Modeling and Electronic Management of Internal Combustion Engines*. Springer, 2014.
- [11] I. E. Araci, B. Su, S. R. Quake, and Y. Mandel. An implantable microfluidic device for self-monitoring of intraocular pressure. *Nature Medicine*, 20(9):1074–1079, 2014.

- [12] R. L. Hammond, K. Hanna, C. Morgan, P. Perakis, N. Najafi, G. W. Long, and C. J. Shanley. A wireless and battery-less miniature intracardiac pressure sensor: Early implantation studies. *ASAIO Journal*, 58:83–87, 2012.
- [13] K. Fricke. Wireless telemetry system for implantable sensors. Master’s thesis, University of Western Ontario, 2012.
- [14] M. Yip, R. Jin, H. Nakajima, K. M. Stankovic, and A. P. Chandrakasan. A fully-implantable cochlear implant soc with piezoelectric middle-ear sensor and arbitrary waveform neural stimulation. *IEEE Journal of Solid-State Circuits*, 50(1):214–229, 2015.
- [15] J. Coosemans and R. Puers. An autonomous bladder pressure monitor. *Sensors and Actuators A*, 123-124:155–161, 2005.
- [16] Minghua Xu and Lihong V. Wang. Analytic explanation of spatial resolution related to bandwidth and detector aperture size in thermoacoustic or photoacoustic reconstruction. *Physics Review E*, 67:056605, May 2003.
- [17] Minghua Xu and Lihong V. Wang. Photoacoustic imaging in biomedicine. *Review of Scientific Instruments*, 77(4), 2006.
- [18] H. Jiang. *Photoacoustic Tomography*, chapter Chapter 4: Transducer Array-Based Photoacoustic Tomography: 2D, 3D, and 4D Photoacoustic Imaging. CRC Press, 2014.
- [19] M. Xu and L. V. Wang. Photoacoustic imaging in biomedicine. *Review of Scientific Instruments*, 77, 2006.
- [20] B. Wang, J. L. Su, A. B. Karpiouk, K. V. Sokolov, R. W. Smalling, and S. Y. Emelianov. Intravascular photoacoustic imaging. *IEEE Journal of Selected Topics in Quantum Electronics*, 16(3):588–599, 2010.
- [21] Lihong V. Wang. Prospects of photoacoustic tomography. *Medical Physics*, 35(5758), 2008.
- [22] S. Manohar, S. E. Vaartjes, J. C. G. van Hespén, J. M. Klaase, F. M. van den Engh, W. Steenbergen, and T. G. van Leeuwen. Initial results of in vivo non-invasive cancer imaging in the human breast using near-infrared photoacoustics. *Optics Express*, 15(9):12277–12285, 2007.
- [23] Li. R, P. Wang, L. Lan, P. Lloyd, C. J. Goergen, S. Chen, and J.-X. Cheng. Assessing breast tumor margin by multispectral photoacoustic tomography. *Biomedical Optics Express*, 6(4):1273–1281, 2015.

- [24] A. Shakir, K. Sirihar, B. Murcko, C. Yun, and B. Sulouff. Flow sensor using micromachined pressure sensor. *IEEE Sensors*, 6:530–539, 2008.
- [25] R. E. Oosterbroek, T. S. J. Lammerink, J. W. Berenschot, G. J. M. Krijnen, M. C. Elwenspoek, and A. van den Berg. A micromachined pressure/flow-sensor. *Sensors and Actuators*, 7:167–177, 1999.
- [26] H. Li, C. X. Luo, H. Ji, Q. Ouyang, and Y. Chen. Micro-pressure sensor made of conductive pdms for microfluidic applications. *Microelectronic Engineering*, 87:1266–1269, 2010.
- [27] X. Zhang, P. Coupland, P. D. I. Fletcher, and S. J. Haswell. Monitoring of liquid flow through microtubes using a micropressure sensor. *Chemical Engineering Research and Design*, 87:19–24, 2009.
- [28] G. Testa, G. Persichetti, and Bernini R. Optofluidic approaches for enhanced microsensor performance. *Sensors*, 15:465–484, 2015.
- [29] M. G. Scullion, T. F. Krauss, and A. Di Falco. Slotted photonic crystal sensors. *Sensors*, 13:3675–3710, 2013.
- [30] S. Liu, W. Gao, H. Li, Y. Dong, and H. Zhang. Liquid-filled simplified hollow-core photonic crystal fiber. *Optics & Laser Technology*, 64:140–144, 2014.
- [31] H. Helvajian, editor. *Microengineering Aerospace Systems*. The Aerospace Press, 1999.
- [32] D. Agnelidis and P. Parsons. Optical micromachined pressure sensor for aerospace applications. *Optical Engineering*, 31(8):1638–1642, 1992.
- [33] H. H. Hu and H. H. Bau. Feedback control to delay or advance linear loss of stability in planar poiseuille flow. In *Proceedings: Mathematical and Physical Sciences*, volume 447, pages 299–312. The Royal Society, 1994.
- [34] R. H. Thomas, M. M. Choudhari, and R. D. Joslin. Flow and noise control: Review and assessment of future directions. Technical report, NASA, 2002.
- [35] M. J. Madou. *Fundamentals of Microfabrication*. CRC Press, 3 edition, 2012.
- [36] W. N. Jr. Sharpe. *The MEMS Handbook: MEMS: Introduction and Fundamentals*, chapter Chapter 3: Mechanical Properties of MEMS. CRC Press: Taylor & Francis Group, 2006.
- [37] A. J. Jacobs-Cook. Mems versus moms from a systems point of view. *Journal of Micromechanics and Microengineering*, 6:148–156, 1996.

- [38] Y. Zhang, R. Howver, B. Gogoi, and N. Yazdi. A high-sensitive ultra-thin mems capacitive pressure sensor. In *Solid-State, Actuators and Microsystems Conference (TRANSDUCERS), 2011 16th International*, pages 112–115, Beijing, 2011. IEEE.
- [39] H.-Y. Yu, M. Qin, J.-Q. Huang, and Q.-A. Huang. A mems capacitive pressure sensor compatible with cmos process. In *Sensors, 2012 IEEE*, pages 1–4, Taipei, 2012. IEEE.
- [40] Y. He, J. Liu, L. Li, and J. He. A novel capacitive pressure sensor and interface circuitry. *Microsystems Technology*, 19:25–30, 2013.
- [41] M. Nie, Q.-A. Huang, M. Qin, and W.-H. Li. Complementary metal-oxide semiconductor compatible capacitive barometric pressure sensor. *Journal of Micro/Nanolithography, MEMS and MOEMS*, 10(1), 2011.
- [42] C.-T. Sun, Y.-C Lin, C.-J Hsieh, J.-C Liou, L.-B. Wang, and W.-C Tian. A linear-response cmos-mems capacitive tactile sensor. In *Sensors, 2012 IEEE*, pages 1–4, Taipei, 2012. IEEE.
- [43] A. Nisanth, K. J. Suja, and R. Komaragiri. Performance analysis of a silicon peizoresistive pressure sensor based on diaphragm geometry and piezoresistor dimensions. In *Circuit, Power and Computing Technologies (ICCPCT), 2014 International Conference on*, pages 1273–1278, Nagercoil, 2012. IEEE.
- [44] C. Pramanik and H. Saha. Low pressure piezoresistive sensors for medical electronics applications. *Materials and Manufacturing Processes*, 21:233–238, 2006.
- [45] STMicroelectronics, United Kingdom. *LPS331AP high-resolution MEMS pressure sensor*, September 2012.
- [46] Y. Zhao, X. Fang, Z. Jiang, and L. Zhao. An ultra-high pressure sensor based on soi piezoresistive material. *Journal of Mechanical Science and Technology*, 8:1655–1660, 2010.
- [47] S. S. Kumar and B. D. Pant. Design principles and considerations for the 'ideal' silicon piezoresistive pressure sensor: a focused review. *Microsystem Technology*, 20:1213–1247, 2014.
- [48] G. C. Hill, R. Melamud, F. E. Declercq, A. A Davenport, I. H. Chan, P. G. Hartwell, and B. L. Pruitt. Su-8 mems fabry-perot pressure sensor. *Sensors and Actuators A*, 138:52–62, 2007.
- [49] N. H. Ngajikin, L. Y. Ling, N. I. Ismail, A. S. M. Supaat, M. H. Ibrahim, and N. M. Kasim. Cmos-mems integration in micro fabry perot pressure sensor. *Jurnal Teknologi*, 6(3), 2014.

- [50] S. Chen and L. Zhang. Miniature fabry-perot optical fiber pressure sensor. In *Design, Manufacturing, and Testing of Micro- and Nano-Optical Devices and Systems*, Proc. SPIE 7657, 5th International Symposium on Advanced Optical Manufacturing and Testing Technologies, 2010.
- [51] P. Roriz, M. S. Ferreira, K. Schuster, J. Kobelke, and O. Frazao. A fabry-perot sensor prototype for low-pressure measurements. *Microwave and Optical Technology Letters*, 56(12):2981–2984, 2014.
- [52] Y. Zhang, L. Yuan, L. Xinwei, A. Kaur, J. Huang, and H. Xiao. High-temperature fiber-optic fabry-perot interferometric pressure sensor fabricated by femtosecond laser. *Optics Letters*, 38(22), 2013.
- [53] Y. Zhu, K. L. Cooper, G. R. Pickrell, and A. Wang. High-temperature fiber-tip pressure sensor. *Optics Letters*, 24(2):861–896, 2006.
- [54] A. A. Barlian, W.-T. Park, J. R. Mallon, A. J. Rastegar, and B. L. Pruitt. Review: Semiconductor piezoresistance for microsystems. In *Proc IEEE Institute of Electrical and Electronics Engineering*, volume 97, pages 513–522, 2009.
- [55] S. S. Kumar and B. D. Pant. Design principles and considerations for the 'ideal' silicon piezoresistive pressure sensor: a focused review. *Microsystems Technologies*, 20:1213–1247, 2014.
- [56] Z. Niu, Y. Zhao, and B. Tian. Design optimization of high pressure and high temperature piezoresistive pressure sensor for high sensitivity. *Review of Scientific Instruments*, 85(015001), 2014.
- [57] A. Rinaldi, A. Proietti, A. Tamburrano, G. De Bellis, M. Mulattieri, and M.S. Sarto. Multilayer graphene-based films for strain sensing. In *Nanotechnology (IEEE-NANO), 2014 IEEE 14th International Conference on*, pages 585–589, 2014.
- [58] M. Schulz, Y. Song, A Hehr, and V. Shanov. Embedded carbon nanotube thread piezoresistive strain sensor performance. *Sensor Review*, 34(2):209–219, 2014.
- [59] E. Almaz and T. E. Blue. Effects of annealing on irradiated sic piezoresistive pressure sensor. *Journal of the Korean Physical Society*, 61(7):1005–1009, 2012.
- [60] P. V. Rao, K. Srimannarayana, M. S. Shankar, P. Kishore, D. Sengupta, and P. S. Reddy. A diaphragm based low-cost fiber optic pressure sensor. *Microwave and Optical Letters*, 54(10):2229–2231, 2011.

- [61] E. Pinet. Pressure measurement with fiber-optic sensors: Commercial technologies and applications. In W. J. Bock, J. Alber, and X. Bao, editors, *21st International Conference on Optical Fiber Sensors*, volume 7753. SPIE, 2011.
- [62] V. R. Pachava, S. Kamineni, S. S. Madhuvarasu, and K. Putha. A high sensitive fbg pressure sensor using thin metal diaphragm. *Journal of Optics*, 43(2):117–121, 2014.
- [63] X. Zhao, J. M. Tsai, H. Cai, X. M. Ji, J. Zhou, M. H. Bao, Y. P. Huang, D. L. Kwong, and A. O. Liu. A nano-opto-mechanical pressure sensor via ring resonator. *Optics Express*, 20(8):8535–8542, 2012.
- [64] P. Niewczas, L. Dzuida, G. Fusiek, A. J. Willshire, J. R. McDonald, G. Thursby, D. Harvey, and W. C. Michie. Interrogation of extrinsic fabry-perot interferometric sensors using arrayed waveguide grating devices. *IEEE Transactions on Instrumentation and Measurement*, 52(4):1092–1096, 2003.
- [65] A. Bakhtazad and J. Sabarinathan. Silicon planar photonic crystal directional coupler as a displacement sensing element. In *Proceedings of the SPIE*, volume 8007 of *Photonics North*, 2011.
- [66] Y. Wang, A. Bakhtazad, and J. Sabarinathan. Reflection mode 2-dimensional photonic slab waveguide based micro-pressure sensor. In *Proceedings of the SPIE*, volume 8007 of *Photonics North*, 2011.
- [67] J. Sabarinathan, A. Bakhtazad, X. Hou, and J. Hutter. Photonic crystal pressure sensors. US Patent, 2014. 8839683 B2.
- [68] J. Sabarinathan, A. Bakhtazad, Poulsen B., and M. Zylstra. Photonic crystal thin-film micro-pressure sensors. *Journal of Physics*, 60(8):5751–5758.
- [69] A. Bakhtazad, J. Sabarinathan, and J. Hutter. Mechanical sensitivity enhancement of silicon based photonic crystal micro-pressure sensor. International Symposium on Optomechatronic Technologies (ISOT), 2010.
- [70] Y. Tanaka, H. Nakamura, Y. Sugimoto, N. Ikeda, K. Asakawa, and K. Inoue. Coupling properties in a 2-d photonic crystal slab directional coupler with a triangular lattice of air holes. *IEE Journal of Quantum Electronics*, 41(1):76–84, 2005.
- [71] Y. Sugimoto, Y. Tanaka, N. Ikeda, T. Yang, H. Nakamura, K. Asakawa, K. Inoue, T. Maruyama, K. Miyashita, and K. Ishida. Design, fabrication, and characterization of coupling-strength-controlled directional coupler based on two-dimensional photonic-crystal slab waveguides. *Applied Physics Letters*, 83(16):3236–3238, 2003.

- [72] S. Dakshinamurthy, N. R. Quick, and A. Kar. Temperature-dependent optical properties of silicon carbide for wireless temperature sensors. *Journal of Physics D: Applied Physics*, 40:353–360, 2007.
- [73] H. H. Li. Refractive index of silicon and germanium and its wavelength and temperature derivatives. *Journal of Physical Chemistry Reference Data*, 9(3):561–658, 1980.
- [74] R. Halir, A. Maese-NOvo, A. Ortega-Monux, I. Molina-Fernandez, J. G. Wanguemert-Perez, P. Cheben, D.-X. Xu, J. H. Schmid, and S. Janz. Compact broadband directional coupler. In *Group IV Photonics (GFP), 2012 IEEE 9th International Conference on*, pages 177–179, San Diego, CA, 2012. IEEE.
- [75] R. Halir, A. Maese-Novo, A. Ortega-Monux, I. Molina-Fernandez, J. G. Wanguemert-Perez, P. Cheben, D.-X. Xu, J. H. Schmid, and S. Janz. Colorless directional coupler with dispersion engineered sub-wavelength structure. *Optics Express*, 20(12):13470–13477, 2012.
- [76] E. Iwase, P.-C. Hui, D. Woolf, A. W. Rodriguez, S. G. Johnson, F. Capasso, and M. Loncar. Control of buckling in large micromembranes using engineered support structures. *Journal of Micromechanics and Microengineering*, 22, 2012.
- [77] J. D. Joannopoulos, S. G. Johnson, J. N. Winn, and R. D. Meade. *Photonic Crystals: Molding the Flow of Light*. Princeton University Press, 2 edition, 2008.
- [78] D. A. McQuarrie. *Mathematical Methods for Scientists and Engineers*. University Science Books, 2003.
- [79] F. J. Dyson. Why is maxwell’s theory so hard to understand? an essay by Professor Freeman J. Dyson, FRS.
- [80] Bandsolve 9 (manual). RSOFT Design Group, Inc., July 1993-2012.
- [81] S. G. Johnson. Guided modes in photonic crystal slabs. *Physical Review B, Condensed Matter and Material Physics*, 60(8):5751–5758.
- [82] M. Gherbrebrhan, M. Ibanescu, S. G. Johnson, M. Soljagic, and J. D. Joannopoulos. Distinguishing zero-group-velocity modes in photonic crystals. *Physical Review A*, 76, 2007.
- [83] M. Qiu and M. Swillo. Contra-directional coupling between two-dimensional photonic crystal waveguides. *Photonics and Nanostructures Fundamentals and Applications*, 1:23–30, 2003.

- [84] D. Marcuse. *Theory of Dielectric Optical Waveguides*. America Telephone and Telegraph Company, 2 edition, 1991.
- [85] D. Vermeulen, S. Selvaraja, P. Verheyen, G. Lepage, W. Bogaerts, P. Absil, D. Van Thourhout, and G. Roelkens. High-efficiency fiber-to-chip grating couplers realized using an advanced cmos-compatible soi platform. *Optics Express*, 18(17):18278–18283, 2010.
- [86] Toshiyuki Tsuchiya. *Evaluation of Mechanical Properties of MEMS Materials and Their Standardization*, pages 1–25. Wiley-VCH Verlag GmbH & Co. KGaA, 2008.
- [87] COMSOL. *Improving Your Meshing with Swept Meshes*, 2015.
- [88] R. M. Jones. *Buckling of Bars, Plates, and Shells*. Bull Ridge Publishing, 2006.
- [89] COMSOL. *Postbuckling Analysis of a Hinged Cylindrical Shell*, 2015.
- [90] Wet & plasma etching. <http://tnfc.utoronto.ca/home/processes-services/wet-plasma-etching/>, July 2015.
- [91] CMC Microsystems, Kingston, Ontario, Canada. *Products and Services Catalogue 2013*, 2013.
- [92] S. Kopp, C. Bernabe, B. B. Bakir, Fedeli J.-M., R. Orobtcchouk, F. Schrank, H. Porte, L. Zimmermann, and T. Tekin. Silicon photonic circuits: On-cmos intergration fiber optical coupling, and packaging. *IEEE Journal of Selected Topics in Quantum Electronics*, 12(3):498–509, 2011.
- [93] P. De Dobelaere, A. Ayazi, Y Chi, A. Dahl, S. Denton, S. Gloeckner, K.-Y. Hon, S. Hovey, Y. Liang, M. Mack, G. Masini, A. Mekis, M. Peterson, T. Pinguet, J. Schramm, M. Sharp, Sohn C., K. Stechschulte, P. Sun, L. Vastola, L. Verslegers, and R. Zhou. Packaging of silicon photonics systems. *Optical Society of America*, 978-1-55752-993-0/14:1–3, 2014.
- [94] L. Vivien, D. Marris-Morini, J.-M. Fedeli, M. Rouviere, J.-F. Damlencourt, L. El Melhaoui, X. Le Roux, P. Crozat, J. Mangeney, E. Cassan, and S. Laval. Metal-semiconductor-metal ge photodetectors integrated in silicon waveguides. *Applied Physics Letters*, 92(15114):1–3, 2008.
- [95] T. Yin, R. Cohen, M. M. Morse, G. Sarid, Y. Chetrit, D. Rubin, and M. J. Paniccia. 31ghz ge n-i-p waveguide photodetectors on silicon-on-insulator substrate. *Optics Express*, 15(21):12965–13971, 2007.

- [96] D. Ahn, L. C. Kimerling, and J. Michel. Efficient evanescent wave coupling conditions for waveguide-integrated thin-film si/ge photodetectors on silicon-on-insulator/germanium-on-insulator substrates. *Journal of Applied Physics*, 110(083115):1–9, 2011.
- [97] S. Assefa, F. Xia, S. W. Bedell, Y. Zhang, T. Topuria, P. M. Rice, and Y. A. Vlasov. Cmos-integrated high-speed msm germanium waveguide photodetector. *Optics Express*, 18(5):4986–4999, 2010.
- [98] S. Assefa, F. Xia, M. J. Green, C. L. Schow, A. V. Rylyakov, and Y. A. Vlasov. Cmos-integrated optical receivers for on-chip interconnects. *IEEE Journal of Selected Topics in Quantum Electronics*, 16(5):1376–1385, 2010.
- [99] D. Dimitropoulos and B. Jalali. Noise and information capacity in silicon nanophotonics. *IEEE Photonics Journal*, 7(3):1–21, 2015.
- [100] Kane Yee. Numerical solution of initial boundary value problems involving maxwell’s equations in isotropic media. *IEEE Transactions on Antennas and Propagation*, 14(3):302–307, 1966.
- [101] U. S. Inan and R. A. Marshall. *Numerical Electromagnetics: The FDTD Method*. Cambridge University Press, 2011.
- [102] F. H. Drosaert and A. Giannopoulos. Complex frequency shifted convolution pml for fdtd modelling of elastic waves. *Wave Motion*, 44:593–604, 2007.
- [103] S. D. Gedney and B. Zhao. Auxiliary differential equation formulation for the complex-frequency shifted pml. *IEEE Transactions on Antennas and Propagation*, 53(3):838–847, 2010.

Appendix A

Finite-Difference Time-Domain

Finite-difference time-domain (FDTD) is a robust EM simulation which involves the literal time-stepping of Maxwell's equations in a discretized space. The FDTD implementation allows finite structures and absorption to easily be incorporated in the routine. The stability of the FDTD algorithm resides in the use of the lattice developed by in 1966 by Kane Yee [100] as shown in Fig. A.1.

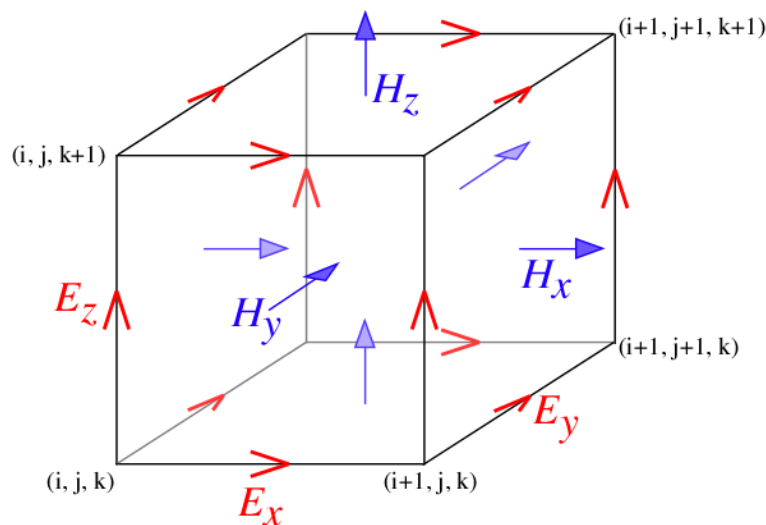


Figure A.1: A Yee lattice, used almost universally in FDTD routines, provides a natural arena for computing curls and line integrals

The \mathbf{E} and \mathbf{H} fields in the Yee lattice must be offset in order to ensure the fields remain divergenceless throughout the time-stepping [101]. By computing both fields in this manner, only the first derivatives are required¹ and only closest-neighbour fields are needed for the next iteration. For most accurate results, the fields at neighbouring points should not vary significantly in space and the discretization of space is usually $1/5$ – $1/10$ of the estimated wavelength

¹Or, line integrals

in the media. Similarly, the unit-time step cannot be made arbitrarily large. In Cartesian coordinates, the time discretization must also satisfy the Courant-Fredric Levy condition given by

$$\Delta t \leq \frac{1}{c_{max} \sqrt{(\Delta x)^{-2} + (\Delta y)^{-2} + (\Delta z)^{-2}}} \quad (\text{A.1})$$

in order for the remain convergent. Specialized FDTD routines can be extended to any number of dimensions incorporating curvilinear coordinate systems by using the appropriate Maxwell's equations and Yee lattice.

The effect of loss on the coupling may be confirmed as FDTD simulations agree with PWE by modeling the silicon with a purely real dielectric constant. In order to introduce loss, a Lorentz oscillator model is inserted into the harmonic domain of Maxwell's equations which is data-fitted to the observed optical response of silicon. The dielectric representation of the Lorentz model is given by

$$\epsilon(\omega) = \epsilon + \frac{\epsilon_{Lorentz} \omega_0^2}{\omega_0^2 - 2i\delta_0 \omega - \omega^2} \quad (\text{A.2})$$

where the permittivity, Lorentz permittivity, Lorentz resonance, and line width for silicon are given by $\epsilon = 7.987$, $\epsilon_{Lorentz} = 3.688$, $\omega_0 = 3.933 \times 10^{15}$ rad/s, and $\delta_0 = 10^{-8}$, respectively.

In most cases, the ideal boundary conditions of the FDTD algorithm would totally absorb all incident radiation as reflections can generate unwanted Fabry-Perot effects. A perfectly matched layer (PML) is used to minimize these reflections by modifying Maxwell's equations inside a shell of lattice points surrounding the domain. PMLs are typically implemented using complex frequency shifting (CFS) achieved by artificially introducing a complex coordinate transformation to the harmonic Maxwell's equations. The introduction of the complex term effectively converts propagating waves to evanescent waves. For waves travelling in the x -direction this can be achieved by replacing partial derivatives of x with

$$\frac{\partial}{\partial x} \rightarrow \frac{1}{\kappa + \frac{\sigma}{\alpha + i\omega}} \frac{\partial}{\partial x} \quad (\text{A.3})$$

where κ , σ , and a are real positive constants [102, 103]. The PML-adjusted Maxwell's equations are then transformed to the time domain using the inverse Fourier transform. The resulting equations are frequently called the auxillary differential equations. The purpose of α is to shift frequency which allow for low-frequency numerical stability while σ controls the decay rate of PML absorption. Increasing the κ parameter generates more reflections at the PML normal but reduces reflections at oblique angles. These parameters are smoothed out over several lattice layers using polynomial approximation. Care must be taken to when using PML in metals and non-homogeneous structures, particularly photonic crystals, as exponentially decaying waves become propagating waves using the prescribed CFS transformation.

The typical FDTD routine consists of an excitation and a monitor. Excitations frequently consist of a Gaussian pulse centred on the desired frequency². FDTD allows for a variety of excitation sources such as plane-wave, dipole, Gaussian, and pre-computed modal solutions. Monitors are used to record the field amplitude at each time-step which may 1D or 2D. A Fourier transform is used to convert the time-domain excitation and monitor fields to harmonic-domain in order to evaluate the transmission spectra. The simulation may be concluded either after a fixed amount of time or when the total electromagnetic energy contained in the domain falls below a pre-determined threshold.

²A Gaussian pulse is used as it is maximally localized in both the harmonic and time domain

Appendix B

Plane Wave Expansion

While the Bloch theorem provides insight on the possible range of unique propagation constants, the modal solutions $\mathbf{u}_{\mathbf{k}}$ and frequency ω involving the specific dielectric configuration remain unknown. The plane wave expansion method (PWE) seeks to find solutions to the eigenvalue problem posed by the vector Helmholtz equation for given a \mathbf{k} . By combining the Bloch theorem with the vector Helmholtz equation, a new operator \mathbf{L} may be created and is given by

$$\mathbf{L}\mathbf{u}_{\mathbf{k}} = (i\mathbf{k} + \nabla) \times \left(\frac{1}{\epsilon(\mathbf{r})} (i\mathbf{k} + \nabla) \right) \times \mathbf{u}_{\mathbf{k}} = \left(\frac{\omega}{c} \right)^2 \quad (\text{B.1})$$

This is the equation that is solved using the PWE routine. There are four important features of the \mathbf{L} operator:

- The \mathbf{L} operator forms an eigenvalue equation with unknown eigenvalue ω and eigenvector $\mathbf{u}_{\mathbf{k}}$
- The \mathbf{k} parameter is incremented freely forming a new eigenvalue equation to be solved for each \mathbf{k}
- The \mathbf{L} operator is completely scalable, typically ω and \mathbf{k} are normalized to the lattice parameter
- The \mathbf{L} operator is Hermitian and therefore has real positive-definite discrete eigenvalues

The parameterization of the \mathbf{k} and solving for ω is in contrast to the prevailing wisdom of sweeping ω and solving for \mathbf{k} as excitations are typically centred near a specific harmonic. However, framing the problem in this manner allows direct exploitation of the periodic symmetry inherent in the system. Since PWE is based on a Fourier spatial domain, it is important to keep in mind that the domain can be imagined as a "tile" which is repeated in all three dimensions. Care must be taken to ensure no discontinuities exist as these subdomains are stitched together. Indeed, when simulating defects, the domain must be extended accordingly to ensure

sufficient spatial separation of neighbouring defects after tiling. Technically, this is achieved by padding the defect with a continuation of the dielectric media along the direction where the symmetry is broken. In the case of dielectric slabs, this may include adding more air-region above/below the slab or adding additional bulk PC periods surrounding the defect.

Since \mathbf{L} is Hermitian, a variational approach may be used to find the lowest order mode. If \mathbf{u}_k and $\frac{1}{\epsilon(\mathbf{r})}$ are expressed as a truncated Fourier series, the unknown Fourier coefficients of \mathbf{u}_k may be solved by minimizing the functional¹ given by

$$F[\mathbf{u}_k] = \frac{\int \mathbf{u}_k * [\mathbf{L}\mathbf{u}_k]}{\mathbf{u}_k \mathbf{u}_k} \quad (\text{B.2})$$

The functional is considered minimized if the difference between successive iterations is below a specified error tolerance. Higher order modes are computed by also imposing modal orthogonality. All of the band structure plots computed in this thesis were calculated using PWE.

¹using the Ritz method

Appendix C

FDTD Script (Lumerical)

```
# PCDC Lumerical Script by Michael Zylstra
# Creates a basic PCDC structure with adjustable
clear;
deleteall;
Lambda=450e-9; # Lambda (PC pitch)
T=220e-9; # T (PC slab thickness)
R=0.3*Lambda; # R (PC hole radius)
W=200e-9; # W (Air gap)
E=1.2*Lambda; # E (Edge width)
D=0e-9; # D (Sensor deflection)
Ny=53; # Ny (Number of PC holes along coupling length)
Nx=3; # Nx (Number of PC periods in each side)
clad=1e-6; # clad (Width of rib waveguide cladding)
simtime=1200e-15; # FDTD simulation time
wavelength=1550e-9; # Center wavelength
fddt.wavelength_min=1.400e-6;
fddt.wavelength_max=1.700e-6; # fddt.wavelength_min/max (Sets the
max/min wavelength of Gaussian pulse)
extension=3e-6;
hole2clad=1e-9;
T_ridge=50e-9;
newproject;
filename= "PCDC";
save(filename);
materials; # runs "material" script which creates a dispersive ma-
terial model for Si.
Material_Si = "Si (Silicon) - Dispersive & Lossless";
```

```

MESH = 3;
FREQ_PTS = 128; # Number of FFT points
FDTD_above=500e-9; # Extra simulation volume added, 0.5 um on top
and bottom
FDTD_below=500e-9;
BC = "PML"; # boundary conditions
Autoshutoff=1e-5;
setglobalsource("center frequency",c/wavelength);
setglobalsource("frequency span",c/wavelength/8);
MAXZ=T/2+FDTD_above; MINZ=-T/2-FDTD_below;
deleteall;
# *****
# PC COUPLER:
# *****
# Create Si slab
addrect; set("name", "RightSlab");
set("material", Material_Si);
set("override mesh order from material database", true);
set("mesh order", 3);
set("x min", W/2);
set("x max", W/2+E+(Nx+1)*sqrt(3)*Lambda);
set("z", D);
set("z span", T);
set("y min", 0);
set("y max", (Ny+1)*Lambda);
# Create array of air holes
for(ny=0:Ny) {
addcircle;
set("name", "longrow");
set("material", "etch");
set("x", W/2+E);
set("y", (ny+1/2)*Lambda);
set("radius", R);
set("z", D);
set("z span", T);
}
for(ny=1:Ny) {
addcircle;
set("name", "shortrow");

```

```

set ("material", "etch");
set ("x", W/2+E+(1/2)*sqrt(3)*Lambda);
set ("y", ny*Lambda);
set ("radius", R);
set ("z", D);
set ("z span", T);
}
select ("longrow");
shiftselect ("shortrow");
for (nx=1:Nx) {
copy (sqrt(3)*Lambda);
}
# Create Si slab
addrect; set ("name", "LeftSlab");
set ("material", Material_Si);
set ("override mesh order from material database", true);
set ("mesh order", 3);
set ("x max", -W/2);
set ("x min", -(W/2+E+(Nx+1)*sqrt(3)*Lambda));
set ("z", 0);
set ("z span", T);
set ("y min", -extension);
set ("y max", (Ny+1)*Lambda+extension);
# Create array of air holes
select ("longrow");
copy (-W-2*E-(Nx)*sqrt(3)*Lambda, 0, -D);
select ("shortrow");
copy (-W-2*E-(Nx+1)*sqrt(3)*Lambda, 0, -D);
# Create BOX layer
addrect; set ("name", "BOX");
set ("material", "SiO2 (Glass) - Dispersive & Lossless");
set ("x max", (W/2+E+((Nx+1.5)*sqrt(3))*Lambda)+SimMarginX+0.75e-6);
set ("x min", -(W/2+E+((Nx+1.5)*sqrt(3))*Lambda)-SimMarginX-0.75e-6);
set ("z max", -T/2);
set ("z min", MINZ);
set ("y min", -extension-SimMarginY);
set ("y max", extension+(Ny+1)*Lambda+SimMarginY);

```

```

# *****
# WAVEGUIDE FOR COUPLER:
# *****
addrect; set("name", "RightBotWG");
set("material", Material_Si);
set("x min", W/2);
set("x max", W/2+E);
set("z", D);
set("z span", T);
set("y min", -extension);
set("y max", 0);
addrect; set("name", "RightTopWG");
set("material", Material_Si);
set("x min", W/2);
set("x max", W/2+E);
set("z", D);
set("z span", T);
set("y min", (Ny+1)*Lambda);
set("y max", (Ny+1)*Lambda+extension);
addrect; set("name", "LeftBotCLD");
set("material", "etch");
set("x max", -W/2-E);
set("x min", -W/2-E-clad);
set("z min", -40e-9);
set("z max", T/2);
set("y min", -extension);
set("y max", 0);
addrect; set("name", "LeftTopCLD");
set("material", "etch");
set("x max", -W/2-E);
set("x min", -W/2-E-clad);
set("z min", -40e-9);
set("z max", T/2);
set("y min", (Ny+1)*Lambda);
set("y max", (Ny+1)*Lambda+extension);
# *****
# FDTD:
# *****
MonSpanY=2e-6+E;

```

```

SimMarginX=1e-6; #make sure simulation is inside material
SimMarginY=1e-6; #make sure simulation is inside material
SourceMarginX=2.5e-6;
MonMarginX=2e-6;
# add FDTD
addfdtd;
set("x min", -(W/2+E+((Nx+1.5)*sqrt(3))*Lambda)+SimMarginX-0.75e-6);
set("x max", (W/2+E+((Nx+1.5)*sqrt(3))*Lambda)-SimMarginX+0.75e-6);
set("y min", -extension+SimMarginY);
set("y max", extension+(Ny+1)*Lambda-SimMarginY);
set("z min", MINZ);
set("z max", MAXZ);
set("mesh accuracy", MESH);
set("z min bc", BC); set("z max bc", BC); set("y min bc", BC); set("y max bc", BC);
set("auto shutoff min", Autosshutoff);
set("simulation time", simtime);
set("pml reflection", 1e-7);
set("type of pml", "stabilized");
set("auto shutoff min", 0.005);
# adjust mesh to align with materials
addmesh; set("name", "Air Gap Refinement");
set("override x mesh", true);
set("override y mesh", true);
set("override z mesh", true);
set("dx", 25e-9);
set("dy", 45e-9);
set("dz", 27.5e-9);
set("x", 0);
set("x span", W+2*E);
set("y min", -2e-6);
set("y max", (Ny+1)*Lambda+2e-6);
set("z", 0);
set("z span", T);
# reduce mesh density near edges
# add source
addmode; set("name", "ModeSource");

```

```
set("injection axis", "y-axis");
set("mode selection", "fundamental TE mode");
set("wavelength start", ftd_d_wavelength_min);
set("wavelength stop", ftd_d_wavelength_max);
set("x",  $-W/2-E/2$ );
set("x span",  $E+200e-9$ );
set("y",  $-extension+SimMarginY+0.5e-6$ );
set('z', 0);
set("z span",  $0.5e-6$ );
setglobalmonitor("frequency points",FREQ_PTS);
addpower; set("name", "Monitor_Left");
set('monitor type', 'Linear Y');
set('x',  $-W/2-(E-R)/2$ );
set("y min",0);
set('y max',  $(Ny+1)*Lambda$ );
set('z', 0);
set('override global monitor settings', 0);
addpower; set("name", "Monitor_Right");
set('monitor type', 'Linear Y');
set('x',  $W/2+(E-R)/2$ );
set("y min",0);
set('y max',  $(Ny+1)*Lambda$ );
set('z',D);
set('override global monitor settings', 0);
select("FDTD"); setview("extent"); # zoom to extent
```


Appendix D

Buckling Analysis

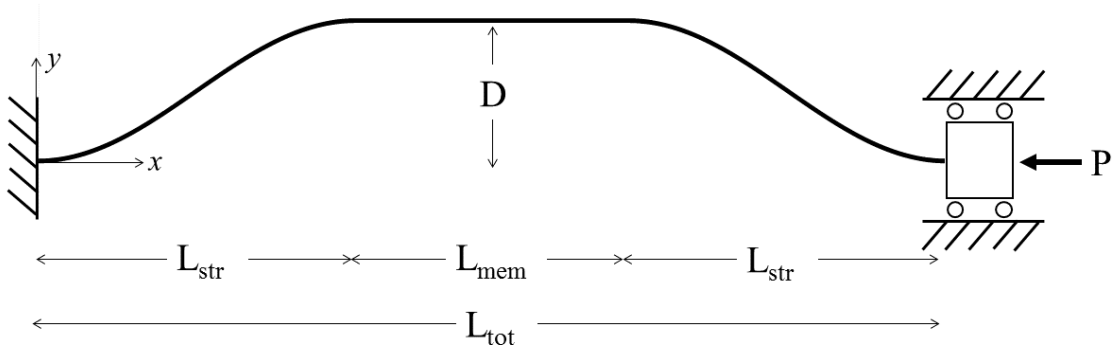


Figure D.1: Fixed-fixed buckling of a beam under axial loading

Here, the critical buckling force P_c and an estimation of buckling mode amplitude D is given. For the piecewise fixed/rigid/fixed beam configuration as shown in Fig. D.1 we assume the PC membrane can be approximated by a perfectly rigid beam of length L_{mem} that bridges the buckled struts together which are of length L_{str} . The assumption is valid as long as the PC membrane width is much larger than the strut member width. Consider an applied force $P = \sigma_0 A$ due to intrinsic SOI stress σ_0 acting on strut members of cross sectional area $A = tw$. At a given point x along the beam, the restoring moment M of the beam may be described as a function of local curvature y'' .

$$\frac{M}{EI} = \pm y'' \quad (D.1)$$

An applied moment due to applied force generated at each point along the beam as a function of beam deflection y

$$M = -Py \quad (D.2)$$

Requiring the applied and the restoring moments to be balanced yields the following Sturm-Liouville form

$$y'' + \kappa^2 y = 0 \quad (D.3)$$

$$\text{where } \kappa = \sqrt{\frac{P_c}{EI}} \quad (D.4)$$

The boundary conditions of the fixed/fixed arrangement are given by

$$\begin{aligned} y(0) &= 0 & y(L_{tot}) &= 0 \\ y'(0) &= 0 & y'(L_{tot}) &= 0 \end{aligned} \quad (D.5)$$

The piecewise conditions of the rigid connecting member require y' to remain constant along the L_{mem} portion of the beam

$$y'(L_{str} \leq x \leq L_{str} + L_{mem}) = C \quad (D.6)$$

The first buckling mode which satisfies D.3 and the boundary conditions is given by

$$y(x) = \begin{cases} \frac{D}{2} [1 - \cos(\kappa x)] & \text{if } 0 \leq x < L_{str} \\ D & \text{if } L_{str} \leq x < L_{str} + L_{mem} \\ \frac{D}{2} [1 - \cos(\kappa(x - L_{str} - L_{mem}))] & \text{if } L_{str} + L_{mem} \leq x < 2L_{tot} \end{cases} \quad (D.7)$$

with the critical buckling load is given by

$$\kappa = \frac{\pi}{L_{str}} \quad (D.8)$$

$$P_c = \frac{\pi^2 EI}{L_{str}^2} \quad (D.9)$$

As with all eigenvalue problems, the mode shape is well defined while the amplitude remains unknown. This is due to the arbitrary moment generated at the boundaries. However, we can estimate the amplitude by considering the path length along the beam. If we assume the beam no longer compresses beyond P_c and subsequent deformation occurs along the y direction, the change in path length is determined by the difference between the applied load and critical buckling load.

$$\frac{1}{A} (P - P_c) = \frac{E \Delta L_{tot}}{L_{tot}} \quad (\text{D.10})$$

$$\frac{L_{tot}}{EA} (P - P_c) = \Delta L_{tot} \quad (\text{D.11})$$

The change in path length is given by

$$\Delta L_{tot} = \int_0^{L_{tot}} \sqrt{1 + y'^2} dx - L_{tot} \quad (\text{D.12})$$

If y' is small, the Taylor expansion yields

$$\Delta L_{tot} \approx \int_0^{L_{tot}} 1 + \frac{1}{2} y'^2 dx - L_{tot} \quad (\text{D.13})$$

$$\Delta L_{tot} \approx \int_0^{L_{tot}} \frac{1}{2} y'^2 dx \quad (\text{D.14})$$

Piecewise evaluation of the integral yields

$$\Delta L_{tot} \approx \frac{D^2 k^2 L_{str}}{8} \quad (\text{D.15})$$

In terms of the strain

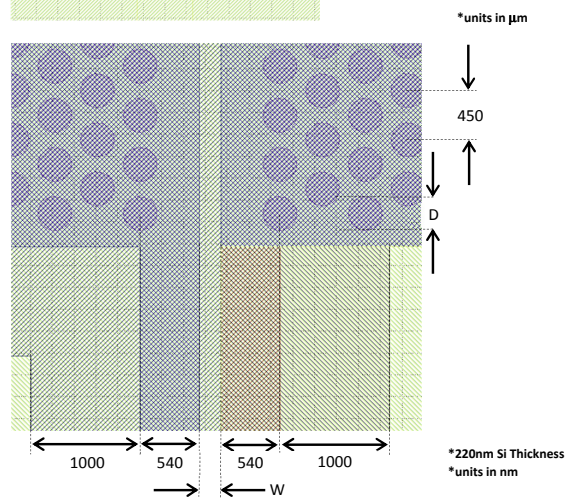
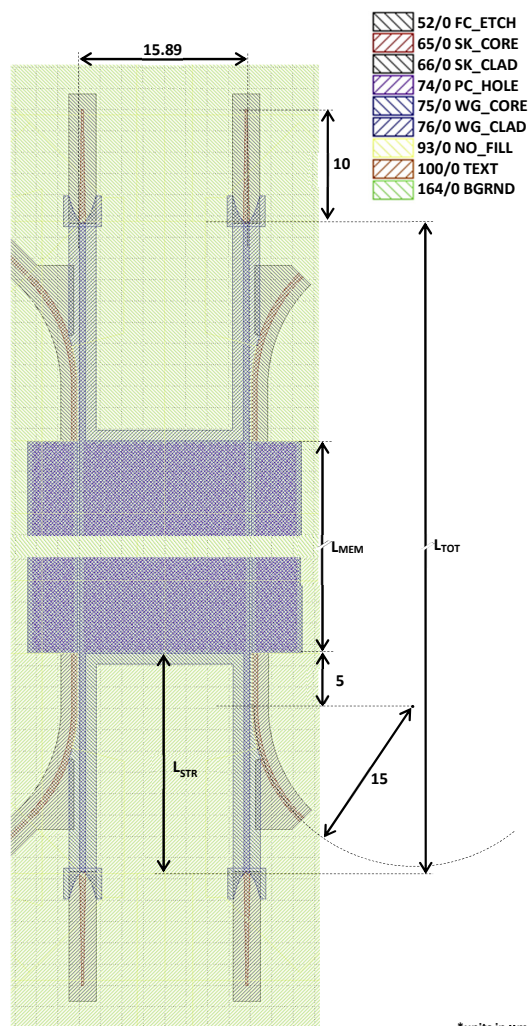
$$D \approx \sqrt{8 \frac{\sigma_o L_{tot} L_{str}}{\pi^2 E} - \frac{2 L_{tot}}{3 L_{str}} t^2} \quad (\text{D.16})$$

Appendix E

Project Specifications

Device Specifications

Code	CH/RB	W	D*	L _{TOT}	N _{MEM} [†]	L _{MEM} [‡]	L _{STR} [§]	K**
UNIT	TYPE	nm	nm	μm	# of holes	μm	μm	N/m
101	CH	200	320	150	53/54	24.47	62.765	
102	CH	200	280	150	53/54	24.43	62.785	
103	CH	200	320	150	57/58	26.27	61.865	
104	CH	200	280	150	57/58	26.23	61.885	
105	CH	200	320	150	61/62	28.07	60.965	
106	CH	200	280	150	61/62	28.03	60.985	
107	CH	200	320	150	65/66	29.87	60.065	
108	CH	200	280	150	65/66	29.83	60.085	
109	CH	200	300	150	53/54	24.45	62.775	
110	CH	200	260	150	53/54	24.41	62.795	
111	CH	200	300	150	57/58	26.25	61.875	
112	CH	200	260	150	57/58	26.21	61.895	
113	CH	200	300	150	61/62	28.05	60.975	
114	CH	200	260	150	61/62	28.01	60.995	
115	CH	200	300	150	65/66	29.85	60.075	
201	RB	200	320	70	53/54	24.47	22.765	
202	RB	200	280	70	53/54	24.43	22.785	
203	RB	200	320	70	57/58	26.27	21.865	
204	RB	200	280	70	57/58	26.23	21.885	
205	RB	200	320	70	61/62	28.07	20.965	
206	RB	200	280	70	61/62	28.03	20.985	
207	RB	200	320	70	65/66	29.87	20.065	
208	RB	200	280	70	65/66	29.83	20.085	
209	RB	200	300	70	53/54	24.45	22.775	
210	RB	200	260	70	53/54	24.41	22.795	
211	RB	200	300	70	57/58	26.25	21.875	
212	RB	200	260	70	57/58	26.21	21.895	
213	RB	200	300	70	61/62	28.05	20.975	
214	RB	200	260	70	61/62	28.01	20.995	
215	RB	200	300	70	65/66	29.85	20.075	
301	RB	300	320	85	85/86	38.87	23.065	
302	RB	300	280	85	85/86	38.87	23.065	
303	RB	300	320	85	91/92	41.57	21.715	
304	RB	300	280	85	91/92	41.53	21.735	
305	RB	300	320	85	97/98	44.27	20.365	
306	RB	300	280	85	97/98	44.23	20.385	
307	RB	300	320	85	103/104	46.97	19.015	
308	RB	300	280	85	103/104	46.93	19.035	
309	RB	300	300	85	85/86	38.85	23.075	
310	RB	300	260	85	85/86	38.81	23.095	
311	RB	300	300	85	91/92	41.55	21.725	
312	RB	300	260	85	91/92	41.51	21.745	
313	RB	300	300	85	97/98	44.25	20.375	
314	RB	300	260	85	97/98	44.21	20.395	
315	RB	300	300	85	103/104	46.95	19.025	
401	RB	200	320	55	27/28	12.77	21.115	
402	RB	200	280	55	27/28	12.73	21.135	
403	RB	200	320	55	31/32	14.57	20.215	
404	RB	200	280	55	31/32	14.53	20.235	
405	RB	200	300	55	27/28	12.75	21.125	
406	RB	200	260	55	27/28	12.71	21.145	
407	RB	200	300	55	31/32	14.55	20.225	
408	RB	200	260	55	31/32	14.51	20.245	
409	RB	200	310	55	29/30	13.66	20.670	
0	RB	N/A	N/A	N/A	N/A	N/A	N/A	



* D_{Target} = 270 nm (imec process known to create smaller PC holes)

† N_{MEM(i0)}/N_{MEM(i1)} are number of holes along the coupler length

‡ L_{MEM} = N_{MEM(i0)} × 0.45 + 2 × (0.15 + D/2000)

§ L_{STR} = (L_{TOT} - L_{MEM})/2

** Spring constant under uniform pressure

*units in μm

*220nm Si Thickness
*units in nm

Curriculum Vitae

Name: Michael Zylstra

Post-Secondary Education and Degrees: McMaster University
Hamilton, ON
2003 - 2008 B.Sc.

University of Western Ontario
London, ON
2010 - 2014 B.Eng.

Honours and Awards: Dean's Honor List
2011 - 2013

NSERC USRA
2013

QEII-GSST
2013 - 2014

OGS
2013 - 2015

Related Work Experience: Teaching Assistant
The University of Western Ontario
2008 - 2012

Publications:

J. Sabarinathan, M. Zylstra, A. Bakhtazad, Photonic crystal coupled waveguides pressure sensors, International Symposium on Optomechatronic Technologies (ISOT), Seattle, 2014.

J. Sabarinathan, A. Bakhtazad, B.Poulsen, M. Zylstra, Photonic crystal thin-film micro-pressure sensors, International Conference on Optical & Optoelectronic properties of Materials & Applications (ICOOPMA), Leeds, UK, 2014; Journal of Physics: Conference Series (JPCS) 2015.